UNIVERSITAT DE BARCELONA

On the Dynamics Around the Collinear Points in the Sun-Jupiter System

Gladston Duarte Ferreira

Aquesta tesi doctoral està subjecta a la llicència ***Reconeixement- NoComercial – CompartirIgual 4.0. Espanya de Creative Commons***.

Esta tesis doctoral está sujeta a la licencia ***Reconocimiento - NoComercial – CompartirIgual 4.0. España de Creative* Commons**.

This doctoral thesis is licensed under the ***Creative Commons Attribution-NonCommercial-ShareAlike 4.0. Spain License***.

On the Dynamics Around the Collinear Points in the Sun-Jupiter System

Gladston Duarte Ferreira

PhD Advisor: **Àngel Jorba Monte**

Universitat de Barcelona
Programa de Doctorat en Matemàtiques i Informàtica

Tesi presentada per en Gladston Duarte Ferreira per optar al grau de

Doctor en Matemàtiques i Informàtica

Director: Àngel Jorba Monte

Departament de Matemàtiques i Informàtica

Facultat de Matemàtiques i Informàtica

Novembre de 2019

Certifico que la següent tesi
ha estat realitzada per en
Gladston Duarte Ferreira
sota la meva direcció.

Barcelona, novembre de 2019.

Àngel Jorba Monte

Agradecimentos / Agradecimientos / Agraïments / Acknowledgements

A Deus, sobre todas as coisas.

À minha família e parentes por todo o apoio e alegrias divididas. Em especial à minha mãe Oneida e ao meu pai José Luiz por todo o amor e suporte durante esses anos.

Agraeixo al meu director l'Àngel, per l'acolliment, pels infinits consells, per les correccions siguin del castellà i/o català, siguin de les matemàtiques, i per creure sempre em mi, tot i quan jo mateix no m'ho creia.

Al Carles per sempre estar motivant tothom el seu voltant a fer matemàtiques, pel seu bon humor de cada dia i per seus intents de ensenyar-me francès.

A Arturo por los cafés, por ser siempre solícito aúnque le cueste minutos o aún horas a más en la universidad y por las clases.

A Àlex por su amistad, su buen humor, su acogida inicial y sus clases y ayudas.

Agradezco a Anna por su infinita paciencia con mis preguntas tontas siempre después de las clases de gràfics y por interceder por mi, mismo cuando yo no lo veia necesario.

Als (a les) altres professors(res) que també han sigut importants per a mi en aquesta temporada a Barcelona: en Joan Carles, en Miquel, en Jaume, en Gerard, la Susana, la Núria, l'Ernest, l'Antoni, la Mireia, l'Eloi, la Tere, en Tomás, la Mercè, l'Amadeu, en Marcel i l'Esther.

Certamente não poderia deixar de agradecer às pessoas que contribuíram de maneira mais direta pra minha carreira como pesquisador antes do doutorado: À Valéria, meu muito obrigado por me apresentar ao mundo da mecânica celeste ainda na graduação. Desde aquele momento que você me citou essa área, despretensiosamente, eu sabia de alguma forma que aquilo era pra mim. Obrigado por todos os conselhos, por todas as broncas e por todos os bullyings, porque eu cresci com eles. À Stefanella, que desde os primeiros

encontros para orientação e trabalho no mestrado me plantou a semente de vir pra Barcelona fazer meu doutorado. Obrigado por tornar esse sonho de vida de fazer parte de minha formação acadêmica fora do Brasil possível. E à Teresa que muito mais que uma coorientadora, foi uma verdadeira amiga que me entendia e sempre procurou o melhor pra mim, sem medo de me mostrar a realidade fosse ela qual fosse. Obrigado pelos infinitos conselhos e pela paciência de me explicar o mais mínimo e insignificante detalhe das minhas dúvidas, por vezes, bobas.

Além disso, é importante também lembrar das que fizeram um trabalho anterior de formação acadêmica: agradeço à Julieta, grande responsável por me trazer pra matemática desde a disciplina de Introdução à Teoria dos Números e, ao mesmo tempo, não me fazer abandonar a computação; à Alessandreia (Tia Alê), pela incrível energia e paixão pela profissão, além de uma amabilidade e preocupação sem igual, um verdadeiro exemplo; à Lucy pelas horas e horas que passamos conversando, pela amizade e pelos conselhos sobre a vida dentro e fora do mundo acadêmico; à Cristiane por aquele minicurso de Introdução à Análise Funcional que terminou o trabalho começado pela Julieta de me fazer ver que eu talvez gostaria de me embrenhar pelo mundo matemático, acabei por escolher a área de sistemas dinâmicos, mas a semente plantada deu frutos; e ao André, responsável por uma parte considerável da minha formação de base, pela exigência e pelo esmero com a profissão.

Agradeço ao Rodrigo pelos excelentes conselhos e conversas sobre a vida acadêmica, agraïments aquests que estenc a la Núria per sempre tenir algún plan o alguna idea al cap per treure'ns de la rutina e também ao Otávio pelo seu alto astral corriqueiro e pelas idas a compras. Muito obrigado pelo acolhimento inicial, por me possibilitar falar um pouquinho de português aqui em Barcelona quando já estava cansado de pensar pra poder falar e pelos ótimos momentos compartilhados.

Agradezco a mi compañera de despacho y portera del xalet Begoña, por su amistad, por los cafés, por su paciencia con mis dudas de castellano y por tener un horario con pocas intersecciones conmigo, lo que nos posibilitó trabajar en nuestras tesis.

A Joan por la recepción, por las llamadas por Skype/Gtalk/Duo/cualquier otro, por siempre tener las informaciones burocráticas y formularios a mano y por el soporte cuando más me fué necesario.

A Marc por las conversaciones sobre mecánica celeste, fútbol, Brasil, Catalunya, España, y más, por las ayudas por mis dudas y por todas las referencias y códigos compartidos.

Agraeixo a en Narcis per a la seva amistat, la seva paciència d'escoltar-me i per contar-me les xafarderies del món acadèmic.

A Alberto por las alegrias y desesperos compartidos y por permitirme ser yo mismo, llevando a escenas

como, por ejemplo, una clase improvisada de samba por las calles de Sevilla.

À Maisa também pelo acolhimento, não somente inicial, como também final, confiando em mim cegamente, pelo carinho e pelas conversas e conselhos.

A la Giulia pel seu bon humor de cada dia i pels partits de futbol.

A l'Òscar pels cafés dels seminaris, per les motivacions i per les informacions dels congressos i beques.

I would also like to thank Linda for her incredible enthusiasm, for telling me about the summer school in her university and for receiving there in Beijing guiding/driving me around.

Hi ha molta més gent que volia agrair: els altres membres del seminari d'estudiants en sistemes dinàmics: Mar, Salvador, Clara, Ivan, Stefano, Mariana, a la gente que la UB me ha presentado: Carlos, l'Ari, en Dani, en Jordi, la Marina, Marco, o la BGSMath: Claudia, Marina, Álvaro, Anastasia or even the UPC: Roisin. Aproveitando o ensejo, à galera brasileria da UAB: Murilo, Natália, Leo, Tainã, Fernando, Júlia, Gabi, Gustavo, Bruna, Jackson e Ricard (és clar que t'hauria de posar aquí, oi?).

Obviously I could not forget about the Mediterranean Squad: Athena, Dario, Jonathan, Marina, Omar, Pedro and Roberto. Thank you all for the best time ever in Beijing. And also, I would also like to thank Lumei for the reception and for helping with some translations, extending to Yue and Jim for walking me around.

Agredeço, obviamente, à galera do forró, em especial a Marina, a Ewa, ao Pedro e à Daniela. Vocês podem ter certeza que fizeram meus dias muito mais leves por aqui. Obrigado por tudo, inclusive por serem insistentes comigo me arrastando pro forró muitas vezes e desculpa quando eu sumia ou quando chegava atrasado.

I also thank people in Atlanta: Bhanu, for the wonderful reception; Larissa, obrigado por me escutar num dos momentos que eu mais precisei e não teria condições de falar em inglês; Livia, for all the support; my officemate Heather, for all the interesting conversations. I extend it to Jiaqi, Adrian, Yian, and Jaemin. It was a privilege to know you all.

Agraeixo al personal administratiu, comunicació i gestió: la Raquel, en Luca, la Núria, la Vanessa i l'Arantxa del CRM, a la Inno, en Victor, la Dolors i la Montse de la UB i a la Patrícia de l'IMUB pel vostre treball amb els papers.

Agradezco al personal de la seguridad de la UB, en especial a Tona, Maribel y Adri, por permitirme trabajar en horas/dias/semanas no muy convencionales y por vuestra amabilidad y conversaciones super intersantes que por muchas veces me sacaban del estado tenso de trabajo y me permitian relajar mejor.

A les meves professores del CPNL: Rosa i Montserrat, per la seva increïble energia i passió per l'ensenyança

de la llengua i la cultura catalanes. Vau ser importantíssimes per a mi, no només com a professores de català però també com a exemples de professional a seguir. Aprofitant, agraeixo també a toda la gent amb qui vaig compartir aquests moments dels cursos, la Valentina, l'Elena, la Maylen, l'Osiris, en Daniel i l'Elena, la Diana, la Manuela, la Noe, la Maika, la Gimena, la Natalia, i altres.

Agradeço imensamente aos meus amigos e às minhas amigas que são parte tão essencial de mim. A quem pôde vir me visitar: Renata (ainda estou te devendo uma visita!), Werneck, Aline, Jaime, Gabriel, Adriele, Iker e Natalie, Tamirys e Diogo, ainda que eu não estivesse aqui em Barcelona (uma pena): Marianna, Lucas, Vinícius e Thaís. A quem eu consegui visitar: Henrique, Claudson, Davi e Tamy, Elias e Carina, Walter, (tia) Lilian e Úrsula. A quem me deu motivos para voltar ao Brasil: Luiz Maurílio e Rosa, Fernanda e Erick, ou que está dando agora: Krissy e Alexandre. A quem a tecnologia da informação permitiu ver e conversar: Mariana (maninha!), Perácio, Gaby, Nathália e Alexia. A quem já tem um tempo que não vejo: Gi e Roberto, Gi e Sacul, Fernanda, Kaká, Aline, Lucas, Angel, Hanailly, Diego, Juliana, Renan, Vinícius, Sara, Alexander, Daniel, Jenny, Freddy, Anselmo, Anninha, Camila, Ceili, Cayus, Naty, Teresa, e poderia ficar aqui por mais páginas e páginas, mas considero que mais importante que ter o nome aqui neste parágrafo, foram os momentos que compartilhamos juntos, motivo mais que suficiente para que quem leia até aqui possa colocar seu próprio nome nestas linhas.

A la BGSMath per aquesta oportunitat de desenvolupar la meva tesi doctoral a la UB.

To the membres of the committee for reading this thesis.

Muito obrigado!

¡Muchas gracias!

Moltes gràcies!

Thank you very much!

Gladston Duarte Ferreira

Barcelona, 25 de novembre de 2019

Esta tesis ha sido posible gracias al proyecto MDM-2014-0445 a través del Programa María de Maeztu para Unidades de Excelencia en investigación y desarollo del Ministerio de Economía y Competitividad de España. This work has been supported by the Spanish grants PGC2018-100699-B-I00 (MCIU/AEI/FEDER, UE) and the Catalan grant 2017 SGR 1374. The project leading to this application has received funding from the European Union's Horizon 2020 research and innovation programme under the Marie Skłodowska-Curie grant agreement No 734557.

Resum en Català

Aquesta tesi té com a objectiu l'estudi quantitatiu del Mecanisme de Transició Ràpida (Rapid transition Mechanism) que explica algunes propietats de l'òrbita d'alguns objectes espacials, com per exemple, el cometa 39P/Oterma, que serà l'objecte principal de l'estudi d'aquesta recerca.

Si considerem que el Sol i Júpiter són les masses que més influencien l'objecte considerat, el mecanisme descriu una transició que farà que l'objecte passi d'una configuració en la qual es troba en una òrbita exterior a la de Júpiter a una d'interior o viceversa.

Aquest mecanisme s'observa, en particular, a l'espai de fase dels models que fem servir en aquesta tesi: el problema restringit de tres cossos, sigui pla i circular o bé pla i el·líptic. En aquest models en consideren tres cossos, dos dels quals, anomenats primaris, tenen massa positiva i les seves òrbites evolucionen segons les solucions del problema de dos cossos, és a dir, són cercles, el·lipses, paràboles o hipèrboles tenint com a focus (o centre) el centre de masses dels dos. El tercer cos (el moviment del qual volem descriure) es considera que té massa zero i, per tant, no influencia el moviment dels primaris però està sota la seva influència gravitacional. Estudiarem els casos en els quals l'òrbita dels primàris sigui un cercle o una el·lipse i que l'òrbita del tercer cos estigui continguda al mateix pla del moviment dels primaris.

Hem pres la decisió de considerar aquests dos models després d'haver fet una extensa exploració numèrica amb diferents models de n-cossos per simular el Sistema Solar, considerant diferents planetes com a més influents en la dinàmica d'Oterma. També s'han considerades les dades en diferents temps inicials de simulació i s'han analitzat els canvis si es modifiquen lleugerament les dades d'Oterma ajustant-les en els models estudiats. Aquestes dades han estat agafades del sistema Horizons del JPL (Jet Propulsion Laboratory), que està disponible al web: https://ssd.jpl.nasa.gov/horizons.cgi.

Cal dir que un punt força important d'aquests models és que hi ha, als dos casos, un sistema de coordenades que possibilita l'existència de punts d'equilibri i això facilita la descripció de la dinàmica. En el cas circular, aquest sistema té l'eix x definit de manera que els primaris hi pertanyin; l'eix z que sigui

paral·lel al moment angular dels primaris; i, finalment, l'eix y de manera que aquest sistema sigui ortogonal i positivament orientat; a més a més, aquests eixos giren amb la velocitat angular dels primaris per a que no es moguin relativament al sistema. En el cas el·líptic hi ha alguns sistemes que es podem fer servir, el que hem fet en aquesta tesi és un en el qual els eixos es defineixen de la mateixa manera, però en lloc de coordenades que giren amb velocitat angular constant, els eixos giren amb velocitat no constant de manera que els primaris sempre pertanyin a l'eix x i la distància entre els primaris sigui sempre igual a 1, donant lloc a un efecte pulsatori d'expansió i contracció. Aquests dos sistemes de coordenades s'anomenen coordenades sinòdiques.

Triats els models per estudiar aquest tipus de transició es procedeix a l'estudi de l'esquelet del sistema, és a dir, s'estudien quins objectes invariants són els més importants i responsables per descriure la dinàmica d'Oterma. Aquesta metodologia és general en l'estudi de l'espai de fase de sistemes dinàmics: tals objectes són els punts d'equilibri, òrbites periòdiques, tors, varietats, atractors, repulsors i altres, segons el context de cada problema. Específicament pels models Hamiltonians que hem triat per explicar el fenomen de transició a l'espai de fase, els objectes més relevants són els següents:

- Al model circular hi ha dos punts d'equilibri (L_1 i L_2) tals que, al voltant de cadascú, hi ha una família d'òrbites periòdiques hiperbòliques, que tenen varietats estable i inestable de dimensió 2.

- Al model el·líptic, els punts d'equilibri són els mateixos i, a més a més, es troben al mateix lloc que els del model circular, però, en canvi, com que aquest model pot ser considerat com una perturbació 2π-periòdica del model circular, la família d'òrbites periòdiques es converteix en una família de tors, també hiperbòlics, i que també posseeixen varietats estables i inestables que ara són de dimensió 3.

En ambdós casos, les connexions heteroclíniques entre les òrbites periòdiques o els tors a través de les seves varietats estables i inestables dóna lloc al mecanisme responsable de la transició ràpida. Més concretament aquesta transició ràpida té lloc quan la connexió es fa abans que alguna de les varietats invariants de les òrbites periòdiques (o tors) completi una volta entorn del primari situat entre aquest parell de punts d'equilibri - en el cas d'Oterma, Júpiter.

Per calcular aquests punts d'equilibri en el model circular (que ens serviran també pel model el·líptic) és suficient resoldre (numèricament) una equació polinomial de grau 5 anomenada quíntica d'Euler. Després, discutim com calcular les òrbites periòdiques al voltant dels punts de manera semi-analítica, fent servir una eina coneguda com a formes normals, que també ens permet calcular una bona aproximació inicial per a les varietats invariants estables i inestables d'aquestes òrbites. S'inclou també el càlcul purament numèric de les periòdiques i les seves varietats amb la finalitat de generalitzar aquest procediment al cálcul de tors i les seves

varietats. En aquest últim cas, s'han representat els tors com una aproximació en sèrie de Fourier. De fet, es considera el difeomorfisme donat per la integració a temps d'un període de Júpiter (en el model el·líptic, es pot fer servir altres variables com a variable independent) i es calculen les corbes de la corresponent aplicació. Degut al fet que la inestabilitat dels tors és molt forta, considerem una representació en més d'una secció en la variable independent (i no només en una, com és comú) i la integració d'un període es divideix a trossos - aquest abordatge s'anomena tir paral·lel.

Finalment, localitzem Oterma en aquest context. Es detallen els canvis de variable de coordenades siderals a coordenades sinòdiques. Això permet llegir les coordenades d'Oterma de Horizons i representar-les en coordenades sinòdiques. Aproximant les coordenades inicials (projectant-les en el pla dels primaris) i integrant el model pla i el·líptic s'obté un indici que aquest és un bon model per reproduir, almenys parcialment, la dinàmica d'Oterma. Podem així, aleshores, visualitzar Oterma dins de l'espai de fase i com interactua amb els objectes invariants considerats. En particular, fent servir seccions en l'anomalia verdadera f i en la coordenada x alhora, és possible calcular tors invariants al voltant d'L_1 i d'L_2 tals que les seves varietats invariants són més properes a l'òrbita d'Oterma. A més a més, fent servir seccions adequades en f i en x, s'han aconseguit visualitzacions de les connexions heteroclíniques entre aquests tors propers l'òrbita d'Oterma.

Contents

Chapter 1

Introduction

In this work we study the behavior of a comet, called Oterma, whose dynamics is heavily influenced by Jupiter and it leads to an intriguing and interesting orbit.

What happens is that at some point of its trajectory it is between Jupiter and Saturn, as comparing their distances from the Sun, but, after a while, its orbit is between Mars and Jupiter, it stays there for some years, and gets back to its original position. In other words, first Oterma's orbit could be approximated by an elliptical one with semi-major axis greater then Jupiter's one at some moments and smaller at some others.

Oterma is not the only comet that have this type of behaviour, in fact, some comets to have this , or a similar, type of behaviour are: 36P/Whipple, 82P/Gehrels, 129P/Shoemaker-Levy 3 and 147P/Kushida-Muramatsu. ([OIY+08])

Some of them experience what is known as a Rapid Transition Mechanism - not revolving around Jupiter while transitioning -, some complete at least one full revolution around Jupiter, and some have collided.

Figure 1.1 shows some plots of the trajectory of Oterma (in red) and Jupiter (in green) in a sidereal frame (x, y, z) coordinates (being the xOy reference plane the ecliptic and mean equinox of reference epoch (JD=2452200.5) and the reference frame ICRF/J2000.0 in JPL Horizons Web-Interface) and its projection in the xOy plane:

Remark: All the orbits shown from now on have a small variation in the z-axis so, unless where it is stated the opposite, they will be presented as if they were planar, even when they are not.

As claimed by [KLM+01] one can think at first sight of using the Planar Circular Restricted Three-Body Problem (PCRTBP) as a model, or, at least, as a starting point, to study this situation.

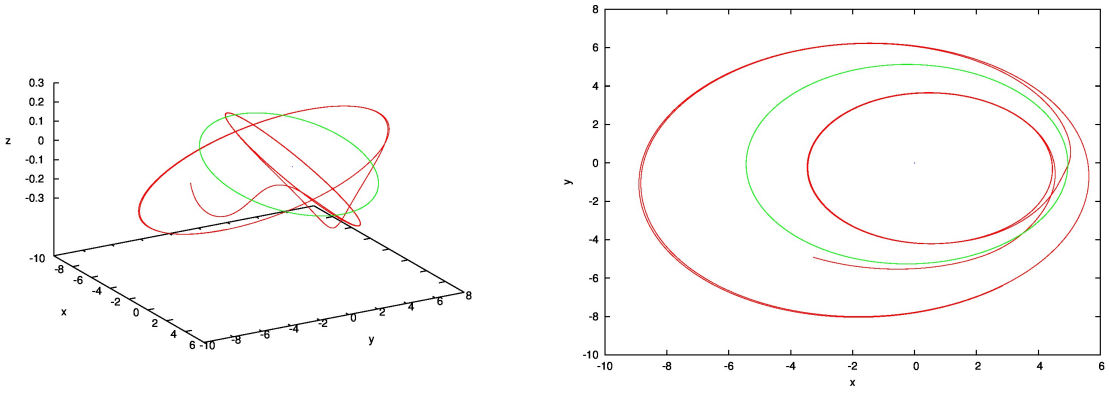

(a) (b)

Figure 1.1: Transition in Oterma's trajectory in the (a) (x, y, z) coordinates and (b) (x, y) projection.

One possible scenario, in the PCRTBP for this transition to occur is drawn in what follows:

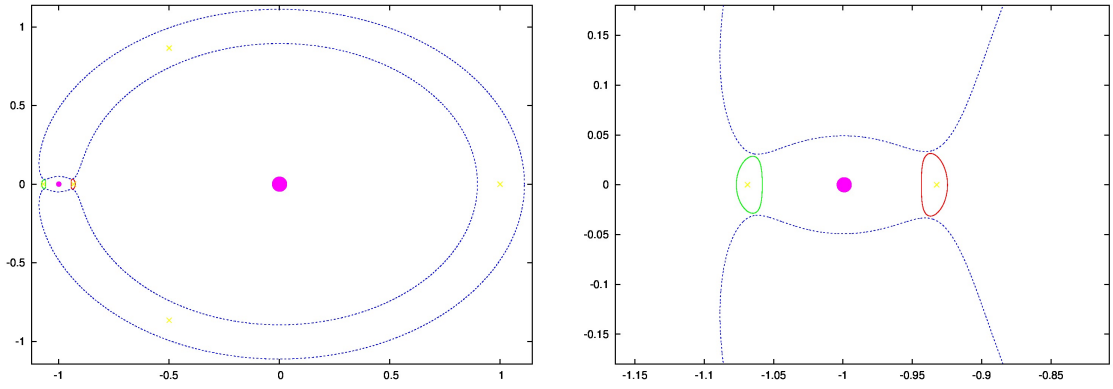

(a) (b)

Figure 1.2: ZVC, equilibrium points and periodic orbits around L_1 and L_2 in the PCRTBP.

Remark: It is not our claim that the scenario presented in Figure 1.2 is the only one where this behaviour happens, instead, the reason for considering this scenario is, among others, not having other objects (for instance, L_3) that could play a key role is this dynamics, in other words, the Zero-Velocity curve must permit this type of transition, from the inside region to the outside one, i.e., it is enough to have a connected region of possible motion.

Figure 1.3 shows some examples of transitions in this scenario.

The goal of this thesis is to study this problem via a dynamical systems point of view, i.e., following [KLM+01], computing the dynamical objects responsible for this behaviour, checking which are the most important ones when studying Oterma's dynamics and comparing what can be improved when considering

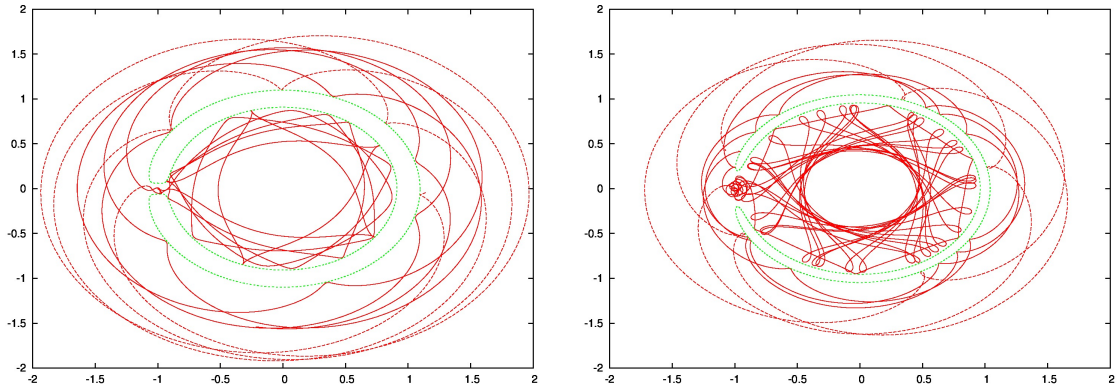

(a) (b)

Figure 1.3: Some examples of transitions in the PCRTBP. Particle's initial data do not represent any known comet or asteroid. The solid lines represent a forward integration, the red dashed ones a backward, the green dashed lines are the ZVC.

different models, more specifically, what is improved when describing its dynamics when considering that Sun and Jupiter describe and elliptic orbit instead of a circular one.

1.1 Models

The N-Body problem can be described as follows: Given the initial positions and velocities of N point masses in a given space (most commonly $\mathbb{R}^2$ or $\mathbb{R}^3$) under mutual gravitational attraction, predict their orbits.

Let r_i be the position of the i^{th} body.

The system of equations to be solved is

$$\ddot{r}_i = \sum_{\substack{j=1 \\ j\neq i}}^{N} \frac{Gm_j}{|r_j - r_i|^3}(r_j - r_i).$$

In the case of the Restricted $N+1$-Body Problem, in addition to the above system, one should also consider that the $N+1^{th}$ body is influenced by the other N bodies, so that the system turns out to be

$$\begin{cases} \ddot{r}_i = \displaystyle\sum_{\substack{j=1 \\ j\neq i}}^{N} \frac{Gm_j}{|r_j - r_i|^3}(r_j - r_i) \\ \ddot{r}_{N+1} = \displaystyle\sum_{j=1}^{N} \frac{Gm_j}{|r_j - r_{N+1}|^3}(r_j - r_{N+1}). \end{cases} \tag{1.1}$$

There are some interesting system of coordinates to study this problem - namely the sidereal and the

synodical ones.

Remark: The synodical coordinates were initially designed to be applied to the RTBP, i.e. for $N = 2$, however there are some problems involving more bodies that use this system of coordiantes as well - for instance, [Wie84, GLM+87, Jor00] in the Bicircular Problem and [And98, AS99], in the Quasi-Bicircular Problem, to name a few.

The sidereal system of coordintes is an inertial one, on which its axis should be defined using some planes of reference, for instance, when dealing with some Solar System computations, the most commons ones are the Ecliptic (uses as the reference plane the one defined by Earth's orbit) and the Equatorial (uses the Equator plane as a reference) ones, although there are some more, for instance the Galactic, the Supergalactic and the Horizontal ones. ([Mee98, Val97])

The synodical system of coordinates, in the case of a circular problem, is defined as a system that revolves with the same constant angular velocity as the primaries; the x-axis by the line between the primaries, oriented from the less massive to the more massive one; the z-axis points at the angular momentum vector; and the y-axis is defined accordingly in order to have a positive oriented basis; it is usual, to simplify, to make units of distance, time and mass such that the gravitational constant is 1, their period is 2π and the sum of their masses also equals 1, as a consequence, the distance between the primaries is also 1.

Is these coordinates, the primaries do not move, they stand still in two points to be defined:

- the less massive one in $(-1+\mu, 0, 0)$ and the more massive one in $(\mu, 0, 0)$; ([Sze67])
- the less massive one in $(-\mu, 0, 0)$ and the more massive one in $(1-\mu, 0, 0)$. ([KLM+01])

Notice that, in both cases, their mutual distance is still 1, it is a matter of which convention one is adopting.

For this work, we will be adopting the first one.

In the case of an elliptical movement, the angular velocity of these rotating coordinates are not constant anymore, instead, they revolve with the same angular velocity as the primaries.

In addition, the unit of length is variable. It depends on the distance between the primaries, in such a way that they are located in the same points as before.

This produces an effect of pulsation - as the unit of length varies - in such a way, these set of coordinates are also said to be roto-pulsating ones.

With the above-mentioned synodical systems of coordiantes, we describe below the different versions of the Restricted Three-Body Problem (RTBP), namely:

- The Planar and Circular RTBP (PCRTBP);
- The Spatial and Circular RTBP (SCRTBP);
- The Planar and Elliptic RTBP (PERTBP);
- The Spatial and Elliptic RTBP (SERTBP);

Under the hypothesis of a circular movement, i.e. that Jupiter and Sun describe a circular orbit, this problem can be described by the following Hamiltonian:

$$H(x,y,z,p_x,p_y,p_z) = \frac{1}{2}(p_x^2+p_y^2+p_z^2) + yp_x - xp_y - \frac{1-\mu}{r_1} - \frac{\mu}{r_2}, \tag{1.2}$$

where $r_1 = (x-\mu)^2 + y^2 + z^2$ and $r_2 = (x+1-\mu)^2 + y^2 + z^2$.

If in addition, it is also assumed that the movement is planar, i.e., that Oterma moves in the same plane as Sun and Jupiter, it is enough to take $z = 0$ and $p_z = 0$, in such a way that the Hamiltonian turns out to be

$$H(x,y,p_x,p_y) = \frac{1}{2}(p_x^2+p_y^2) + yp_x - xp_y - \frac{1-\mu}{r_1} - \frac{\mu}{r_2}, \tag{1.3}$$

where $r_1 = (x-\mu)^2 + y^2$ and $r_2 = (x+1-\mu)^2 + y^2$.

The case where the primaries describe an elliptic orbit mimics, in some sense, the above feature of being enough to "ignore" the (z, p_z) pair when considering the movement as a planar one.

The Hamiltonian, in this case, is non-autonomous and can be written in the following way:

$$\begin{aligned} H(x,y,z,p_x,p_y,p_z,f) \quad = \quad & \frac{1}{2}\left((p_x+y)^2 + (p_y-x)^2 + p_z^2 + z^2\right) \\ & -\frac{1}{1+e\cos f}\left(\frac{1}{2}(x^2+y^2+z^2) + \frac{1-\mu}{r_1} + \frac{\mu}{r_2}\right), \end{aligned} \tag{1.4}$$

where $r_1^2 = (x-\mu)^2 + y^2 + z^2$, $r_2^2 = (x+1-\mu)^2 + y^2 + z^2$ and e is Jupiter's eccentricity and f is its true anomaly. ([Sze67])

Notice that, instead of the time as the independent variable, the above Hamiltonian has the true anomaly f as it, and the reason for presenting and modelling the problem is this way is facility of handling it.

In fact, for the PERTBP, following [Flo04], one may model using the time as the independent variable with the following Hamiltonian:

$$H(x,y,p_x,p_y,t) = \frac{1}{r^2}\left(\frac{p_x^2}{2} + \frac{p_y^2}{2} + yp_x - xp_y\right) - \frac{e\sin f}{r}(xp_x + yp_y) - \frac{1-\mu}{\tilde{r_1}} - \frac{\mu}{\tilde{r_2}},$$

where $r^2 = \dfrac{1}{(1+e\cos f)^2}$, $\tilde{r_1}^2 = r^2((x-\mu)^2+y^2)$, $\tilde{r_2}^2 = r^2((x+1-\mu)^2+y^2)$ and f is given by

$$\tan\frac{f}{2} = \left(\frac{1+e}{1-e}\right)^{1/2}\tan\frac{E}{2}$$

and the eccentric anomaly E is computed via the recurrence formula $E = n(t-T) + e\sin E$, being n the mean motion and T the time of perigee passage.

There are other formulations using different independent variables, for instance, still following [Flo04], the eccentric anomaly E:

$$H(x,y,p_x,p_y,E) = \frac{\sqrt{1-e^2}}{1-e\cos E}\left(\frac{p_x^2}{2}+\frac{p_y^2}{2}+yp_x-xp_y\right) - \frac{e\sin E}{1-e\cos E}(xp_x+yp_y) - \frac{1-\mu}{r_1} - \frac{\mu}{r_2},$$

where $r_1^2 = (x-\mu)^2+y^2$ and $r_2^2 = (x+1-\mu)^2+y^2$.

In the case of the sidereal coordinates when handling the problem in $\mathbb{R}^3$, one can consider them as (x,y,z) coordinates, so that the system (1.1) turns out to be

$$\begin{cases} \ddot{x}_i &= \displaystyle\sum_{\substack{j=1\\ j\neq i}}^{N} \frac{Gm_j}{|r_j-r_i|^3}(x_j-x_i) \\ \ddot{y}_i &= \displaystyle\sum_{\substack{j=1\\ j\neq i}}^{N} \frac{Gm_j}{|r_j-r_i|^3}(y_j-y_i) \\ \ddot{z}_i &= \displaystyle\sum_{\substack{j=1\\ j\neq i}}^{N} \frac{Gm_j}{|r_j-r_i|^3}(z_j-z_i) \\ \ddot{x}_{N+1} &= \displaystyle\sum_{j=1}^{N} \frac{Gm_j}{|r_j-r_{N+1}|^3}(x_j-x_{N+1}) \\ \ddot{y}_{N+1} &= \displaystyle\sum_{j=1}^{N} \frac{Gm_j}{|r_j-r_{N+1}|^3}(y_j-y_{N+1}) \\ \ddot{z}_{N+1} &= \displaystyle\sum_{j=1}^{N} \frac{Gm_j}{|r_j-r_{N+1}|^3}(z_j-z_{N+1}). \end{cases} \tag{1.5}$$

In order to numerically solve system (1.5), one should transform it in a set of first-order differential equations and apply a solver. All the computations done in sidereal coordinates in this thesis were done based in a Taylor integrator. ([JZ05])

1.1.1 Planar and Circular Restricted Three-Body Problem

This section is based on results contained in [Sze67].

Recalling the expression for the Hamiltonian in the PCRTBP (1.3), the ODE system describing this dynamics is given by

$$\begin{cases} \dot{x} &= p_x + y \\ \dot{y} &= p_y - x \\ \dot{p}_x &= p_y - (1-\mu)\dfrac{x-\mu}{((x-\mu)^2+y^2)^{3/2}} - \mu\dfrac{x+1-\mu}{((x+1-\mu)^2+y^2)^{3/2}} \\ \dot{p}_y &= -p_x - (1-\mu)\dfrac{y}{((x-\mu)^2+y^2)^{3/2}} - \mu\dfrac{y}{((x+1-\mu)^2+y^2)^{3/2}}. \end{cases} \tag{1.6}$$

This is a 2 degrees-of-freedom autonomous Hamiltonian system, which means that its phase space is four-dimensional, foliated by three-dimensional submanifolds each one associated with a value of a first integral - in this case, the Hamiltonian itself - so that, if one is interested in studying this system, a good strategy is to set a specific value for the Hamiltonian (sometimes called as the energy), investigate its features inside this submanifold, and then change this set value, investigate again this feature, change once again, and so on.

Of course this is not enough to detect, describe and analyse all the dynamics, but it is a good strategy to start to understand it, and also, when doing this, it is also possible to have the reduction of the dimension of the problem, making it easier to visualize.

This last case is the one chosen to be applied in this thesis, in fact, in Section 4.4 we will present some Poincaré sections that illustrate intersections of some two-dimensional tube manifolds that can be easily seen with this strategy.

In addition, as we will see in the next sections, this reduction of the dimension will also be an important tool in the case of the elliptic problem.

The PCRTBP has 5 equilibium points, called L_i, $i = 1, \cdots, 5$, three of them located at the x-axis, L_2 to the left of the mass located at $(-1+\mu, 0, 0)$, L_1 between the primaries and L_3 to the right of the one located at $(\mu, 0, 0)$; and two located at the third vertex of an equilateral triangle where the other two points are the primaries, one with positive y value, and the other one with negative y.

As the last result of this section, we mention that some key objects to explain Oterma's dynamics are the periodic orbits around the equilibrium points L_1 and L_2 and their stable/unstable manifolds. These points

are linearly unstable being of centre × saddle type, and due to this nature, for each value of the Hamiltonian, there is a periodic orbit around each of these points with stable and unstable manifolds. Based in [KLM+01], intersections between these manifolds of the periodic orbits are the responsible for the transition between regimes.

1.1.2 Planar and Elliptic Restricted Three-Body Problem

The equations for the PERTBP, based on its Hamiltonian (Equation (1.4), setting $(z, p_z) = (0, 0)$) are given by

$$\begin{cases} x' &= p_x + y \\ y' &= p_y - x \\ p_x' &= p_y - x + \dfrac{1}{1+e\cos f}\left(x - (1-\mu)\dfrac{x-\mu}{((x-\mu)^2+y^2)^{3/2}} - \mu\dfrac{x+1-\mu}{((x+1-\mu)^2+y^2)^{3/2}}\right) \\ p_y' &= -p_x - y + \dfrac{1}{1+e\cos f}\left(y - (1-\mu)\dfrac{y}{((x-\mu)^2+y^2)^{3/2}} - \mu\dfrac{y}{((x+1-\mu)^2+y^2)^{3/2}}\right), \end{cases} \tag{1.7}$$

where $'$ denotes the derivative with respect to f.

This model is a four-dimensional non-autonomous Hamiltonian system, which means that now the Hamiltonian is not a first integral anymore, i.e., it cannot be used to reduce this system's dimension.

In other words, this system's phase space is one dimensional larger than the last one, but in addition, the Hamiltonian value cannot be used to reduce the system's dimension, which means that now we are dealing with a full five-dimensional system.

Notice that, when setting $e = 0$ (the circular case) in (1.4), one recovers the Hamiltonian (1.2), i.e., these models are consistent.

For small values of e, the elliptic model can be seen as a 2π-periodic time dependent perturbation of the circular one.

The equilibria points, in the above-explained roto-pulsating coordinates, are the same as in the circular model. ([Sze67])

As periodic orbits around L_1 and L_2 in the circular model are now perturbed by a 2π-periodic function, the ones that are not resonant are converted to invariant tori, with the same stability (centre × saddle).

It should be mentioned that, although the circular and the elliptic problems have a strict relation between them, their differences require different tools to study them, as we shall see in the following chapters. More

specifically, in Chapter 4 and Appendix A tools to study the PCRTBP will be presented, and the ones to study the PERTBP will be presented in Chapter 5.

1.2 What has been done so far?

Concerning Oterma's dynamics and its modeling, the pioneering work of [KLM+01] has to be mentioned, as the ideas behind this paper are an important basis for this thesis.

On it, the authors, using the PCRTBP, explain which are the dynamical objects that act in the transition of Oterma and also compute them for some case. As the real data is not presented, qualitatively it is extremely relevant, but maybe, quantitatively, the PCRTBP is not the best model to describe Oterma's orbit.

About tori and its stable and unstable manifolds numerical computation, [Jor01] contains the necessary tools to compute them. Some tools are mixed with the ones presented in this paper in order to accuretely have the desired precision in the case of computing the invariant tori around L_1 and L_2. These tools will be presented in Chapter 5 and Appendix A.

In [AEL16] the authors discuss some computations of orbits and manifolds in the SCRTBP using a dynamical systems tool known as Isolating Blocks. It is beyond the scope of this thesis to discuss this tool and this application, it is refered here as a possible future direction for this work. It is also important to notice that all the computations done there were for the case that the primaries were Earth and Moon, so Oterma's case was not discussed there.

In [GL18] the authors are also dealing with the SCRTBP, more specifically with the computations of the invariant manifolds and some chaos indicators using a specific set of coordinates. They use the mass parameter of Sun and Jupiter system, but it is not among their goals the intersection between invariant manifolds to explain and ilustrate Oterma's dynamics.

1.3 Motivation and Objectives

When simulating the Solar System, considering the Sun, the inner planets, the outer planets, Pluto and Oterma as a gravitational $(n+1)$-body problem, in sidereal coordinates, it is possible to see Oterma's transition from an orbit which is exterior to the Jupiter's one to a interior one and back again.

Different planets influence Oterma's orbit by different magnitudes, and the one that does it the most is Jupiter. Simulating the dynamics of just the Sun, Jupiter and Oterma, diminishing the considered time span, the same behaviour is observed for Oterma. So, in order to study the transition, it is possible to

consider as a base model, the RTBP.

When considering the Sun and Jupiter in a circular movement, it is not possible to see the transition when fitting Oterma's data in the PCRTBP, but if we consider them in an elliptic orbit, Oterma does the transition. Therefore, it would be interesting to consider the planar and elliptic RTBP for a better quantitative description of this phenomenon that Oterma experiences.

The dynamical objects that play a key role in explaining Oterma's dynamics, both in the circular and in the elliptical case are similar and, although the tools to compute them are also similar, their differences make it important to distinguish the cases when considering the circular model and when considering the elliptic one.

In this thesis we also present a number of numerical experiments that justify the choosing of the planar and elliptic model to better describe Oterma's dynamics, together with the tools needed to compute the model's invariant dynamical objects involved on this dynamics - namely invariant tori with their stable and unstable manifolds - and some plots locating Oterma in its transition, with respect to these computed objects. These numerical experiments also show that the PERTBP is not the best model to describe Oterma's transition, in fact, the projection made in Sun-Jupiter's plane of movement alter qualitatively Oterma's return, so, in addition to support to the decision of using the PERTBP as a first step in improving the quantitative description of Oterma's behaviour, the simulations also give hints of possible future research directions.

1.4 Structure of the Thesis

This thesis is divided as follows: in Chapter 1 we present some preliminary results and discuss some features of the main application of the tools exhibited in this thesis; in Chapter 2 we present the changes of variables used in this study and its purposes; the goal of Chapter 3 is to present a number of numerical experiments made to check which planets influence most Oterma's orbit, so that we are able to discuss the validity of considering the presented models (the PCRTBP and the PERTBP, to be explained still in Chapter 1) and to give a hint of possible future directions; in Chapter 4 we present a semi-analytical tool used to compute some dynamical objects in the Planar and Circular Restricted Three-Body Problem and some Poincaré sections to visualize some features; in Chapter 5, as already mentioned, we present tools to investigate and compute quasi-periodic and related invariant objects; Chapter 6 is the most important one, that is when we present how all these tools and presented computations can be applied in the study of the dynamics of comet 39P/Oterma, improving its understanding via a dynamical system way; finally, in Chapter 7 we present some general conclusions of this study and some immediate future directions. Appendix A is written for the sake

of self-completeness and also for pedagogical reasons, all the tools presented and discussed in this appendix are already known in the literature and there is nothing new there, but its ideas are of great help when explaining Chapter 5, since the environment is simpler when computing periodic orbits (and related objects) than when computing quasi-periodic ones; in Appendix B we present a diagram of the code developed and the produced files to have all the numerical results presented here in this thesis; in Appendix C these files are briefly explained, what they contain and for what they were used for.

Chapter 2

Changes of Variables

It is important to care about the set of variables one will use to represent the system being studied, not only for facility in handling the equations but also because one should care about how to better visualize the interesting features of it. In fact, it is not unusual to see the same system being represented in different sets of variables depending on the phenomena that is being observed.

It is not always obvious how to change between two given sets of variables representing the same system, and it can take a long or a short time to implement these changes. However, it is something that should be analysed case by case - because it will depend not only on the system, but also on the sets of coordinates of such system, as there may be a number of them to represent it.

In this chapter we will be presenting only the changes departing from the sidereal coordinates as they are the ones that we gather from JPL Horizons. There exist also the inverse changes, but they will not be presented here as they were not used in any moment throughout this work.

In addition to the difficulties that may be presented in computing the changes of variables representing a system, we should also state that, as in this thesis we are dealing with a number of systems, a special care should be taken in the moment on which these changes will be applied. In other words, depending on the time we will consider a model or other, we may have some changes in the behaviour of the system. As examples:

- In this chapter, when comparing the changes of variable departing from the same system (Sun-Jupiter-Oterma considering, not only them, but also the other main bodies in the Solar System) and reaching the PCRTBP (Section 2.2) there is no Oterma's transition, while, when reaching the PERTBP (Section 2.3), Oterma does it.

- In Chapter 3, where some N-Body models are considered and the change presented in Section 2.1 is apllied to them leading to some different qualitative behaviours in Oterma's orbit.

2.1 From Sidereal to Orbital Elements

The orbital elements are a set of 6 coordinates (it should be mentioned that this set is not unique) that in a certain way better describe a Keplerian orbit. This "certain" way is in the sense of given, in a moment t, a set of coordinates (x, y, z, v_x, v_y, v_z) of positions and velocities in an inertial Euclidean frame, it is hard (not to say impossible) to gather any information from this orbit, meanwhile if one is given a set of orbital elements, those informations are available there, informations such as, if the orbit is elliptical, the shape of this ellipse, the angle it has with some given plane, the nearest and the furthest point of the orbit from the centre of mass, among others.

Remark: In the case where one does not have Keplerian orbits, the change presented in this section can be used to compute the orbital elements of the osculating orbit of the given bodies.

Let us describe now the classical set of orbital elements.

The first and the second orbital elements are presented to us in any basic course of analytic geometry: the **semimajor axis** a and the **eccentricity** e, that model the shape of the orbit.

Remark: It should be mentioned that, for many applications, instead of the semimajor axis a, the semiparameter p is used. It measures the minimum distance between the focus where the centre of mass is located and the orbit. The reason for this is because in parabolic orbits, the semimajor axis is infinite. For this work however, the seminajor axis will be used.

The other four elements are angles that determine the postion of the orbit related to a given reference frame.

Depending on each system, this frame can be defined in many ways, for instance, if we are modelling a spacecraft travelling around the Earth, then we can use the equatorial plane as the xOy plane and the z axis oriented in the North Pole direction.

For the rest of this subsection, we will use the notation (x, y, z) as the adopted reference frame, and we will consider that the orbit is an ellipse.

The elements are described as follows:

The **inclination** i is measured as the angle between the z axis and the angular momentum vector c. It can be seen as a measure of how much the ellipse is not contained in the xOy plane.

The **longitude of the ascending node** Ω is the angle measured between the x axis and the line of

nodes, which is a line from the origin to the ascending node, a point in the orbit and in the xOy plane at the same time, where the particle goes towards the northern direction, i.e., the particle goes from the negative part of the z axis to the positive one.

The **argument of perigee** ω is the angle between the ascending node and the perigee.

The **true anomaly** f is the angle between the perigee and the position of the particle.

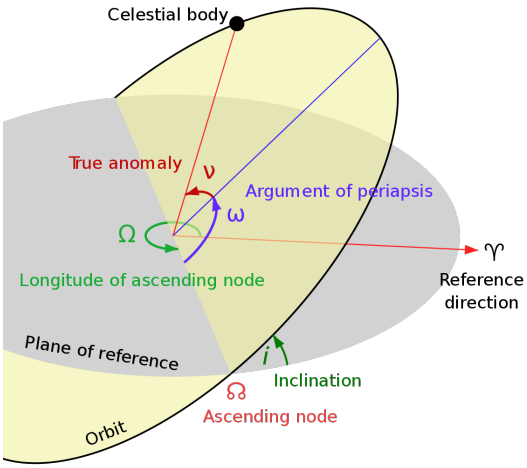

Figure 2.1: Illustration of some orbital elements.
File:Orbit1.svg (https://commons.wikimedia.org/wiki/File:Orbit1.svg)
by Lasunncty (https://en.wikipedia.org/wiki/User:Lasunncty)
is licensed under CC BY-SA 3.0 (https://creativecommons.org/licenses/by-sa/3.0/).

The formulas to compute the orbital elements described above are presented in the following paragraphs. ([Val97]).

Let $\overrightarrow{i}$, $\overrightarrow{j}$ and $\overrightarrow{k}$ be unitary vectors in the x, y and z directions, respectively.

Let $r = (x, y, z)$ and $v = (v_x, v_y, v_z)$ be the particle's position and the velocity vectors, respectively.

Let $\eta = \overrightarrow{k} \times c$ (it is a vector in the line of nodes), $E = \frac{1}{\mu}\left(|v|^2 - \frac{\mu}{|r|}\right) r - (r \cdot v)v$ (be a vector pointing at the perigee) and $\mathcal{E} = \frac{|v|^2}{2} - \frac{\mu}{|r|}$ (representing the energy).

We have that $c = r \times v$ and $\eta = k \times c$.

So, the following formulas allow us to compute the orbital elements (the subscrits $_x$, $_y$ and $_z$ refer to the

the components fo the vector):

$$
\begin{aligned}
e &= |E| \\
a &= -\frac{\mu}{2\mathcal{E}} \\
p &= a(1-e^2) \\
\cos(i) &= \frac{c_z}{|c|} \\
\cos(\Omega) &= \frac{n_x}{|\eta|} \\
\cos(\omega) &= \frac{n \cdot E}{|\eta| e} \\
\cos(f) &= \frac{e \cdot r}{|r| e}
\end{aligned}
$$

For the last three quantities, a special care should be taken:

- If $\eta_y < 0$ then $\Omega \longleftarrow 2\pi - \Omega$;
- If $E_z < 0$ then $\omega \longleftarrow 2\pi - \omega$;
- If $r \cdot v < 0$ then $f \longleftarrow 2\pi - f$.

2.2 From Sidereal to Synodical: the Circular Case

If we take the position and velocity data for Sun, Jupiter and Oterma on a given time t and use it as initial data for system (1.5), Sun and Jupiter would evolve in elliptical orbits inside some plane, while Oterma would have some orbit outside this plane that it is not possible to classify without a specific analysis.

In the Circular RTBP, we assume that Sun and Jupiter move in circular orbits. So we should seek a way of fitting their orbits in a circle.

In this section we will present an algorithm used to fit Oterma's position and momenta in the PCRTBP.

It should be mentioned that this process depends on time, i.e., if we consider two different times on which we apply the algorithm to fit the data t_1 and t_2, the circles generated from the algorithm would possibly be different.

The algorithm is given by:

- Project orthogonally both Oterma's position and velocity onto the plane where Sun and Jupiter move;

  - Apply the formulas: $r \leftarrow r - \frac{r \cdot N}{|N|^2} N$ and $v \leftarrow v - \frac{v \cdot N}{|N|^2} N$, where N is the normal vector to the Sun-Jupiter's movement plane;

- Rotate such plane so that it is now the xOy plane;

  - Apply a change of coordinates from cartesian to cylindric (being the axis oriented in the z-direction) and rotate around the axis so that Jupiter and Oterma are in the xOz plane, i.e., so that, the normal vector points at the direction where its θ equals $-\frac{\pi}{2}$ and apply the inverse transformation;

  - Apply a change of coordinates from cartesian to cylindric (being the axis oriented in the x-direction) and rotate around the axis so that the plane of movement is the xOy , i.e., so that, the normal vector points at the direction where its θ equals $\frac{\pi}{2}$ and apply the inverse transformation;

- Inside that plane, rotate x and y axes in such a way that both Jupiter and Sun are in the x axis;

  - Apply a change of coordinates from cartesian to polar and rotate so that, in the latter coordinates, Jupiter's θ equals π, and apply the inverse change to recover the cartesian coordinates;

- Change the units of measure of position and velocity so that Jupiter is fixed in $(-1+\mu, 0, 0)$, Sun in $(\mu, 0, 0)$ and Jupiter's period of revolution is 2π;

  - Divide the mutual distances Sun-Jupiter (r_{SJ}) and Sun-Oterma (r_{SO}) by r_{SJ}, so that r_{SJ} is 1;

  - Divide the velocity of Oterma by $n * r_{SJ}$, where n is the mean motion of Jupiter, so that the time needed for a complete revolution of Jupiter is 2π;

  - Apply the formulas $\dot{x} = p_x + y$, $\dot{y} = p_y - x$ to compute Oterma's momenta.

Based on previous works ([KLM+01, GKM+04]) one can see that this orbit does not have the qualitative behaviour one could expect: an entering in the region where Oterma would be closer to the Sun than Jupiter.

A trial-an-error adjustment in Oterma's initial velocities were done to see if it would be still possible to reproduce a similar behaviour than the one in the nature.

Figure 2.3 shows Oterma's orbit with this adjustment of adding $+0.07$ in both components (v_x, v_y) of Oterma's velocity.

Remark: The value of H used for the computation of the Zero-Velocity Curve were computed via the formula $H = -2 * J_C = x^2 + y^2 + 2\left(\frac{1-\mu}{\sqrt{(x-\mu)^2+y^2}} + \frac{\mu}{\sqrt{(x-\mu+1)^2+y^2}}\right)$, using as values of x and y the ones in the beginning of the computation, right after the application of the change of variables.

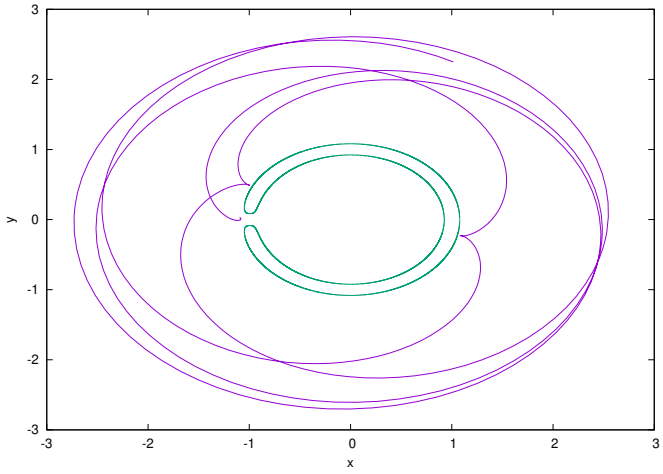

Figure 2.2: Oterma's orbit in synodical coordinates after applying the above-mentioned change of coordinates in purple, in green the ZVC for $H = 3.0184989628453996$

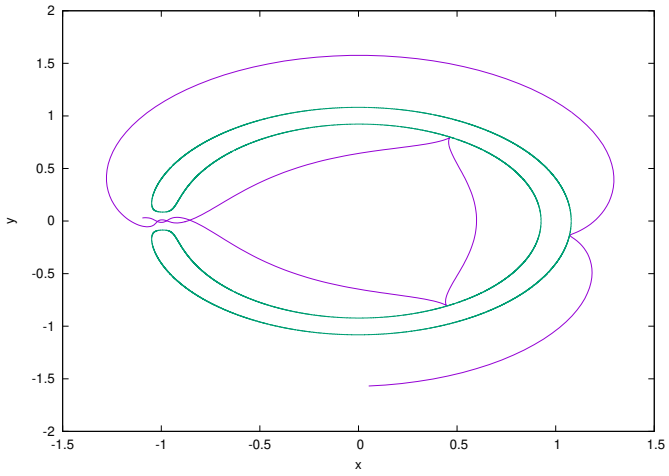

Figure 2.3: Oterma's orbit with an adjustment in its velocity

As it can be seen, in opposition to the orbit in Figure 2.2, the one in Figure 2.3 presents the phenomenon of transition we are looing for.

However, this adjustment is artificial and was made by means of observing the results and tuning to achieve the expected result.

If we are eager to build a framework where it is possible to get the data of comets/asteroids and compute if they have or not this transition without this intervention, it may be a better option to study a more accurate model, for instance, the elliptical one.

2.3 From Sidereal to Synodical: the Elliptical Case

Recalling what was explained in the beginning of the last section, considering Sun, Jupiter and Oterma interacting gravitationally under the system (1.5), being the initial conditions their positions and velocities data gathered in a given moment, Sun and Jupiter will describe an elliptic orbit.

This means that, when considering the PERTBP, no intervention in Sun's and Jupiter's orbit is necessary, just in the Oterma's one. So, as less modifications are being made, we can expect better results for this model.

Now, we should see how the change of variables is done so that the system, initially described in sidereal coordinates, could be expressed in synodical ones. ([GLM+00])

Let $\vec{e}$, $\vec{a}$ be the position vectors of the particle in sidereal and in synodical coordinates, respectively.

Let $K \in \mathbb{R}$ and $C \in \mathcal{M}_{3\times 3}(\mathbb{R})$ be such that

$$\vec{e} = KC\vec{a}.$$

Let also r_p, r_s, v_p, v_s, a_p, a_s be the position, velocity and acceleration vectors of the primaries (the more massive one with the subscript p and the other with s) in sidereal coordinates.

We have that $K = ||r_p - r_s||$ and $C = (C_0 \;\; C_1 \;\; C_2)$, being

$$C_0 = \frac{r_p - r_s}{||r_p - r_s||}, C_2 = \frac{(r_s - r_p)\times(v_s - v_p)}{||(r_s - r_p)\times(v_s - v_p)||} \text{ and } C_1 = C_2 \times C_0.$$

Let $r = r_s - r_p$, $v = v_s - v_p$, $a = a_s - a_p$.

With the above notation, we have that $\dot{K} = \dfrac{r\cdot v}{K}$ and $\dot{C} = (\dot{C}_0 \;\; \dot{C}_1 \;\; \dot{C}_2)$, with

$$\dot{C}_0 = \frac{-vK + \dot{K}r}{K^2},$$

$$\dot{C}_2 = \frac{||w||dw - \dot{w}w}{||w||^2} \text{ and}$$

$$\begin{aligned}\dot{C}_1 \quad = \quad & (C_{31}\dot{C}_{23} - C_{21}\dot{C}_{33} + C_{23}\dot{C}_{31} - C_{33}\dot{C}_{21} \\ & C_{11}\dot{C}_{33} - C_{31}\dot{C}_{13} + C_{33}\dot{C}_{11} - C_{13}\dot{C}_{31} \\ & C_{21}\dot{C}_{13} - C_{11}\dot{C}_{23} + C_{13}\dot{C}_{21} - C_{23}\dot{C}_{11}),\end{aligned}$$

where we have used the following: $w = r \times v$, $dw = r \times a$, $\dot{w} = \dfrac{w\,dw}{||w||}$.

Now we may write

$$\dot{\vec{e}} = \dot{K}C\vec{a} + K\dot{C}\vec{a} + KC\dot{\vec{a}}$$

which is equivalent to

$$\dot{\vec{a}} = \frac{C^{-1}}{K}\left(\dot{\vec{e}} - \dot{K}C\vec{a} - K\dot{C}\vec{a}\right).$$

These velocities are with respect to the time as an independent variable.

Using the chain rule, we have that $\frac{d}{dt} = \frac{df}{dt}\frac{d}{df}$ so that

$$\vec{a}\,' = \left(\frac{df}{dt}\right)^{-1}\frac{C^{-1}}{K}\left(\dot{\vec{e}} - \dot{K}C\vec{a} - K\dot{C}\vec{a}\right),$$

where $' = \frac{d}{df}$ and $\frac{df}{dt} = \frac{nl^{3/2}}{a^{3/2}(1-e^2)^{3/2}}(1+e\cos f)^2$, being n the mean motion and l the mutual distance between the primaries.

So the change of variables is given by:

$$\begin{cases} \vec{a} &= \frac{C^{-1}}{K}\vec{e} \\ \vec{a}\,' &= \left(\frac{df}{dt}\right)^{-1}\frac{C^{-1}}{K}\left(\dot{\vec{e}} - \dot{K}C\vec{a} - K\dot{C}\vec{a}\right). \end{cases}$$

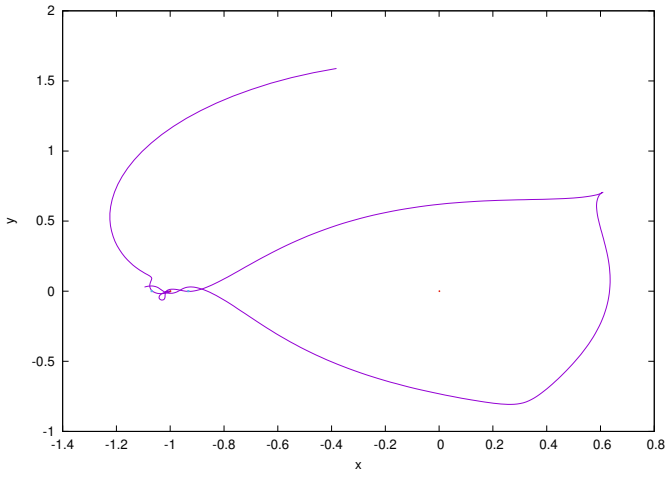

Figure 2.4: Orthogonally projected Oterma's orbit integrated using the PERTBP equations of motion (in purple); in red, Jupiter and Sun (out of scale); and in blue, L_1 and L_2 positions.

It may seem, from Figure 2.5, that there is a collision with Jupiter (when considering Jupiter's radius in the PERTBP synodic coordinates $\approx 10^{-4}$), but that, as it can be seen from Figure 2.6, is not the case.

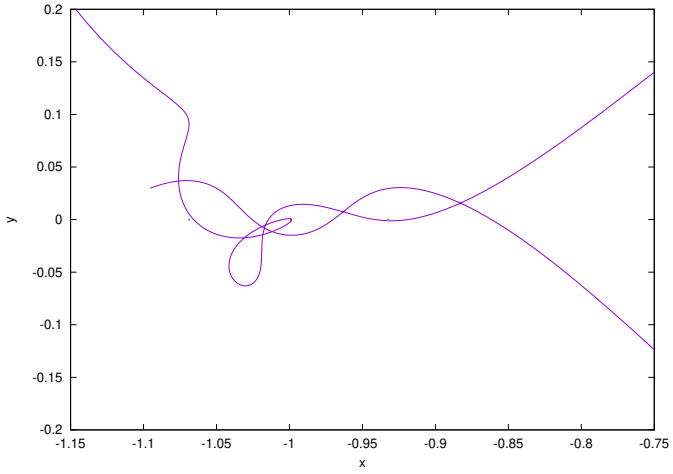

Figure 2.5: Zoom in the region near Jupiter. Same color scheme as above.

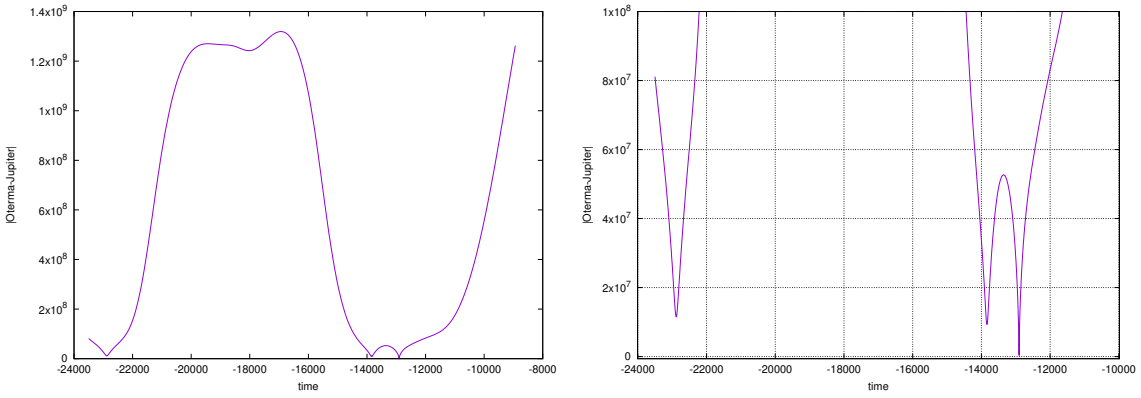

(a) (b)

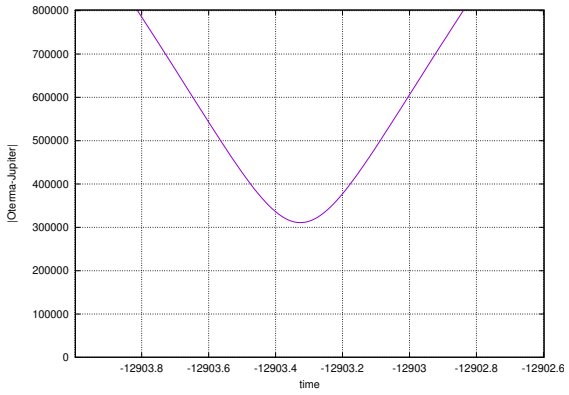

(c)

Figure 2.6: Distances between orthogonally project Oterma and Jupiter computed from August 30^{th}, 1935 to July 02^{th}, 1975. Units in days and km. (a) Full graph; (b) Zoom in three parts that could be a collision; (c) Zoom in the minimum showing that there is no collision (Jupiter's radius is 71.492 km approximately).

Chapter 3

Numerical Experiments

In this chapter we will present some simulations of the motion of Oterma including the effect of the major bodies of the Solar System. We will perform several simulations, with different numbers of planets, to see the relative importance of each body.

We will be discussing how to detect Oterma's transition from an orbit which is exterior to the Jupiter's one to a interior one and back again, which planets influence it the most, if there is any difference in getting the data and starting the simulations in different initial times and more.

In particular, this chapter is a crucial one, in which we define the model we will be using throughout the thesis to study and describe Oterma's dynamics.

It is important also to notice that this chapter gives some of the hints of possible research future directions.

3.1 Simulating the Solar System with Oterma

We start by computing Oterma's dynamics using a Taylor integrator ([JZ05]), based on an already built code. This code uses the Restricted $(N + 1)$-Body Problem, where the N main bodies could be chosen among the Sun and planets of the Solar System (although a simple adaptation can be done for any body to be considered), using the JPL Horizons system, file DE405, for the initial positions and velocities of the bodies centered at the Solar System barycentre.

In order to detect Oterma's transition, we compute the semi-major axis of the osculating orbit of every body (planets and Oterma) at each integration step, during the complete time of integration (January 1^{st}, 1900 until January 1^{st}, 2000), to see if there will be a drastic change in Oterma's behaviour.

Remark: Unless clearly stated, all the simulations for the semi-major axis were done by a backwards integration, i.e., all the data were collected in the final time (in the case of this section, January 1^{st}, 2000, which will be related to $t = 0$) and the integration were done until the initial time was reached (in this section, January 1^{st}, 1900, $t = -36525$).

Figure 3.1 show the computed semi-major axis for the time span considered.

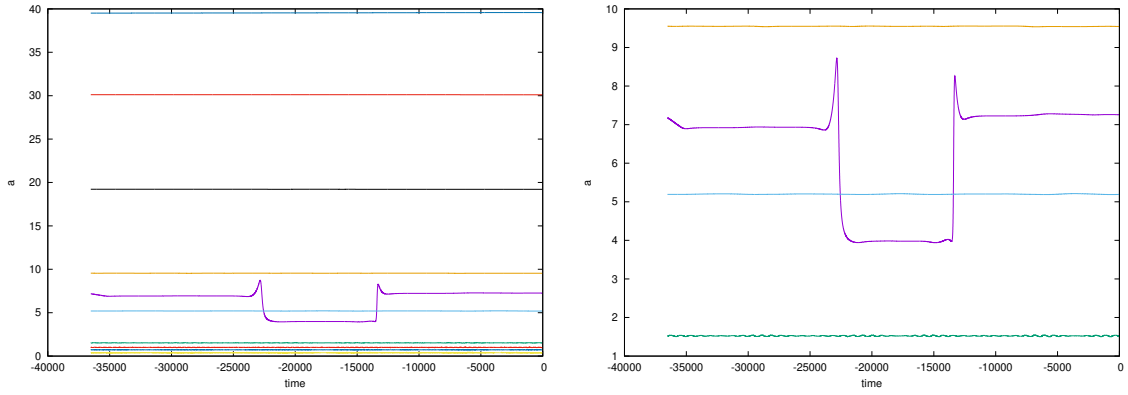

(a) (b)

Figure 3.1: Computed semi-major axis of (a) Mercury, Venus, Earth, Mars (dark green), Jupiter (light blue), Saturn (yellow), Uranus, Neptune, Pluto and Oterma (purple) (b) Mars (dark green), Jupiter (light blue), Saturn (yellow) and Oterma (purple).

As it may be seen from Figure 3.1 Oterma's semi-major axis transition from a value between Jupiter's and Saturn's to one between Jupiter's and Mars' and back again. This phenomenon can be explained as the mechanism of transitioning that was illustrated in Figures 2.3 and 2.4.

Figure 3.2 shows the computed orbits during the considered time span.

One may notice, from Figure 3.2, that Oterma's orbit is part between Jupiter's and Saturn's and part between Jupiter's and Mars'.

It should be mentioned that there is no collision when considering the complete set of main bodies of the Solar System, as can be seen from Figure 3.3.

Remark: It should be noticed the relation that there is between Figures 3.1 and 3.3: The times where there is the transition in Figure 3.1 are the times where there is an approach of Oterma and Jupiter as can be seen in Figure 3.3. This indicates that the astronomical mechanism responsible for the transition is a close encounter with Jupiter.

We shall see, in following chapters, the dynamical mechanisms for this transition to occur, i.e., we will model this system with already known models in celestial mechanics, compute some of the invariant objects

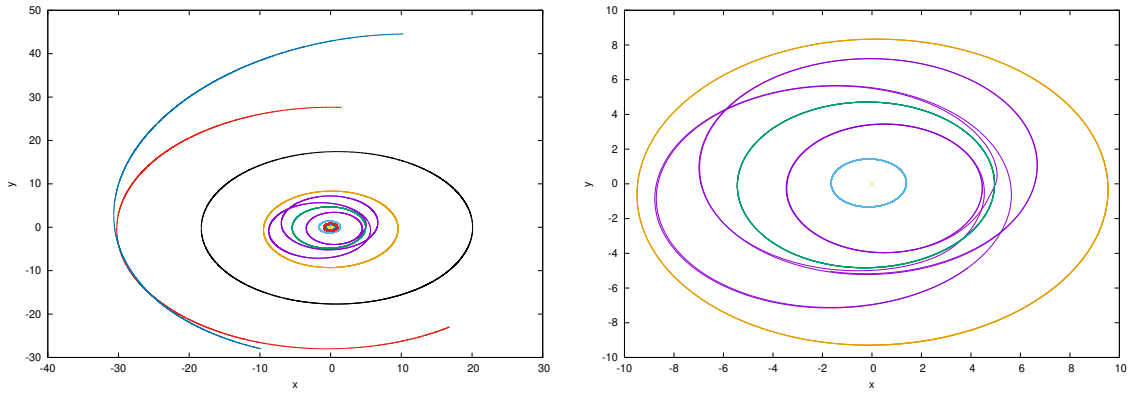

(a) (b)

Figure 3.2: Computed orbits of (a) Mercury, Venus, Earth, Mars (dark green), Jupiter (light blue), Saturn (yellow), Uranus, Neptune, Pluto and Oterma (purple) (b) Mars (dark green), Jupiter (light blue), Saturn (yellow) and Oterma (purple).

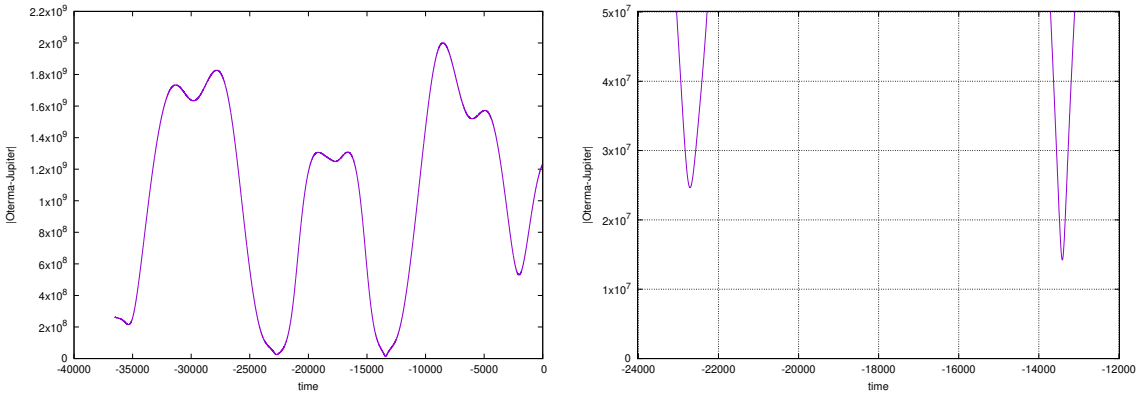

(a) (b)

Figure 3.3: Distance between Oterma and Jupiter in the considered time span. Units in km and days. (a) Complete time span; (b) Zoom in two regions where they approach.

of these dynamical systems and verify the responsable ones for this behaviour.

3.2 Models with Less Planets

In this section, we will see some experiments done to see which planets have a major influence in this observed Oterma's behaviour.

The experiments are all based in the procedure described in the last section, with the difference of the choice of model:

- choose which planets will be considered;

- take as initial conditions the position and velocities of the chosen planets in January 1^{st}, 2000;
- integrate them using the Taylor integrator described in [JZ05];
- compute, at each integration time step, the semi-major axis of the osculating orbit of each body (planets and Oterma).

It is important to state that in doing this procedure, we are choosing different Restricted $(N+1)$-Body Problems to represent Oterma's dynamics.

The following configurations were chosen:

(a) Sun and Jupiter;

(b) Sun, Jupiter and Saturn;

(c) Sun, Jupiter, Saturn, Uranus and Neptune;

(d) Sun, Mars and Jupiter;

(e) Sun, Mars, Jupiter and Saturn;

(f) Sun, Mars, Jupiter, Saturn, Uranus and Neptune;

(g) Sun, Earth and Jupiter;

(h) Sun, Earth, Jupiter and Saturn;

(i) Sun, Earth, Mars, Jupiter and Saturn;

(j) Sun, Mercury, Venus, Earth, Mars, Jupiter, Uranus, Neptune and Pluto.

Figure 3.4 summarizes the computation of the semi-major axis for all the above-described configurations of bodies.

Some considerations about Figure 3.4 can be done:

- The computation of the semi-major axis by means of the formulas presented in Section 2.1 is an approximation only valid where the movement is almost Keplerian, so that it should not be considered accurate near Oterma's transitions;
- In every scenario considered the first transition exist, but depending on the planets one consider as affecting its movement, the second may not exist;

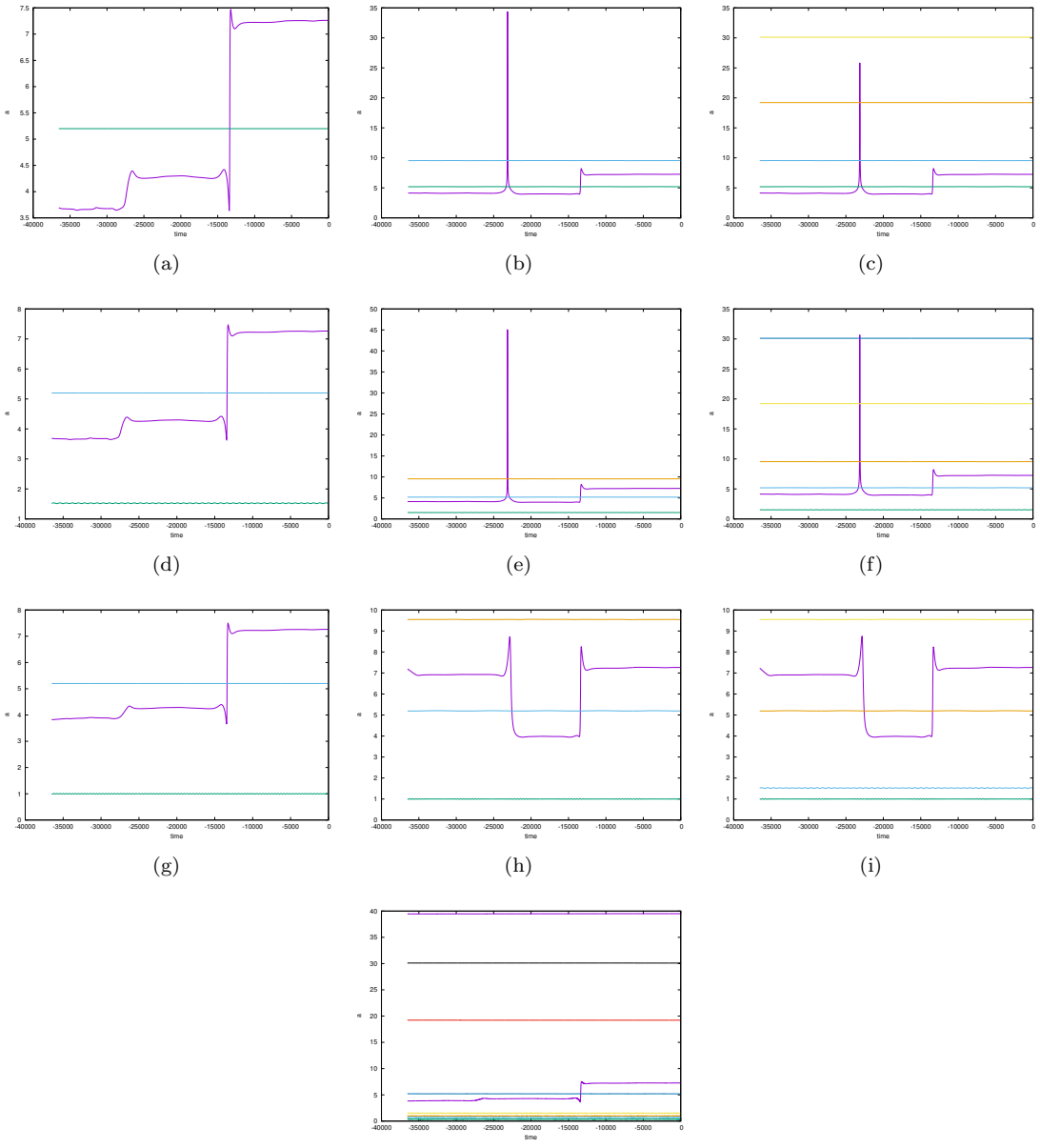

Figure 3.4: Computed semi-major axis of the considered planets and Oterma. Units in AU and days. (a) Jupiter; (b) Jupiter and Saturn; (c) Jupiter, Saturn, Uranus and Neptune; (d) Mars and Jupiter; (e) Mars, Jupiter and Saturn; (f) Mars, Jupiter, Saturn, Uranus and Neptune; (g) Earth-Moon Barycentre and Jupiter; (h) Earth-Moon Barycentre, Jupiter and Saturn; (i) Earth-Moon Barycentre, Mars, Jupiter and Saturn; (j) Mercury, Venus, Earth-Moon Barycentre, Mars, Jupiter, Uranus, Neptune and Pluto;

- Jupiter is considered in every scenario because it is the main body that affects Oterma's orbit, and its transition just occur due to gravitational interaction with it;

- If we admit a rougher approximation, we are able to see that the semi-major axis have some change

in its computation in a time near the one where the transition occurs, i.e., if we compare, for instance, Figures (a) and (h), we will see that the second transition occurs between $t = -25000$ and $t = -20000$ (in (h)), whereas in (a), it varies (not to the desired region) from $t = -30000$ and $t = -25000$ and if we compare, for instance, Figures (b) and (h), we will see that, in (b) there is an interval where this computation suffers a perturbation, and it coincides with the one in (h);

- Still about that above item, we are able to say, furthermore, that the time-shift in the change of the semi-major axis' behaviour is due to the presence of Saturn in the considered model. Having it there alter Oterma's orbit both directly - direct gravitational interaction - and indirectly - modification of Jupiter's orbit. Notice that, Figures (b), (c), (e) and (f) are computations where Saturn were involved and where some perturbation in the semi-major axis occur in the same time-interval as Figures (h) and (i) (that have the desired behaviour), while in Figures (a), (d), (g) and (j) the perturbation in this computation is occur in a different (although near) time-interval;

- It is clear that there are many other configurations to be tested, but that is not the focus of this work, here we focus on the fact that different configurations lead to different results.

Of course, when trying to model this system, one is looking for the simplest possible description where the desired phenomenon occur.

In the next section, we will see how changing the initial time of integration can lead us to interesting and intriguing results, and how we will take our initial conditions to integrate and compute the dynamical objects of the modelled system to see which are the ones that matter the most.

3.3 Starting the Simulation at Different Initial Times

In the last section, it was discussed the changes produced in Oterma's orbit when using different Restricted $(N + 1)$-Body Problems. Now, we shall see another variation in Oterma's orbit.

The algorithm described in the last section, now reads:

- choose which planets will be considered;

- choose a date in which we shall read, as initial conditions, the position and velocities of the chosen planets;

- integrate them using the Taylor integrator described in [JZ05];

- compute, at each integration time step, the semi-major axis of the osculating orbit of each body (planets and Oterma).

Remark: There is no special reason for choosing the initial times that were chosen, they are just to illustrate qualitative changes in Oterma's behaviour.

We start by considering the effect of only Sun and Jupiter, i.e., as if Sun and Jupiter were in a two-boy problem, orbiting around each other in ellipses, gravitationally influenting Oterma which is not in the same plane of movement, so that this problem can be understood as a SERTBP.

Figure 3.5 shows some computed semi-major axis.

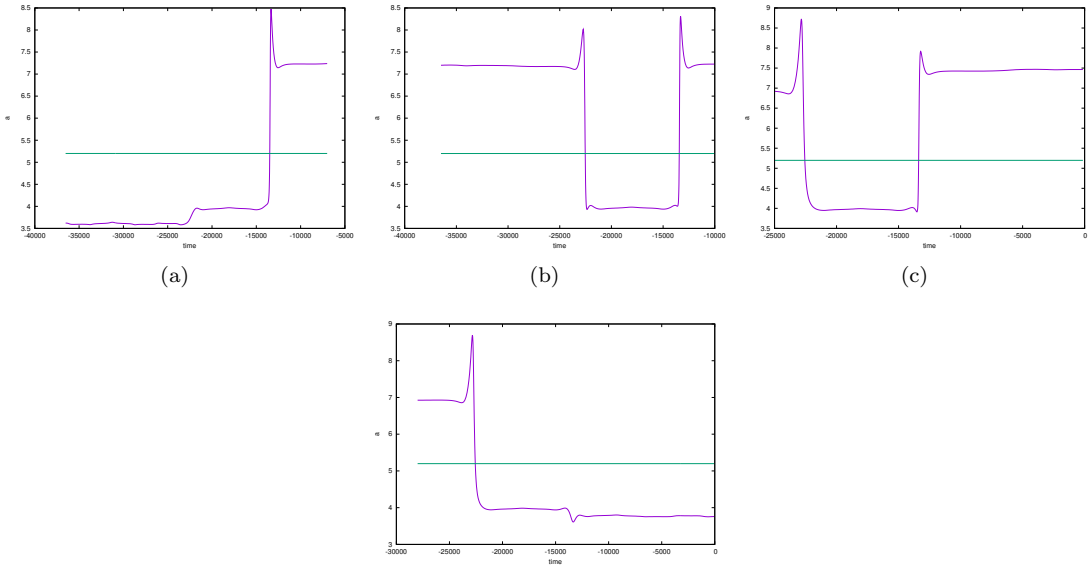

(a) (b) (c)

(d)

Figure 3.5: Computed semi-major axis of Jupiter and Oterma. Units in AU and days. (a) Backward integration starting at $t = -7000$ (November 1^{st}, 1980); (b) Backward integration starting at $t = -10000$ (August 15^{th}, 1972); (c) Forward integration starting at $t = -25000$ (Jult 22^{nd}, 1931); (d) Forward integration starting at $t = -28000$ (May 5^{th}, 1923).

Notice that, as we take as the initial data a set closer to the one at the time where the transition occurs, Jupiter's influence in Oterma's behaviour becomes more apparent, i.e., the closer to the transition, the more other planets' effects are negligible.

Adding Saturn to this dynamics, makes it possible to extend this domain where the transition occurs somewhat, as it may be seen from Figure 3.6.

Comparing two pairs of figures - namely Figures 3.5(a)(a) and 3.6(c) and Figures 3.5(d) and 3.6(d) - we may see that, at the same initial times, if we consider also the influence of Saturn, Oterma have its transition,

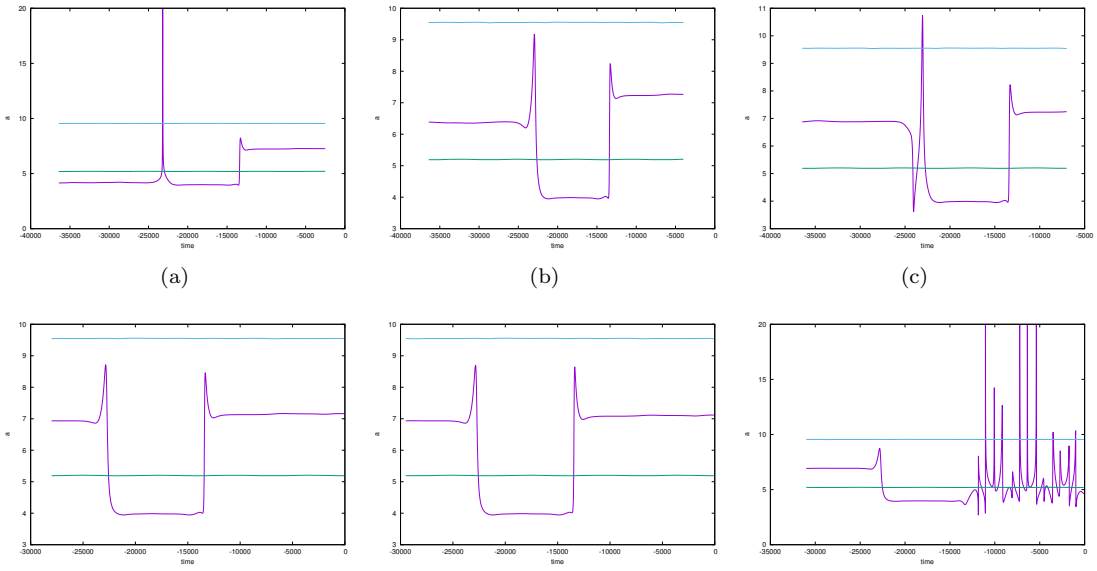

(a) (b) (c)

(d) (e) (f)

Figure 3.6: Computed semi-major axis of Jupiter, Saturn and Oterma. Units in AU and days. (a) Backward integration starting at $t = -2500$ (February 26^{th}, 1993); (b) Backward integration starting at $t = -4000$ (January 18^{th}, 1989); (c) Backward integration starting at $t = -7000$ (November 1^{st}, 1980); (d) Forward integration starting at $t = -28000$ (May 5^{th}, 1923); (e) Forward integration starting at $t = -29500$ (March 27^{th}, 1919); (f) Forward integration starting at $t = -31000$ (February 16^{th}, 1915).

and, in fact, this time can be extended for some range - as it can be seen in Figures 3.6(b) and 3.6(e) - but this extension is limited - Figures 3.6(a) and 3.6(f).

Remark: The Figure 3.6(f) requests a more careful investigation. It may seen odd, in principle, its behaviour, as one may think that the Kepler approximation for Oterma it not valid anymore, this could indicate, for instance, that Oterma, instead of orbiting the Sun, it is orbiting Jupiter after what would be the second transition. To check if that is correct, let us see Oterma's orbit.

Comparing Figures 3.7 and 3.2, we can confirm, that it is, in fact, what happens, instead of transitioning to the region between Jupiter and Saturn, Oterma starts to orbit Jupiter.

To conclude this section, let us mention that all the computations from now on, unless clearly stated the opposite, will be done by a forward integration with the initial data gathered at $t = -23500$ (August 30^{th}, 1935), as this is an initial time where Oterma's transition occur and it is located near Jupiter, so that any adaptation for the system to fit in a given model could be done with greater accuracy.

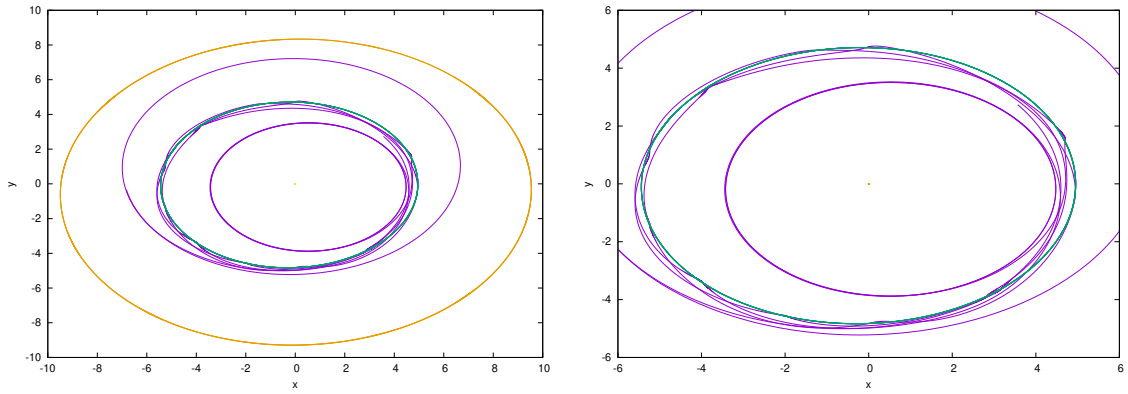

(a) (b)

Figure 3.7: Computed orbits of Jupiter (in green), Saturn (in yellow) and Oterma (in purple), with initial data gathered in $t = -31000$ (February 16^{th}, 1915).

3.4 Projecting Oterma on the Sun-Jupiter plane

All the above computations were done in a three-dimensional configuration space, even though to visualize them, they were projected. Now, in this section, we will show that it is possible to project Oterma in the plane of motion of Sun and Jupiter, and the transition will still happen.

In principle, it would be possible to project Oterma's position and velocity in many ways in the Sun-Jupiter's movement plane, so the adopted strategy was choosing a time where Oterma was close to Jupiter and orthogonally project Oterma's both position and velocity in the desired plane.

It is clear that this projection does affect its dynamics, but the transition keeps happening, as it may be seen in Figure 3.8.

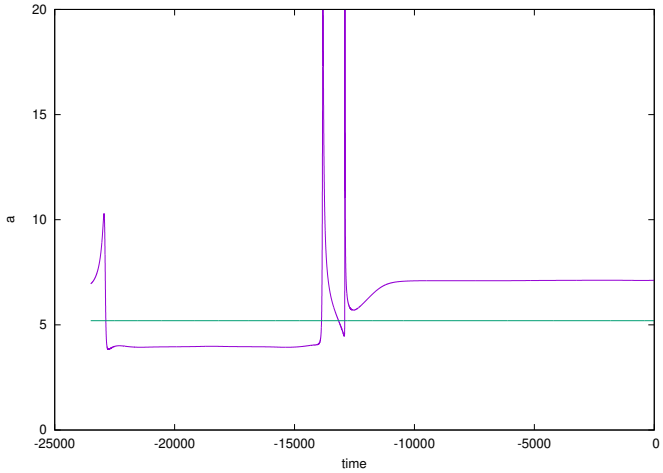

Figure 3.8: Orthogonally projected Oterma's computed semi-major axis.

It should be mentioned that, although the transition happens in the case of orthogonally projecting Oterma, analysing the Figure 3.8 one may consider, inspired by the situation of Figure 3.6(f), that Oterma does not experience a Rapid Transition Mechanism, and revolves around Jupiter. In order to check if this is the case, consider Figure 3.9.

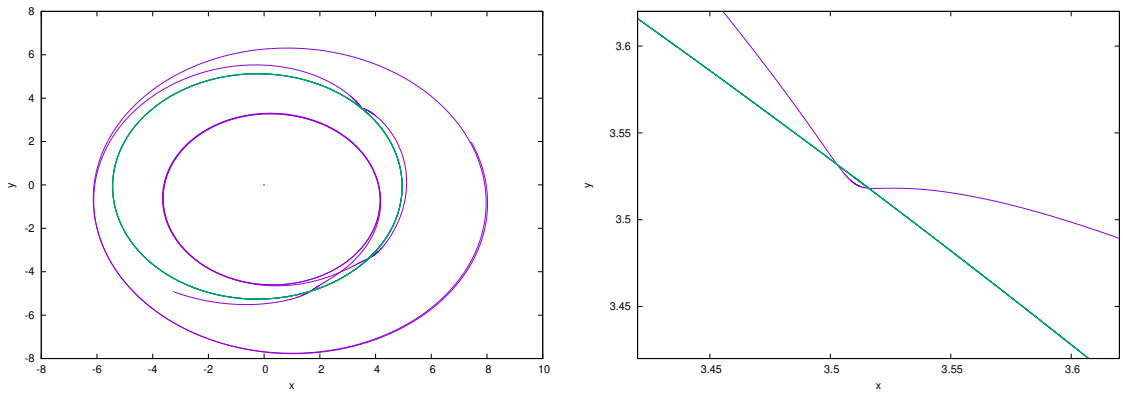

(a) (b)

Figure 3.9: Computed orbits of Jupiter (in green) and orthogonally projected Oterma (in purple), with initial data gathered in $t = -23500$ (August 30^{th}, 1935).

Comparing Figures 3.9 and 1.1(b) we may see that Oterma's behaviour is affected by the chosen projection, and comparing Figures 3.9 and 2.5 we can conclude that, in fact, this change is a revolution around Jupiter, making Oterma not to experience a Rapid Transition Mechanism.

We will, however, use this set of initial data, in this specific initial time and this projection for all the analyses we will do in this present work.

We are aware that this represents an approximation to Oterma's orbit, although it is, by itself, a rich dynamics which a lot could be worked on and it may serve as one step more in the direction of understanding and modelling Oterma's behaviour.

3.5 Choosing the Model: Planar vs. Spatial; Circular vs. Elliptical

All the computations done in this section, unless where it was stated the opposite (as in the previous section), were done in a three-dimensional configuration space and Jupiter were either in an elliptical movement, or close to it - in the case other planets were also involved in the integration of its orbit.

It is clear that, the more aspects one considers when describing and modelling a specific phenomenon,

the more precise this model will be, but also the more complex and harder to understand it.

As it was seen in Figure 1.3 even the simpler model that one could think of to describe Oterma's transition - the PCRTBP - is enough for this behaviour to exist. Both Jupiter's eccentricity and the angle which Oterma interesects the Sun-Jupiter plane of movement are small ($e \approx 0.048594036027482114$ and $\alpha \approx 2.4860378961300218°$, respectively), which justify these assumptions. However, when dealing with real data, it may be possible that this model is not enough (Figure 2.3).

There are some works done based in this behaviour that use the PCRTBP as a base model to analyse this dynamics ([KLM+01]) and, although $H = 3.03$ (the value used by them) is a possible one for Oterma, there is no clear reason for choosing this specific value and not another.

Once again, Jupiter's orbit have some eccentricity and Oterma's movement is three-dimensional, so one could think that a natural model to tackle this problem is the SERTBP.

In order to reach the SERTBP, one could think of two possibilities:

- first going to the SCRTBP and then to the SERTBP, or
- first going to the PERTBP and then to the SERTBP.

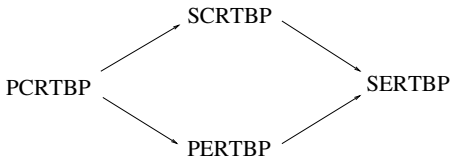

We are aware of some works in the SCRTBP ([AEL16, GL18]), but not in the PERTBP.

From the computations that were done in the Sections 2.3 and 3.4, we can see that if we project Oterma in the Sun-Jupiter's plane of movement, the transition occurs.

For the above-mentioned reasons, the decision taken here were to study the fitting of Oterma's orbit in the PERTBP, which means that, throughout the thesis we will be presenting tools to study the computation of dynamical objects related to this environment, i.e., quasi-periodic orbits (tori) and their invariant manifolds, in order to see which of them are the responsibles for Oterma's behaviour.

Chapter 4

Normal Forms Computation

In this chapter, we present some results using a semi-analytic tool in order to compute some dynamical objects in the PCRTBP.

In addition, this approach is also used to check all the numerical computation of these objects when using the tools present in Appendix A, which are the ones that will be generalized to the tori computations (Chapter 5).

All the computations done here in this chapter are based on the codes presented in [Jor99], which were modified to the cases of L_1 and L_2 points.

We refer to this paper for a more detailed explanation about the codes and about some theoretical aspects not covered here.

4.1 A Short Summary on Birkhoff Normal Forms

In this section we will be presenting some results in the theory of Birkhoff Normal Forms in order to compute them in L_1 and L_2 in the case of the circular RTBP, i.e., throughout this section, we ought to keep in mind we are thinking all the time about the specific case of the equilibrium points L_1 and L_2 in the circular RTBP. This theory is certainly more general, see for instance, [AM78, AKN88].

The approach presented here will be considering the three-dimensional problem, i.e., as if we were computing the normal forms at L_1 and L_2 for the SCRTBP, but, as we will see in the next section, it is easy to get the normal forms in the planar case having them computed to the spatial one.

The idea behind these computations that will be presented here is to use the knowledge of the behaviour

of L_1 and L_2 - namely, they are equilibrium points are of the type centre $\times$ centre $\times$ saddle - to approximate the Hamiltonian function by a polynomial in the action variables (for the hyperbolic part, $I_1 = \lambda q_1 p_1$ and, for the centre one, $I_j = \omega_j \dfrac{q_j^2 + p_j^2}{2}$, $j = 2, 3$), and to do successive changes of variables in order to get a polynomial approximation for the Hamiltonian.

More objectively, if we expand the Hamiltonian H around L_1 and L_2, we have

$$H = H_2 + H_3 + H_4 + \cdots ,$$

where H_i are homogeneous polynomials that contain all the the monomials of order i.

Remark: We start in the order 2 because there are no order 0 monomials as we can add or subtract any constant term, nor there are order 1 monomials as L_1 and L_2 are equilibrium points of the type centre $\times$ centre $\times$ saddle of a Hamiltonian system.

As we change variables for the position and momenta, we are able to eliminate some of the monomials and, after truncating to a suitable order, to get an integrable approximation of the initial Hamiltonian with which we can compute approximations of objects from the original system (equilibrium points, periodic orbits, stable/unstable manifolds, etc.).

This is done in the following way:

Let $f, g : \Sigma \longrightarrow \mathbb{R}$ be two functions on the $2n$-dimensional phase space Σ.

The Poisson bracket $\{f, g\}$ is computed by the following formula

$$\{f, g\} = \sum_{i=1}^{n} \left(\frac{\partial f}{\partial q_i} \frac{\partial g}{\partial p_i} - \frac{\partial f}{\partial p_i} \frac{\partial g}{\partial q_i} \right).$$

It has the property of, in the case of f and g being homogeneous polynomials of degree r and s respectively, $\{f, g\}$ is also a homogeneous polynomial of degree $r + s - 2$.

Suppose that there is a function, say G_3 (we will see way calling it in this way), such that

$$\tilde{H} = H + \{H, G_3\} + \frac{1}{2!}\{\{H, G_3\}, G_3\} + \frac{1}{3!}\{\{\{H, G_3\}, G_3\}, G_3\} + \cdots \tag{4.1}$$

has no order 3 monomials.

If such a function exists, we have a Hamiltonian which has order 2 (responsible for the linear behaviour of the studied system) and 4 or more.

Remark: The operation shown in Equation (4.1) defines a change of variables.

Suppose now that there is another function, say G_4 such that

$$\tilde{\tilde{H}} = \tilde{H} + \{\tilde{H}, G_4\} + \frac{1}{2!}\{\{\tilde{H}, G_4\}, G_4\} + \frac{1}{3!}\{\{\{\tilde{H}, G_4\}, G_4\}, G_4\} + \cdots$$

has no order 4 monomials.

If one is able to find this function, the Hamiltonian now will have order 2 monomials and 5 or more.

Continuing this process, we would be able to get the Hamiltonian to have just order 2 and then any arbitrarily large order monomials.

We shall see, later in this section, that this is not possible. Instead, it is possible to compute a G_4 such that $\tilde{\tilde{H}}$ is simpler. We will see what does this word "simpler" means.

Let us see first if these functions G_3, G_4, $\cdots$ exist, then how to compute them and finally if this process can be always applied or, if not, what can be done instead.

Let $H = \sum_{j=2}^{N} H_j$ be the expansion, up to order N, of the Hamiltonian.

Let each term of the above expansion be given by $H_j = \sum_{|k|=j} h_j^k q^{k_q} p^{k_p}$, $j = 3, \cdots$ where we have followed the notation presented in [Jor99]: k is a multiindex, k_q are the ones refering to the positions and k_p the ones refering to the momenta.

Notice that, for the case of the Hamiltonian (1.3), we have $H_2 = \lambda q_1 p_1 + \omega_2 \frac{q_2^2 + p_2^2}{2}$.

It is easier to handle all these computations when handling them in the field of complex numbers.

Applying the following change of variables:

$$\begin{cases} \tilde{q_j} &= \frac{q_j + i p_j}{\sqrt{2}} \\ \tilde{p_j} &= \frac{i q_j + p_j}{\sqrt{2}}, \end{cases} \tag{4.2}$$

where $i = \sqrt{-1}$ to (q_2, p_2) and (q_3, p_3) pairs and, abusing notation, calling the variables $\tilde{q_j}$, $\tilde{p_j}$ as q_j and p_j (without $\sim$) again, we have $H_2 = \lambda q_1 p_1 + i\omega_2 q_2 p_2 + i\omega_3 q_3 p_3$.

Let us analyse, with the above notations, Equation (4.1) and what does it mean to ask for it not to have order 3 monomials.

Using the bilinearity of the Poisson bracket, it is not difficult to see that the degree 3 monomials of (4.1) are H_3 and $\{H_2, G_3\}$.

So, in order to ask for $\tilde{H}$ not to have order 3 monomials, it is enough to ask $\tilde{H}_3 = H_3 + \{H_2, G_3\}$ to be zero, since we are dealing with a polynomial equation.

So, with all the above computations, we can see that G_3's coefficients should be given by

$$g_3^k = \frac{-h_3^k}{\lambda(k_1^p - k_1^q) + i\omega_2(k_2^p - k_2^q)}.$$

Notice that, in the case of an odd $|k|$ the denominator will be always different from zero, because the only possible way of it to be zero is if $k_q = k_p$.

Applying the inverse of (4.2) to the complexified variables, we have the Hamiltonian $\tilde{H}$ (that, abusing notation, we will write H again) written as

$$H = H_2 + \sum_{j=4}^{N} H_j.$$

For the case of even $|k|$, it is possible to have the case $k_q = k_p$.

In this case, let us now see that this is not a problem when considering an integrable approximation of the Hamitlonian.

Suppose that we have already eliminated the degree 3 monomials.

As $H = H_2 + \sum_{j=4}^{N} H_j$, is it not difficult to see that the degree 4 monomials of $\tilde{H} = H + \{H, G_4\} + \frac{1}{2!}\{\{H, G_4\}, G_4\} + \frac{1}{3!}\{\{\{H, G_4\}, G_4\}, G_4\} + \cdots$ are H_4 and $\{H_2, G_4\}$.

So, in order to have no degree 4 monomials, we should compute $\tilde{H}_4 = H_4 + \{H_2, G_4\} = 0$.

Analogously to what was done above, we have that G_4's coefficients should be given by

$$g_4^k = \frac{-h_4^k}{\lambda(k_1^p - k_1^q) + i\omega_2(k_2^p - k_2^q)}.$$

The problem is that, now in an even $|k|$ case, it is possible to have zero denominator (in the case of having $k_q = k_p$).

The solution for this is simple: instead of killing all the degree 4 monomials, kill just the ones where $k_q \neq k_p$.

This is not a problem for the integrability of the approximated Hamiltonian because, if we write the Hamiltonian having killed all the monomials except the ones where $k_q = k_p$, we have

$$H = H_2 + \tilde{H}_4 + \sum_{j=5}^{N} H_j,$$

where

$$\tilde{H}_4 = h_4^k q_k p_k,$$

or, writting it in action-angle variables,

$$\tilde{H}_4 = h_4^k I_k,$$

we can see that it does not depend on the angles so it is integrable.

Remark: We already have that $I_1 = \lambda q_1 p_1$ and, in complex coordinates, (i.e., applying (4.2) to the (q_2, p_2)) we have that $I_2 = i\omega_2 q_2 p_2$, so the above computation is valid.

If we continue this process until we reach N, we will have H written as

$$H(I) = \sum_{j=1}^{\lfloor N/2 \rfloor} H_{2j}(I),$$

which is an integrable Hamiltonian that approximates the original one.

Recall that the normal forms are to be computed around the desired equilibrium point, so that, in the case of this thesis, there will be two normal forms: one for L_1 and another one for L_2.

4.2 Normal Forms at L_1 and L_2 in the Planar and Circular Restricted Three-Body Problem

In [Jor99], the normal forms were computed at the triangular points L_4 and L_5, which have different behaviour than the collinear ones. For them, [Jor99] only computed the centre manifold. As we already have both codes built, it was possible to take parts of each of them to construct the normal forms for L_1 and L_2.

One of the major adaptation that were done has to do with the nature of the equilibrium points: centre $\times$ centre $\times$ centre (for the equilateral points) against saddle $\times$ centre $\times$ centre (for the collinear ones). This implies that the treatment of the variables should be different, for instance, the pair (q_1, p_1) appear in the form $q_1 p_1$ which is already diagonal and it do not need to be complexified, as stated in the previous section. In addition, the same pair, when computing the values of q_1 and p_1 from the action value, it should be noticed that the formulas to be used are not

$$\begin{cases} q_j &= \sqrt{I_j}\cos(\varphi_j) \\ p_j &= \sqrt{I_j}\sin(\varphi_j) \end{cases},$$

but

$$\begin{cases} q_j &= \sqrt{I_j}e^{\varphi_j} \\ p_j &= \sqrt{I_j}e^{-\varphi_j} \end{cases}.$$

It is important to notice that, during the application of the algorithm explained in the previous section, the positions and momenta variables are changed step after step, in such a way that in order to make sense of orbit and objects computed in these new variables we should apply an inverse transformation to recover the original variables of the system.

We should also keep in mind that this process involves the transformation of the original variables to a set of action-angle ones, so that the new and truncated Hamiltonian is now integrable, i.e, such that it does not depends on the angle variables.

So, when the normal form is computed, it will only depend on three (action) variables, two of them being the centre part and the other, the hyperbolic one. And it will be enough to prescribe some values for them to have the desired behaviour.

From this point on, we will set the value zero to the action variable corresponding to the vertical direction ($I_3 = 0$), as we will be presenting here the planar problem. With this, one of the centre action variables will always be zero, and we will consider that we have two action variables: one responsible for the centre part, and the other for the hyperbolic one.

More specifically:

- when setting both actions as zero, we have nothing other than the equilibrium point;
- if we set the centre part as non-zero and the hyperbolic as zero, we will have a Lyapunov periodic orbit around the equilibrium point.

It is important to state that, when setting these values to the action variables and computing the points (either the equilibrium or the ones belonging to the periodic orbit), these will be in the new coordinate system, i.e., after all the changes of variables that were done to put the Hamiltonian in its normal form. In order to have them in the original system, we should apply the inverse transformations.

Remark: Let us call this new set of coordinates as "normal forms" coordinates.

So far, it is not necessary to make any numerical integration.

If we would like to recover a part of the invariant stable/unstable manifolds of the equilibrium point, it is enough to give some small value to the action variable I_1, say s, set $I_2 = 0$, apply the inverse transformations to have this point in the original coordinates and integrate it in the PCRTBP flow (Equations (1.6), or we

could also give some values to this action variable, compute them in normal forms coordinates in send them to the PCRTBP coordinates via the inverse transformations.

And, to compute the invariant manifolds of the periodic orbits around L_1 and L_2, instead of integrating just the point with $I_1 = s$ variable (in the case of the figures in the next section, we have used $s = \pm 0.01$ as this small quantity), we should:

- compute the periodic orbit as above in the normal forms coordinates;
- produce meshes of points, using the previously computed periodic orbit, slightly displaced (by s) in the direction of the stable and the unstable manifolds;
- apply the inverse transformation to have these shifted orbits in the original coordinates;
- integrate these sets of points using Equations (1.6).

In other words, for each periodic orbit around an equilibrium point, we will have four sets of points to integrate (corresponding to adding the positive s to q_1, the negative s to q_1, and analogously to p_1). See Figure 4.1, where a reduction of dimension were done; a is not a point, but a periodic orbit, and its manifolds are higher dimensional.

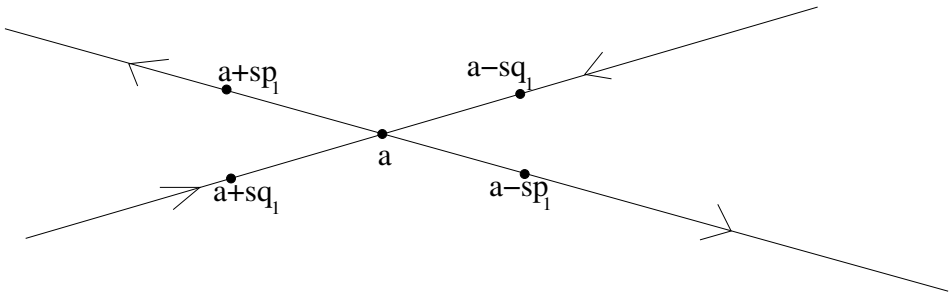

Figure 4.1: Representation of the initial sets of points to integrate to compute a local approximation to the stable and unstable manifolds of the periodic orbits around L_1 and L_2 in lower dimension

4.3 Manifolds of Periodic Orbits

Having computed these initial guesses for the stable and the unstable manifolds of the orbits around L_1 and L_2, we should numerically integrate each of them, to have the manifolds computed in a global form.

These manifolds are globally defined, though here, in the following figures, we will keep track of just a small part of them: until they reach a region where they may have an intersection.

More specifically, Figure 4.2 shows four regions (in black) until where the manifolds are computed.

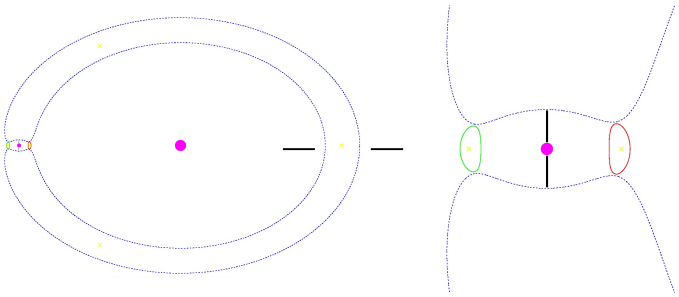

Figure 4.2: Zero-velocity curves, equilibrium points, periodic orbits around L_1 and L_2 and four regions until where the manifolds are propagated

One reason for this is because, in principle, we could numerically propagate for a long time these manifolds, but then, we would not be able to see anything or to detect any dynamical features of this system, we would just see a huge amount of points without knowing what to do with them or what conclusions take from them.

Another reason should be clarified in Section 4.4: These regions will also be Poincaré sections to the study of Oterma's transition. ([KLM+01])

Finally, Figure 4.3 shows the computed parts of the stable and unstable manifolds of the periodic orbits around L_1 and L_2.

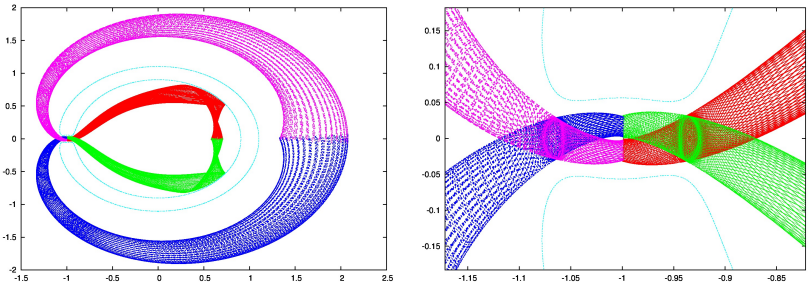

Figure 4.3: Zero-velocity curves, equilibrium points, periodic orbits around L_1 and L_2 and stable/unstable manifolds of those orbits computed using normal forms. Color scheme: (blue) stable of the p.o. around L_2; (pink) unstable of the p.o. around L_2; (red) stable of the p.o. around L_1; (green) unstable of the p.o. around L_1

4.4 Some Poincaré Sections

The phase space of the system (1.6) is four-dimensional and, due to the fact that its two degree of freedom Hamiltonian (1.3) is a first integral, it is foliated by three-dimensional invariant submanifolds, where, once the Hamiltonian value is set, the dynamics occur, so we are dealing with a problem in dimension 3.

Although it is possible to visualize two dimensional objects in $\mathbb{R}^3$ with good results, if we are able to reduce even further the dimension, without losing information, then the visualization becomes easier.

The next figures show some intersections with a Poincaré section defined by $x = -1 + \mu$ (notice that this is the x-coordiante of Jupiter).

Notice that this section is a joint of two regions described in the previous section. Also, we could investigate the other two regions (one way of defining this section would be $y = 0$ and $x > 0$, for instance), but it will be enough seeing just the ones around Jupiter.

There are energy levels where those manifolds do not intersect (Figure 4.4) and energy levels where they do (Figure 4.5).

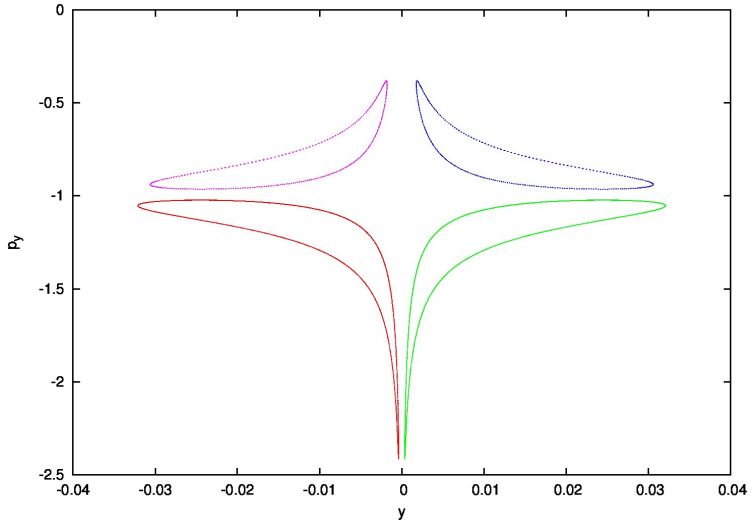

Figure 4.4: Poincaré section $x = -1 + \mu$ with $H = -1.5175$, an energy level on which the manifolds do not intersect without revolving around Jupiter

As stated in [KLM+01], the scenario illustrated in Figure 4.5 is precisely the mechanism that allows the transition phenomena experienced by Oterma, i.e., the presence of an intersection allows Oterma to transit rapidly between the different regions in the configuration space.

More specifically, as the stable and unstable manifolds of the periodic orbits around L_1 and L_2 have codimension 1, they act as separatrices. So, if Oterma is inside the region between the two manifolds, it will describe a transit orbit. ([KLM+01])

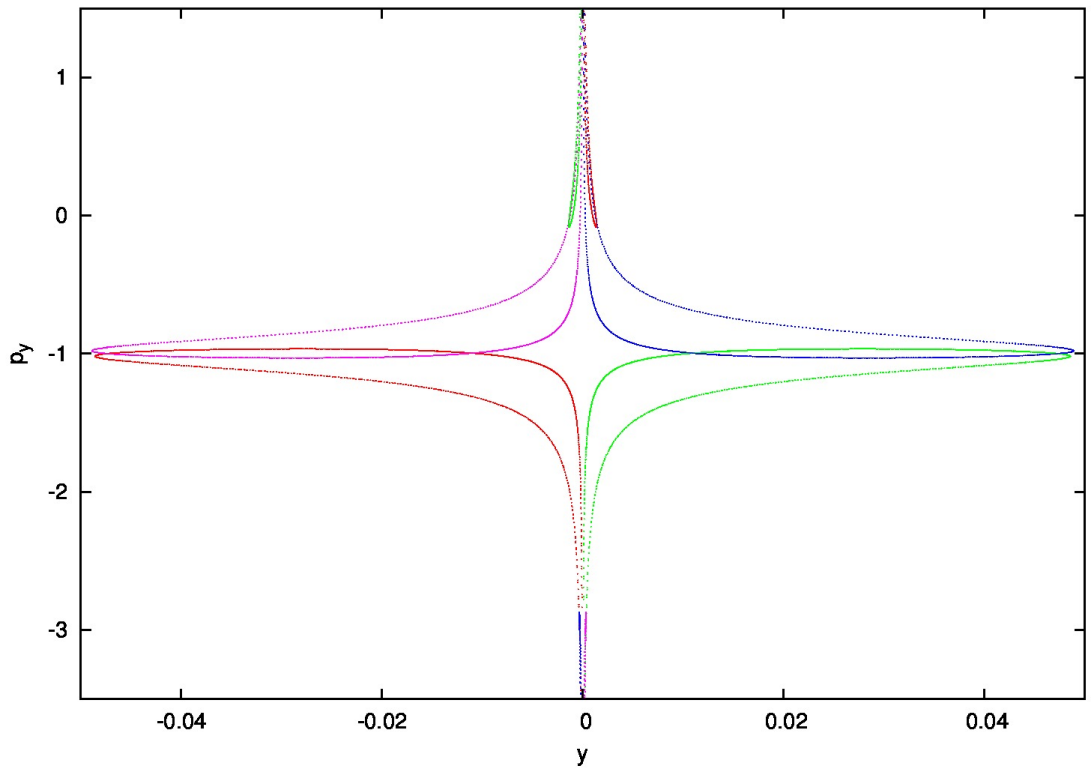

(a)

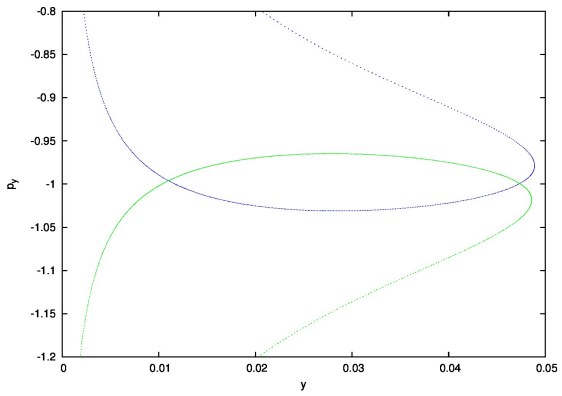

(b)

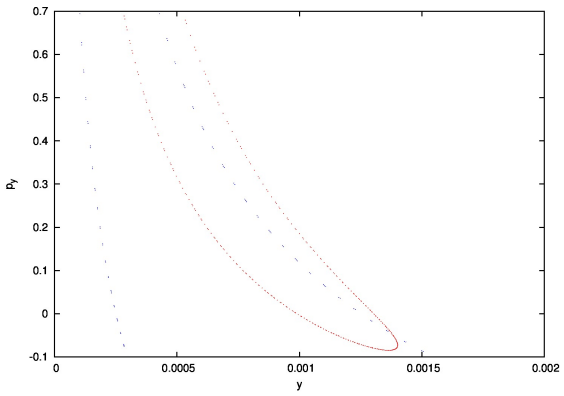

(c)

Figure 4.5: Poincaré section $x = -1 + \mu$ with $H = -1.515$ showing a heteroclinic connection between the periodic orbits around L_1 and L_2. The color scheme is the same as Figure 4.3. (a) Complete figure; (b,c) Zooms in some regions where the intersections occur.

Chapter 5

Computation of Tori and their Invariant Manifolds

This chapter can be seen as a generalization of the Appendix A, as here we will be dealing with the computation of quasi-periodic orbits.

Some details, ideas and computations will be similar and we will be referring to them whenever necessary.

Throughout this chapter the idea of computation and visualization of tori will be done by intersecting them with sections to lower the dimension. This idea will be explained in more details in the next section.

5.1 How to Compute a Torus?

The main idea behind the computation of a torus is to reduce the dimension of the problem computing, instead of a parameterization for the whole torus, one for an intersection between it and a section, and this is done in the following way.

Let $(\alpha_0, \alpha_1) \in \mathbb{T}^2$ be a set of coordinates and let $(\Omega_0, \Omega_1) \in \mathbb{R}^2$ be the vector of frequencies.

Let t be the independent variable, that we may refer it as time.

Taking as an initial condition $(0, \alpha_{1_0})$, if we integrate for time $\frac{2\pi}{\Omega_0}$, the flow lands in $(0, \alpha_{1_1})$. Integrating the flow for more $\frac{2\pi}{\Omega_0}$, it will land in $(0, \alpha_{1_2})$ and so on.

So, we may define a mapping (which will be autonomous), as the integration for time $\frac{2\pi}{\Omega_0}$: $\phi_{2\pi/\Omega_0}$, in

such a way that we transform the problem from

$$\begin{cases} \dot{x} &= f(x, \alpha_0, \alpha_1) \\ \dot{\alpha_0} &= \Omega_0 \\ \dot{\alpha_1} &= \Omega_1 \end{cases} \tag{5.1}$$

to

$$\begin{cases} \overline{x} &= P(x, \theta) \\ \overline{\theta} &= \theta + \omega \end{cases}, \tag{5.2}$$

where we have changed notation to simplify it.

In other words, we have changed our problem of computing a parameterization of a torus, considering a flow (Equation (5.1)), to computing a parameterization of an invariant curve (which will be the intersection of such torus with a section), considering a map (Equation (5.2)).

With this, the invariant curve satisfies the following equation:

$$P(x(\theta), \theta) = x(\theta + \omega), \ \forall \theta \in \mathbb{T}^1. \tag{5.3}$$

In the case where the map P is autonomous, Equation (5.3) reads

$$P(x(\theta)) = x(\theta + \omega), \ \forall \theta \in \mathbb{T}^1. \tag{5.4}$$

Remark: As in the PERTBP the map P is autonomous, from now on, the results and computations presented here will be referring to this case. In fact, recalling the formula for its Hamiltonian (Equation (1.4), with $(z, p_z) = (0, 0)$), if we integrate for 1 period of the independent variable f, this system will not depend explicitly on the angle, but only on the point in the curve. For a more general approach, we refer to [Jor01].

In [GM01] the authors explain how to compute it from a fixed point of the map (a periodic orbit in the flow).

The main idea is to give as an initial condition a circle of small radius in the direction of the centre eigenvectors, and correct it using a standard Newton's method (which will be explained still in this section).

In this case, if the small-radius curve is not enough for the problem one is dealing with, then it should be implemented a continuation scheme, that will be expained later on in this chapter.

In the case of the PERTBP, as we already have periodic orbits computed for the PCRTBP, and, due to

the fact the PCRTBP can be seen as a PERTBP with null eccentricity e, we may use this data to compute a torus, using a continuation method with e as the continuation parameter, until the desired value of e is reached.

In order to numerically approximate this invariant curve we will use a truncated Fourier series.

Remark: This idea of approximating the curve by a Fourier series is explained in [CJ00, Jor01]. We will write here some of the facts we need for the future sections.

Let $T_\omega : \mathcal{C}^0(\mathbb{T}^1, \mathbb{R}^n) \longrightarrow \mathcal{C}^0(\mathbb{T}^1, \mathbb{R}^n)$ be the translation by ω, i.e., $T_\omega(x)(\theta) = x(\theta + \omega)$.

Define $F : \mathcal{C}^0(\mathbb{T}^1, \mathbb{R}^n) \longrightarrow \mathcal{C}^0(\mathbb{T}^1, \mathbb{R}^n)$ as

$$F(x)(\theta) = P(x(\theta)) - T_\omega(x)(\theta), \ \forall x \in \mathcal{C}^0(\mathbb{T}^1, \mathbb{R}^n). \tag{5.5}$$

So, we may see that the zeroes of the operator P correspond to the invariant curves that satisfy Equation (5.4).

Let

$$x(\theta) \approx a_0 + \sum_{k=1}^{N} a_k \cos(k\theta) + b_k \sin(k\theta), \ a_0, a_k, b_k \in \mathbb{R}^n, \ \forall k = 1, \cdots, N. \tag{5.6}$$

The determination of N has to do with the accuracy of the approximation of the curve. It will be discussed later on in this section. For now, let us fix some value for it.

Before continuing, let us see that this representation is not unique and what does it imply.

Given a parameterization $x \in \mathcal{C}^0(\mathbb{T}^1, \mathbb{R}^n)$ and an angle $\varphi \in \mathbb{T}^1$, we have that both $x(\theta)$ and $x(\theta + \varphi)$ are valid ways of representing the invariant curve.

This implies that at the time of computing the solution the system will not have a unique solution.

In order to solve this, it is enough to set a specific value for one coordinate.

This implies that the system will have one equation more and the algorithm computing the zero should handle it.

It can be solved via a standard system-solving procedure, for instance, a Gaussian elimination, with pivoting. After the Gaussian elimination, the last equation should be $0 = 0$.

Given the value of N, take $2N + 1$ points on $\mathbb{T}^1$ (in other words, $2N + 1$ angles) $\theta_j = \dfrac{2\pi j}{2N + 1}$, $j = 0, \cdots, 2N$.

Assume, for now, that the Fourier coefficients a_0, a_k, b_k are known. (This will be discussed in the next subsection.)

Then, using the Inverse Fourier Transform, it is possible to compute $2N+1$ points, $x(\theta_j)$, $j = 0, \cdots, 2N$,

in the invariant curve - let us call them $x_0, x_1, \cdots, x_{2N} \in \mathbb{R}^n$.

As we have now $2N+1$ values of x, we may apply P on them to compute $P(x_0), P(x_1), \cdots, P(x_{2N})$. Call them $\overline{x_j}$, $j = 0, \cdots, 2N$.

In addition, we may also compute $T_\omega(x)(\theta_j)$, $j = 0, \cdots, 2N$. Call them x_{j_ω}, $j = 0, \cdots, 2N$.

So, we have now a set of $2N+1$ points $P(x_j) - T_\omega(x)(\theta_j)$ and we can compute a set of $2N+1$ Fourier coefficients of $P(x) - T_\omega(x)(\theta)$, using the Direct Fourier Transform. Call them $\overline{a_0}, \overline{a_k}, \overline{b_k}$, $k = 1, \cdots, N$.

Note that we have built the following mapping

$$\begin{pmatrix} a_0 \\ a_1 \\ b_1 \\ \vdots \\ a_N \\ b_N \end{pmatrix} \overset{IFT}{\longmapsto} \begin{pmatrix} x_0 \\ x_1 \\ x_2 \\ \vdots \\ x_{2N-1} \\ x_{2N} \end{pmatrix} \overset{F}{\longmapsto} \begin{pmatrix} \overline{x_0} - x_{0_\omega} \\ \overline{x_1} - x_{1_\omega} \\ \overline{x_2} - x_{2_\omega} \\ \vdots \\ \overline{x_{2N-1}} - x_{2N-1_\omega} \\ \overline{x_{2N}} - x_{2N_\omega} \end{pmatrix} \overset{DFT}{\longmapsto} \begin{pmatrix} \overline{a_0} \\ \overline{a_1} \\ \overline{b_1} \\ \vdots \\ \overline{a_N} \\ \overline{b_N} \end{pmatrix}, \tag{5.7}$$

and we will look for the zeroes of this map, by a Newton's method.

Remark: When implementing the algorithm for computing the zeroes of F, the last step of the mapping (5.7) can be skipped, as it maps 0 to 0. So, looking for zeroes of the third part is the same as looking for the ones in the fourth one, with the advantage that we save some computation time. It is definitively not the bottleneck of this computation, but when dealing with thousands of tori, each one with several evaluations of the third step, this saved time can be representative.

Remark: For practical purposes, we claim that it is preferable to allocate the vector of Fourier coefficients is $(a_0, a_1, b_1, \cdots, a_N, b_N)$, instead of $(a_0, a_1, \cdots, a_N, b_1, \cdots, b_N)$ as any change in number of Fourier modes will not force the shifting of any already allocated coefficient, in opposition to the latter case.

As we will be dealing with a Newton's method, we shall now describe how to compute some of the derivatives that appear in these computations.

Let us first compute some derivatives we will use.

As $x(\theta) = a_0 + \sum_{k=1}^{N} a_k \cos(k\theta) + b_k \sin(k\theta)$ it is not difficult to see that

$$\frac{\partial}{\partial a_0} x(\theta) = I_n, \qquad \frac{\partial}{\partial a_k} x(\theta) = I_n \cos(k\theta), \qquad \frac{\partial}{\partial b_k} x(\theta) = I_n \sin(k\theta), \qquad k = 1, \cdots, N. \tag{5.8}$$

Now, it is not difficult to compute the derivative of $P(x(\theta)) - x(\theta + \omega)$ with respect to a_0, a_k, b_k.

First, notice that, if we substitue θ by $\theta + \omega$ in (5.8), this part is solved.

In order to compute the derivatives of $P(x(\theta))$ we will use the chain rule, as

$$\frac{\partial}{\partial a_0} P(x(\theta)) = D_x P(x(\theta)) \frac{\partial}{\partial a_0} x(\theta),$$

(analogously to $\frac{\partial}{\partial a_k} P(x(\theta))$ and $\frac{\partial}{\partial b_k} P(x(\theta))$, $k = 1, \cdots, N$) where $D_x P(x(\theta))$ is the variational matrix of P.

Finally, let us briefly discuss how to determine N.

After succesfully computing, via a Newton's method, a good set of Fourier coefficients to approximate the invariant curve, it is a good idea to check this approximation in a finer mesh, i.e., for the $2N + 1$ computed points, the approximation given by N Fourier modes is accurate enough (for our case, in the PERTBP, unless when strictly mentioned, we have used an tolerance value of 10^{-12}), now let us compute this accuracy in more points.

Let $E(x, \omega) = \max_{\theta \in \mathbb{T}^1} |F(x)(\theta)|$ be the error function. Recall that we are computing the zeroes of the operator F.

Computing E for the initial mesh when the Newton's method was succesfully applied will give us the desired accuracy asked in the method.

Now if we increase the number of points (in the case of the PERTBP, we have used $100N$ points), this function tend to grow, so that, if we control its growth, we will be able to rely more in the computed approximation.

So, given an initial, arbitrarily defined, N, compute the approximation of the operator F via the above-explained Newton's method. After this, compute the error function, in case it is smaller than the desired accuracy, then the approximation of the curve was succesfully computed, if not, increase N and repeat all the computations until the tolerance is reached.

5.1.1 Initial Conditions

Now, we shall discuss the computation of the initial conditions.

In the general case, where we start from a fixed point and compute the invariant curve ([GM01]), the initial condition, as it was already mentioned is a circle of small radius in the direction of the eigenvector related to the centre part, and, as the determination of N was already discussed, we shall proceed to the case of the PERTBP.

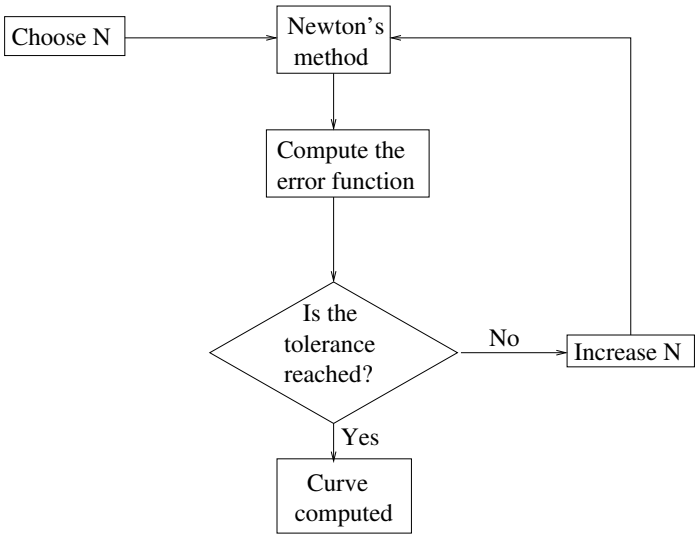

Figure 5.1: Algorithm for the determination of N.

For the PERTBP, as we already have periodic orbits computed for the PCRTBP and we have implemented a continuation scheme using e as the continuation parameter, in order to begin this continuation, we should give an initial guess for the Fourier coefficients.

Let us see now how this was done.

Given a periodic orbit and a value of N (we have chosen the one related to $H = -1.5175$ and $N = 20$) build a mesh of $2N + 1$ points in the orbit - remember that the orbit is given by a point in the orbit and in a section, so to produce a set of $2N + 1$ points, it is enough to integrate it using the PCRTBP flow (1.6) - and, from this mesh, compute a set of Fourier coefficients to be corrected by the Newton's method.

The process of continuation of tori will be explained in Section 5.4, for now, let us assume that it is possible to be done and that, at each step, the Fourier coefficients are corrected.

At the end of this process (when we reach the value of the eccentricity of the Sun-Jupiter orbit) we will have a set of initial conditions for a torus around one of the equilibrium points in the PERTBP.

Remark: These computations were all done with parallel shooting, so the details will be presented in the next section.

5.1.2 Variational Flow

Recalling the system of ODEs representing the PERTBP (Equations (1.7)), the differential matrix will assume a similar form as the one for the PCRTBP (A.4):

$$\begin{pmatrix} \frac{\partial x'}{\partial x} & \frac{\partial x'}{\partial y} & \frac{\partial x'}{\partial p_x} & \frac{\partial x'}{\partial p_y} \\ \frac{\partial y'}{\partial x} & \frac{\partial y'}{\partial y} & \frac{\partial y'}{\partial p_x} & \frac{\partial y'}{\partial p_y} \\ \frac{\partial p'_x}{\partial x} & \frac{\partial p'_x}{\partial y} & \frac{\partial p'_x}{\partial p_x} & \frac{\partial p'_x}{\partial p_y} \\ \frac{\partial p'_y}{\partial x} & \frac{\partial p'_y}{\partial y} & \frac{\partial p'_y}{\partial p_x} & \frac{\partial p'_y}{\partial p_y} \end{pmatrix} = \begin{pmatrix} 0 & 1 & 1 & 0 \\ -1 & 0 & 0 & 1 \\ \frac{\partial p'_x}{\partial x} & \frac{\partial p'_x}{\partial y} & 0 & 1 \\ \frac{\partial p'_y}{\partial x} & \frac{\partial p'_y}{\partial y} & -1 & 0 \end{pmatrix}, \tag{5.9}$$

where

- $\frac{\partial p'_x}{\partial x} = -1 + \frac{1}{1+e\cos f} \cdot \left(1 - \frac{(1-\mu)(r_1^2 - 3(x-\mu)^2)}{r_1^5} - \frac{\mu(r_2^2 - 3(x+1-\mu)^2)}{r_2^5}\right)$;
- $\frac{\partial p'_x}{\partial y} = \frac{\partial p'_y}{\partial x} = \frac{1}{1+e\cos f} \cdot \left(3\frac{(1-\mu)(x-\mu)y}{r_1^5} + 3\frac{\mu(x+1-\mu)y}{r_2^5}\right)$;
- $\frac{\partial p'_y}{\partial y} = -1 + \frac{1}{1+e\cos f} \cdot \left(1 - \frac{(1-\mu)(r_1^2 - 3y^2)}{r_1^5} - \frac{\mu(r_2^2 - 3y^2)}{r_2^5}\right)$.

To explicit some computations, let us write the variational matrix as

$$\begin{pmatrix} \frac{\partial F_0}{\partial a_0} & \frac{\partial F_0}{\partial a_1} & \cdots & \frac{\partial F_0}{\partial a_N} & \frac{\partial F_0}{\partial b_1} & \cdots & \frac{\partial F_0}{\partial b_N} \\ \frac{\partial F_1}{\partial a_0} & \frac{\partial F_1}{\partial a_1} & \cdots & \frac{\partial F_1}{\partial a_N} & \frac{\partial F_1}{\partial b_1} & \cdots & \frac{\partial F_1}{\partial b_N} \\ \vdots & \vdots & \ddots & \vdots & \vdots & \ddots & \vdots \\ \frac{\partial F_N}{\partial a_0} & \frac{\partial F_N}{\partial a_1} & \cdots & \frac{\partial F_N}{\partial a_N} & \frac{\partial F_N}{\partial b_1} & \cdots & \frac{\partial F_N}{\partial b_N} \\ \frac{\partial F_{N+1}}{\partial a_0} & \frac{\partial F_{N+1}}{\partial a_1} & \cdots & \frac{\partial F_{N+1}}{\partial a_N} & \frac{\partial F_{N+1}}{\partial b_1} & \cdots & \frac{\partial F_{N+1}}{\partial b_N} \\ \vdots & \vdots & \ddots & \vdots & \vdots & \ddots & \vdots \\ \frac{\partial F_{2N}}{\partial a_0} & \frac{\partial F_{2N}}{\partial a_1} & \cdots & \frac{\partial F_{2N}}{\partial a_N} & \frac{\partial F_{2N}}{\partial b_1} & \cdots & \frac{\partial F_{2N}}{\partial b_N} \end{pmatrix}. \tag{5.10}$$

Notice that, in the case of the PERTBP, each of the components of the above matrix is a 4×4 matrix. Let us see now how to write some of these blocks.

$$
\begin{aligned}
\frac{\partial F_j}{\partial a_0} &= D_x P(x(\theta_j))\frac{\partial x}{\partial a_0}(\theta_j) - \frac{\partial x}{\partial a_0}(\theta_j+\omega) \\
&= \begin{pmatrix} v_{11}^{\theta_j} & v_{12}^{\theta_j} & v_{13}^{\theta_j} & v_{14}^{\theta_j} \\ v_{21}^{\theta_j} & v_{22}^{\theta_j} & v_{23}^{\theta_j} & v_{24}^{\theta_j} \\ v_{31}^{\theta_j} & v_{32}^{\theta_j} & v_{33}^{\theta_j} & v_{34}^{\theta_j} \\ v_{41}^{\theta_j} & v_{42}^{\theta_j} & v_{43}^{\theta_j} & v_{44}^{\theta_j} \end{pmatrix} \begin{pmatrix} 1&0&0&0 \\ 0&1&0&0 \\ 0&0&1&0 \\ 0&0&0&1 \end{pmatrix} - \begin{pmatrix} 1&0&0&0 \\ 0&1&0&0 \\ 0&0&1&0 \\ 0&0&0&1 \end{pmatrix} \\
&= \begin{pmatrix} v_{11}^{\theta_j}-1 & v_{12}^{\theta_j} & v_{13}^{\theta_j} & v_{14}^{\theta_j} \\ v_{21}^{\theta_j} & v_{22}^{\theta_j}-1 & v_{23}^{\theta_j} & v_{24}^{\theta_j} \\ v_{31}^{\theta_j} & v_{32}^{\theta_j} & v_{33}^{\theta_j}-1 & v_{34}^{\theta_j} \\ v_{41}^{\theta_j} & v_{42}^{\theta_j} & v_{43}^{\theta_j} & v_{44}^{\theta_j}-1 \end{pmatrix} \\
\frac{\partial F_j}{\partial a_k} &= D_x P(x(\theta_j))\frac{\partial x}{\partial a_k}(\theta_j) - \frac{\partial x}{\partial a_k}(\theta_j+\omega) \\
&= \begin{pmatrix} v_{11}^{\theta_j} & v_{12}^{\theta_j} & v_{13}^{\theta_j} & v_{14}^{\theta_j} \\ v_{21}^{\theta_j} & v_{22}^{\theta_j} & v_{23}^{\theta_j} & v_{24}^{\theta_j} \\ v_{31}^{\theta_j} & v_{32}^{\theta_j} & v_{33}^{\theta_j} & v_{34}^{\theta_j} \\ v_{41}^{\theta_j} & v_{42}^{\theta_j} & v_{43}^{\theta_j} & v_{44}^{\theta_j} \end{pmatrix} \begin{pmatrix} \cos(k\theta_j) & 0 & 0 & 0 \\ 0 & \cos(k\theta_j) & 0 & 0 \\ 0 & 0 & \cos(k\theta_j) & 0 \\ 0 & 0 & 0 & \cos(k\theta_j) \end{pmatrix} - \begin{pmatrix} \cos(k\theta_j+k\omega) & 0 & 0 & 0 \\ 0 & \cos(k\theta_j+k\omega) & 0 & 0 \\ 0 & 0 & \cos(k\theta_j+k\omega) & 0 \\ 0 & 0 & 0 & \cos(k\theta_j+k\omega) \end{pmatrix} \\
&= \begin{pmatrix} v_{11}^{\theta_j}\cos(k\theta_j)-\cos(k\theta_j+k\omega) & v_{12}^{\theta_j}\cos(k\theta_j) & v_{13}^{\theta_j}\cos(k\theta_j) & v_{14}^{\theta_j}\cos(k\theta_j) \\ v_{21}^{\theta_j}\cos(k\theta_j) & v_{22}^{\theta_j}\cos(k\theta_j)-\cos(k\theta_j+k\omega) & v_{23}^{\theta_j}\cos(k\theta_j) & v_{24}^{\theta_j}\cos(k\theta_j) \\ v_{31}^{\theta_j}\cos(k\theta_j) & v_{32}^{\theta_j}\cos(k\theta_j) & v_{33}^{\theta_j}\cos(k\theta_j)-\cos(k\theta_j+k\omega) & v_{34}^{\theta_j}\cos(k\theta_j) \\ v_{41}^{\theta_j}\cos(k\theta_j) & v_{42}^{\theta_j}\cos(k\theta_j) & v_{43}^{\theta_j}\cos(k\theta_j) & v_{44}^{\theta_j}\cos(k\theta_j)-\cos(k\theta_j+k\omega) \end{pmatrix} \\
\frac{\partial F_j}{\partial b_k} &= D_x P(x(\theta_j))\frac{\partial x}{\partial b_k}(\theta_j) - \frac{\partial x}{\partial b_k}(\theta_j+\omega) \\
&= \begin{pmatrix} v_{11}^{\theta_j} & v_{12}^{\theta_j} & v_{13}^{\theta_j} & v_{14}^{\theta_j} \\ v_{21}^{\theta_j} & v_{22}^{\theta_j} & v_{23}^{\theta_j} & v_{24}^{\theta_j} \\ v_{31}^{\theta_j} & v_{32}^{\theta_j} & v_{33}^{\theta_j} & v_{34}^{\theta_j} \\ v_{41}^{\theta_j} & v_{42}^{\theta_j} & v_{43}^{\theta_j} & v_{44}^{\theta_j} \end{pmatrix} \begin{pmatrix} \sin(k\theta_j) & 0 & 0 & 0 \\ 0 & \sin(k\theta_j) & 0 & 0 \\ 0 & 0 & \sin(k\theta_j) & 0 \\ 0 & 0 & 0 & \sin(k\theta_j) \end{pmatrix} - \begin{pmatrix} \sin(k\theta_j+k\omega) & 0 & 0 & 0 \\ 0 & \sin(k\theta_j+k\omega) & 0 & 0 \\ 0 & 0 & \sin(k\theta_j+k\omega) & 0 \\ 0 & 0 & 0 & \sin(k\theta_j+k\omega) \end{pmatrix} \\
&= \begin{pmatrix} v_{11}^{\theta_j}\sin(k\theta_j)-\sin(k\theta_j+k\omega) & v_{12}^{\theta_j}\sin(k\theta_j) & v_{13}^{\theta_j}\sin(k\theta_j) & v_{14}^{\theta_j}\sin(k\theta_j) \\ v_{21}^{\theta_j}\sin(k\theta_j) & v_{22}^{\theta_j}\sin(k\theta_j)-\sin(k\theta_j+k\omega) & v_{23}^{\theta_j}\sin(k\theta_j) & v_{24}^{\theta_j}\sin(k\theta_j) \\ v_{31}^{\theta_j}\sin(k\theta_j) & v_{32}^{\theta_j}\sin(k\theta_j) & v_{33}^{\theta_j}\sin(k\theta_j)-\sin(k\theta_j+k\omega) & v_{34}^{\theta_j}\sin(k\theta_j) \\ v_{41}^{\theta_j}\sin(k\theta_j) & v_{42}^{\theta_j}\sin(k\theta_j) & v_{43}^{\theta_j}\sin(k\theta_j) & v_{44}^{\theta_j}\sin(k\theta_j)-\sin(k\theta_j+k\omega) \end{pmatrix},
\end{aligned}
$$

where $j = 0, \cdots, 2N$, $k = 1, \cdots, N$ and $v_{mn}^{\theta_j}$ is the component mn of the variational matrix of $x(\theta_j)$.

5.1.3 Projection into a Temporal Section

In opposition to the projection in a spatial section, in order to project in a temporal section, it is not needed to compute any approximation of vectors or consider some specific components.

Remark: It is not accurate to call, when considering the PERTBP as we are here, these sections as "temporal" ones, because the independent variable is not the time but the true anomaly. We will, however, be using this way of describing them.

In fact, when integrating for the specific time so that the flow ends in a section, the point itself belongs to this section and the vectors of the variational matrix belong to the tangent space to it, so there is not the problem of vectors lying outside of where they should be in order to the map to be well defined.

In the case of the PERTBP, it can be seen as a 2π periodic perturbation of the PCRTBP, so the integration time is 2π.

5.2 Parallel Shooting

The idea of the parallel shooting technique was already explained in Appendix A, so from now on, we will restrict ourselves to the particularities of this tool in the case of the PERTBP.

Let us see now, how to write the computations to be done.

Let Σ be the phase space of the PERTBP.

Let Σ_α be the intersection between Σ and the manifold $\{(x, y, p_x, p_y, f) \in \Sigma \subset \mathbb{R}^4 \times \mathbb{T}^1 / f = \alpha\}$.

We will be using 4 sections in the true anomaly (the independent variable).

Let

$$P^0 : \Sigma_0 \longrightarrow \Sigma_{\frac{\pi}{2}},$$
$$P^1 : \Sigma_{\frac{\pi}{2}} \longrightarrow \Sigma_{\pi},$$
$$P^2 : \Sigma_{\pi} \longrightarrow \Sigma_{\frac{3\pi}{2}},$$
$$P^3 : \Sigma_{\frac{3\pi}{2}} \longrightarrow \Sigma_{2\pi},$$

be given by the $\frac{\pi}{2}$ flow.

So, we can see that $P = P^3 \circ P^2 \circ P^1 \circ P^0$.

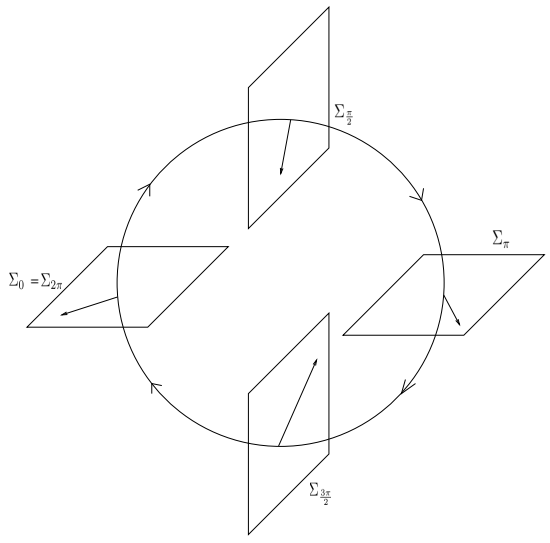

Figure 5.2: Illustration of the parallel shooting used in this thesis for the PERTBP: 4 sections in the independent variable.

Instead of looking for a parameterization x of the torus such that $P(x(\theta)) = x(\theta + \omega)$ we will be looking

at four parameterizations (one for each section, call them x_i, $i = 0, 1, 2, 3$, each one related to $\Sigma_{\frac{i\pi}{2}}$) such that

$$\begin{cases} P^0(x_0(\theta)) &= x_1(\theta) \\ P^1(x_1(\theta)) &= x_2(\theta) \\ P^2(x_2(\theta)) &= x_3(\theta) \\ P^3(x_3(\theta)) &= T_\omega(x_0(\theta)) \end{cases} . \tag{5.11}$$

Remark: It would be possible to write the system (5.11) as

$$\begin{cases} P^0(x_0(\theta)) &= T_{\omega/4}(x_1(\theta)) \\ P^1(x_1(\theta)) &= T_{\omega/4}(x_2(\theta)) \\ P^2(x_2(\theta)) &= T_{\omega/4}(x_3(\theta)) \\ P^3(x_3(\theta)) &= T_{\omega/4}(x_0(\theta)) \end{cases} ,$$

i.e., instead of counting on the twist by ω just at the end of the application of the 4 maps, counting it by parts, in each mapping. For practical purposes there is no difference between these two systems, they are just two different ways of parameterizing the invariant curves in the sections. In this thesis, we have used the system (5.11).

Remark: Notice that solving the system (5.11) is equivalent to finding a solution for the invariance equation (5.4). In fact, as $P = P^3 \circ P^2 \circ P^1 \circ P^0$, we have that

$$\begin{aligned} P(x_0(\theta)) = x_0(\theta + \omega) &\iff P^3(P^2(P^1(P^0(x_0(\theta))))) = T_\omega(x_0(\theta)) \\ &\iff P^3(P^2(P^1(x_1(\theta)))) = T_\omega(x_0(\theta)) \\ &\iff P^3(P^2(x_2(\theta))) = T_\omega(x_0(\theta)) \\ &\iff P^3(x_3(\theta)) = T_\omega(x_0(\theta)). \end{aligned}$$

The system (5.11) can be written (using a similar notation as before) as

$$\begin{cases} F^0(x)(\theta) &= P^0(x_0(\theta)) - x_1(\theta) \\ F^1(x)(\theta) &= P^1(x_1(\theta)) - x_2(\theta) \\ F^2(x)(\theta) &= P^2(x_2(\theta)) - x_3(\theta) \\ F^3(x)(\theta) &= P^3(x_3(\theta)) - T_\omega(x_0(\theta)). \end{cases} \tag{5.12}$$

where we are using the notation $x = (x_0, x_1, x_2, x_3)$.

Let us see now how to build the differential matrix.

As each section will have a parameterization, let a_{0i}, a_{ji}, b_{ji}, $i = 0, 1, 2, 3$ representing the sections $\Sigma_{\frac{i\pi}{2}}$.

So, the derivative matrix is given by

$$\begin{pmatrix} \begin{pmatrix} \frac{\partial F^0}{\partial a_{00}} & \frac{\partial F^0}{\partial a_{j0}} & \frac{\partial F^0}{\partial b_{j0}} \end{pmatrix} \begin{pmatrix} \frac{\partial F^0}{\partial a_{01}} & \frac{\partial F^0}{\partial a_{j1}} & \frac{\partial F^0}{\partial b_{j1}} \end{pmatrix} \begin{pmatrix} \frac{\partial F^0}{\partial a_{02}} & \frac{\partial F^0}{\partial a_{j2}} & \frac{\partial F^0}{\partial b_{j2}} \end{pmatrix} \begin{pmatrix} \frac{\partial F^0}{\partial a_{03}} & \frac{\partial F^0}{\partial a_{j3}} & \frac{\partial F^0}{\partial b_{j3}} \end{pmatrix} \\ \begin{pmatrix} \frac{\partial F^1}{\partial a_{00}} & \frac{\partial F^1}{\partial a_{j0}} & \frac{\partial F^1}{\partial b_{j0}} \end{pmatrix} \begin{pmatrix} \frac{\partial F^1}{\partial a_{01}} & \frac{\partial F^1}{\partial a_{j1}} & \frac{\partial F^1}{\partial b_{j1}} \end{pmatrix} \begin{pmatrix} \frac{\partial F^1}{\partial a_{02}} & \frac{\partial F^1}{\partial a_{j2}} & \frac{\partial F^1}{\partial b_{j2}} \end{pmatrix} \begin{pmatrix} \frac{\partial F^1}{\partial a_{03}} & \frac{\partial F^1}{\partial a_{j3}} & \frac{\partial F^1}{\partial b_{j3}} \end{pmatrix} \\ \begin{pmatrix} \frac{\partial F^2}{\partial a_{00}} & \frac{\partial F^2}{\partial a_{j0}} & \frac{\partial F^2}{\partial b_{j0}} \end{pmatrix} \begin{pmatrix} \frac{\partial F^2}{\partial a_{01}} & \frac{\partial F^2}{\partial a_{j1}} & \frac{\partial F^2}{\partial b_{j1}} \end{pmatrix} \begin{pmatrix} \frac{\partial F^2}{\partial a_{02}} & \frac{\partial F^2}{\partial a_{j2}} & \frac{\partial F^2}{\partial b_{j2}} \end{pmatrix} \begin{pmatrix} \frac{\partial F^2}{\partial a_{03}} & \frac{\partial F^2}{\partial a_{j3}} & \frac{\partial F^2}{\partial b_{j3}} \end{pmatrix} \\ \begin{pmatrix} \frac{\partial F^3}{\partial a_{00}} & \frac{\partial F^3}{\partial a_{j0}} & \frac{\partial F^3}{\partial b_{j0}} \end{pmatrix} \begin{pmatrix} \frac{\partial F^3}{\partial a_{01}} & \frac{\partial F^3}{\partial a_{j1}} & \frac{\partial F^3}{\partial b_{j1}} \end{pmatrix} \begin{pmatrix} \frac{\partial F^3}{\partial a_{02}} & \frac{\partial F^3}{\partial a_{j2}} & \frac{\partial F^3}{\partial b_{j2}} \end{pmatrix} \begin{pmatrix} \frac{\partial F^3}{\partial a_{03}} & \frac{\partial F^3}{\partial a_{j3}} & \frac{\partial F^3}{\partial b_{j3}} \end{pmatrix} \end{pmatrix}.$$

Notice that each submatrix is a $4(2N+1) \times 4(2N+1)$-dimensional matrix, where the first part is $4(2N+1) \times 4$ and the second and third ones $4(2N+1) \times 4N$ each; the number 4 comes from the dimension of Σ_α.

From (5.11) we can see that the first equation depends only on x_0 and x_1, which means that F^0 will not depend on a_{j2}, b_{j2}, a_{j3} and b_{j3}, so that the third and fourth submatrices of the derivative matrix are null.

Analogously, we can see that the components $(1,0)$, $(1,3)$, $(2,0)$, $(2,1)$, $(3,1)$ and $(3,2)$ are null.

In addition, still from (5.11), we can compute some of the components to get

$$\begin{pmatrix} \begin{pmatrix} \frac{\partial P^0}{\partial a_{00}}\Big|_\theta & \frac{\partial P^0}{\partial a_{j0}}\Big|_\theta & \frac{\partial P^0}{\partial b_{j0}}\Big|_\theta \end{pmatrix} & -\begin{pmatrix} \frac{\partial x_1}{\partial a_{01}}\Big|_\theta & \frac{\partial x_1}{\partial a_{j1}}\Big|_\theta & \frac{\partial x_1}{\partial b_{j1}}\Big|_\theta \end{pmatrix} & 0 & 0 \\ 0 & \begin{pmatrix} \frac{\partial P^1}{\partial a_{01}}\Big|_\theta & \frac{\partial P^1}{\partial a_{j1}}\Big|_\theta & \frac{\partial P^1}{\partial b_{j1}}\Big|_\theta \end{pmatrix} & -\begin{pmatrix} \frac{\partial x_2}{\partial a_{02}}\Big|_\theta & \frac{\partial x_2}{\partial a_{j2}}\Big|_\theta & \frac{\partial x_2}{\partial b_{j2}}\Big|_\theta \end{pmatrix} & 0 \\ 0 & 0 & \begin{pmatrix} \frac{\partial P^2}{\partial a_{02}}\Big|_\theta & \frac{\partial P^2}{\partial a_{j2}}\Big|_\theta & \frac{\partial P^2}{\partial b_{j2}}\Big|_\theta \end{pmatrix} & -\begin{pmatrix} \frac{\partial x_3}{\partial a_{03}}\Big|_\theta & \frac{\partial x_3}{\partial a_{j3}}\Big|_\theta & \frac{\partial x_3}{\partial b_{j3}}\Big|_\theta \end{pmatrix} \\ -\begin{pmatrix} \frac{\partial x_0}{\partial a_{00}}\Big|_{\theta+\omega} & \frac{\partial x_0}{\partial a_{j0}}\Big|_{\theta+\omega} & \frac{\partial x_0}{\partial b_{j0}}\Big|_{\theta+\omega} \end{pmatrix} & 0 & 0 & \begin{pmatrix} \frac{\partial P^3}{\partial a_{03}}\Big|_\theta & \frac{\partial P^3}{\partial a_{j3}}\Big|_\theta & \frac{\partial P^3}{\partial b_{j3}}\Big|_\theta \end{pmatrix} \end{pmatrix}, \tag{5.13}$$

where

$$\begin{pmatrix} \frac{\partial x_i}{\partial a_{0i}}\Big|_\theta & \frac{\partial x_i}{\partial a_{ji}}\Big|_\theta & \frac{\partial x_i}{\partial b_{ji}}\Big|_\theta \end{pmatrix} = \begin{pmatrix} I & I\cos(\theta_0) & I\cos(2\theta_0) & \cdots & I\cos(N\theta_0) & I\sin(\theta_0) & I\sin(2\theta_0) & \cdots & I\sin(N\theta_0) \\ I & I\cos(\theta_1) & I\cos(2\theta_1) & \cdots & I\cos(N\theta_1) & I\sin(\theta_1) & I\sin(2\theta_1) & \cdots & I\sin(N\theta_1) \\ \vdots & \vdots & \vdots & \vdots & \vdots & \vdots & \vdots & \vdots & \vdots \\ I & I\cos(\theta_{2N}) & I\cos(2\theta_{2N}) & \cdots & I\cos(N\theta_{2N}) & I\sin(\theta_{2N}) & I\sin(2\theta_{2N}) & \cdots & I\sin(N\theta_{2N}) \end{pmatrix},$$

$$\left(\left.\frac{\partial P^i}{\partial a_{0i}}\right|_\theta \quad \left.\frac{\partial P^i}{\partial a_{ji}}\right|_\theta \quad \left.\frac{\partial P^i}{\partial b_{ji}}\right|_\theta\right) =$$
$$\begin{pmatrix} V^{\theta_0} & V^{\theta_0}\cos(\theta_0) & V^{\theta_0}\cos(2\theta_0) & \cdots & V^{\theta_0}\cos(N\theta_0) & V^{\theta_0}\sin(\theta_0) & V^{\theta_0}\sin(2\theta_0) & \cdots & V^{\theta_0}\sin(N\theta_0) \\ V^{\theta_1} & V^{\theta_1}\cos(\theta_1) & V^{\theta_1}\cos(2\theta_1) & \cdots & V^{\theta_1}\cos(N\theta_1) & V^{\theta_1}\sin(\theta_1) & V^{\theta_1}\sin(2\theta_1) & \cdots & V^{\theta_1}\sin(N\theta_1) \\ \vdots & \vdots & \vdots & \vdots & \vdots & \vdots & \vdots & \vdots & \vdots \\ V^{\theta_{2N}} & V^{\theta_{2N}}\cos(\theta_{2N}) & V^{\theta_{2N}}\cos(2\theta_{2N}) & \cdots & V^{\theta_{2N}}\cos(N\theta_{2N}) & V^{\theta_{2N}}\sin(\theta_{2N}) & V^{\theta_{2N}}\sin(2\theta_{2N}) & \cdots & V^{\theta_{2N}}\sin(N\theta_{2N}) \end{pmatrix},$$

$j = 1, \cdots, N$,$i = 0, 1, 2, 3$, $I = I_{4\times 4}$ and

$$V^{\theta_k} = \begin{pmatrix} v_{11}^{\theta_k} & v_{12}^{\theta_k} & v_{13}^{\theta_k} & v_{14}^{\theta_k} \\ v_{21}^{\theta_k} & v_{22}^{\theta_k} & v_{23}^{\theta_k} & v_{24}^{\theta_k} \\ v_{31}^{\theta_k} & v_{32}^{\theta_k} & v_{33}^{\theta_k} & v_{34}^{\theta_k} \\ v_{41}^{\theta_k} & v_{42}^{\theta_k} & v_{43}^{\theta_k} & v_{44}^{\theta_k} \end{pmatrix}.$$

To finish this section, we would like to emphasize the structure of the differential matrix of the Newton's method.

Recall that, in the case of a single shooting (Section 5.1) the matrix is given by Equation (5.10) - together with the following ones explaining the meaning of each term - where we have a structure of a matrix of matrices of total dimension of $4 \cdot (2N + 1) \times 4 \cdot (2N + 1)$, where the number 4 accounts for the dimension of the phase space and $2N + 1$ is the number of points in the invariant curve that we compute the approximation of the parameterization.

Now, in the case of a parallel shooting, in Equation (5.13) each block in the diagonal has the form of Equation (5.10), meaning that we have a structure of a matrix of matrices of matrices, with a total dimension of $4 \cdot 4 \cdot (2N + 1) \times 4 \cdot 4 \cdot (2N + 1)$, where the numbers 4 and $2N + 1$ are as above and the new 4 is due to the number of Poincaré sections.

Analogously to the single shooting situation, in the parallel shooting, we should add one equation more to compute the unique representation of the torus, and the algorithm to solve the system should take this into consideration.

In addition, we finish this section discussing the computation of the initial conditions.

In the case of a single shooting, we have stated that the initial conditions are computed using a continuation scheme, seen the PCRTBP as as PERTBP with $e = 0$, until we reach the eccentricity we use to the Sun-Jupiter system ($e \approx 0.048594036027482114$), given some periodic orbit.

If we are using the parallel shooting - which is, indeed, the case - initial conditions should be given for

each Poincaré section $\Sigma_{\frac{i\pi}{2}}$, $i = 0, 1, 2, 3$.

We start by computing four different parameterizations for the periodic orbit with $e = 0$, each one with a difference of a shift by φ from the previous one.

This difference is obtained by integrating the PCRTBP flow by $\dfrac{\pi}{2}$ units of time.

From each of this, say, initial curves, we start the continuation process unitil we reach the Sun-Jupiter system eccentricity.

Figure 5.3 shows the curves of continuation of each of these orbits (around L_2), being the y-axis the value of the x-coordinate of $x(\theta_0)$. (Similar figures can be plotted for the ones around L_1 but they will not be shown here.)

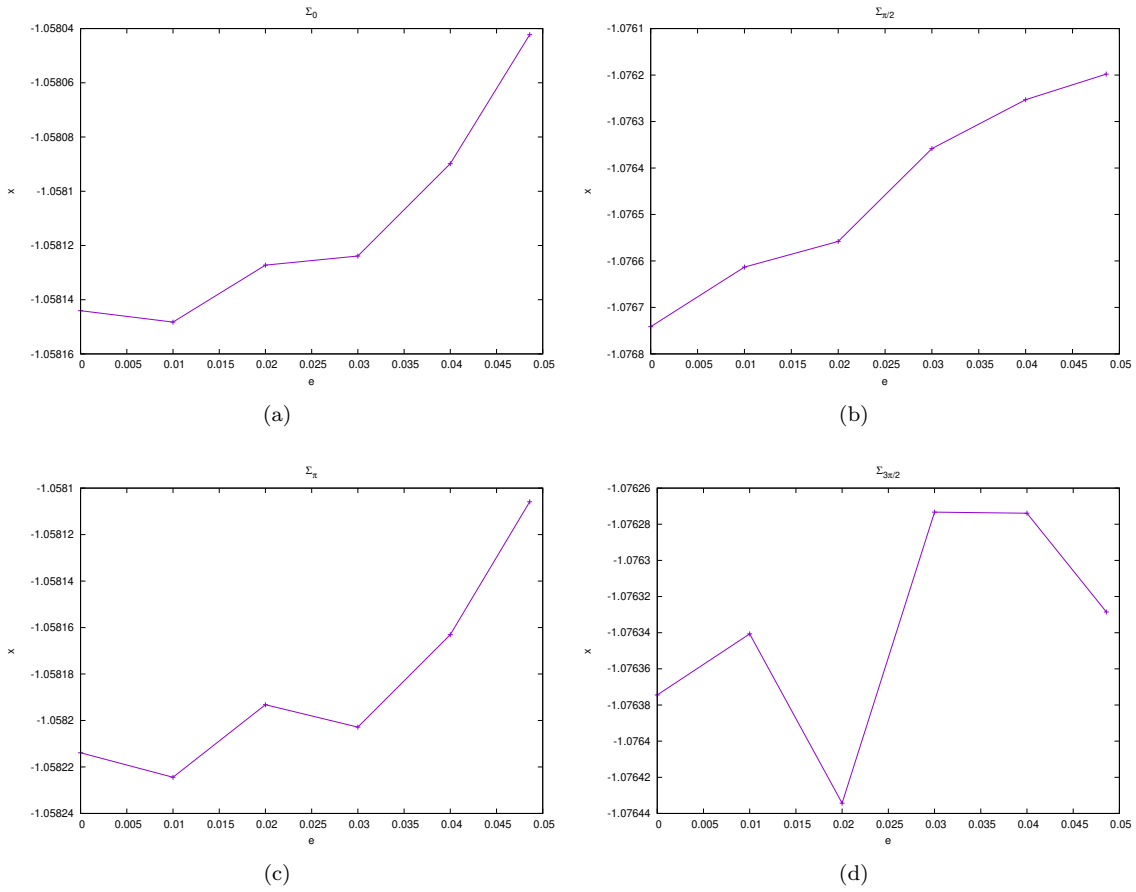

Figure 5.3: Computed x-coordiante of the first point, i.e., $x(\theta_0)$ for each initial periodic orbit until they reach to invariant curve representing the torus for the PERTBP with the Sun-Jupiter eccentricity.

Remark: It was not necessary a small step for the continuation process. Indeed, a step of 10^{-2} has been used succesfully. We just highlight that the first step was small 10^{-8}. We have tried with greater values

and the method would not converge. But after it, the other steps were either 10^{-2} or around it (to reach $e = 0.048594036027482114$ we went from 0.04 to this value in one step, for instance).

Remark: The values of $x(\theta_0)$ presented in Figures 5.3(a) and 5.3(c) are close (the same for the pair of Figures 5.3(b) and 5.3(d)). This is due to the fact that integrating the PCRTBP for time 2π in the periodic orbit related to $H = -1.5175$ means almost two revolutions around L_2, so that the angle related to the first point will be approximately the same for the pairs Σ_0 and Σ_π and $\Sigma_{\frac{\pi}{2}}$ and $\Sigma_{\frac{3\pi}{2}}$.

5.3 Computation of the Stability of a Torus

Let us consider the following system

$$\begin{cases} \overline{x} = A(\theta)x \\ \overline{\theta} = \theta + \omega \end{cases}, \tag{5.14}$$

where $A(\theta) = D_x P(x(\theta))$.

This sytem is called reducible when there exists a change of variables $y = C(\theta)x$ such that the above system can be written as

$$\begin{cases} \overline{y} = By \\ \overline{\theta} = \theta + \omega \end{cases}, \tag{5.15}$$

where $B = C^{-1}(\theta + \omega)A(\theta)C(\theta)$ does not depend on θ.

The dynamics of system (5.15) can be easily studied by computing the eigenvalues of B.

Furthermore, in such case that the system is reducible, the columns of matrix C will be given by the eigenvectors related to the eigenvalues of Equation (5.16).

Let us see this in more detail.

Considering the single shooting situation, we would like to compute pairs $(\lambda, \psi) \in \mathbb{C} \times \mathcal{C}^0(\mathbb{T}^1, \mathbb{C}^n)$ such that

$$A(\theta)\psi(\theta) = \lambda T_\omega \psi(\theta). \tag{5.16}$$

The above equation is equivalent to

$$T_{-\omega} \circ A(\theta)\psi(\theta) = \lambda\psi(\theta).$$

In all its generality this is an infinite-dimensional problem.

In order to solve it, we will use the same strategy as above: approximate these infinite dimensional objects

by means of truncated Fourier series.

Remark: For more details, see [Jor01]. We will present here some of the results that will be seen in the case of parallel shooting without the proofs.

We have that the eigenvalues are organized in, at most, n circles.

In the case of the PERTBP, we have three of them for the region around L_1 and L_2, as their stability is centre $\times$ saddle.

Before moving to the parallel shooting case, let us comment on the discretization of the operators $T_{-\omega}$ and $A(\theta)$.

As $A(\theta) = D_x P(x(\theta))$, we have already seen, in Section 5.1, how to discretize it.

For the operator $T_{-\omega}$, when applied to $\psi(\theta)$ gives us $\psi(\theta - \omega)$. If we have ψ written by means of a truncated Fourier series,

$$\psi(\theta) = a_0 + \sum_{k=1}^{N} a_k \cos k\theta + b_k \sin k\theta,$$

it is clear that applying $T_{-\omega}$ does not mix any coefficient a_k or b_k, it is simply a change in the angle of functions sin and cos.

More specifically, we have that

$$\begin{aligned}
T_{-\omega}(x(\theta)) &= x(\theta - \omega) \\
&= a_0 + \sum_{k=1}^{N} a_k \cos(k(\theta - \omega)) + b_k \sin(k(\theta - \omega)) \\
&= a_0 + \sum_{k=1}^{N} a_k (\cos(k\theta)\cos(k\omega) + \sin(k\theta)\sin(k\omega)) + b_k (\sin(k\theta)\cos(k\omega) - \cos(k\theta)\sin(k\omega)) \\
&= a_0 + \sum_{k=1}^{N} (a_k \cos(k\omega) - b_k \sin(k\omega))\cos(k\theta) + (a_k \sin(k\theta) + b_k \cos(k\omega))\sin(k\theta),
\end{aligned}$$

i.e., we can write

$$\begin{pmatrix} a_k \\ b_k \end{pmatrix} \xmapsto{T_{-\omega}} \begin{pmatrix} a_k \cos(k\omega) - b_k \sin(k\omega) \\ a_k \sin(k\theta) + b_k \cos(k\omega) \end{pmatrix} = \begin{pmatrix} \cos(k\omega) & -\sin(k\omega) \\ \sin(k\omega) & \cos(k\omega) \end{pmatrix} \begin{pmatrix} a_k \\ b_k \end{pmatrix}.$$

With this, it is not difficult to see that we can write the discretized version of $T_{-\omega}$ as

$$\begin{pmatrix}
I & 0 & 0 & 0 & 0 & \cdots & 0 & 0 \\
0 & I\cos(\omega) & -I\sin(\omega) & 0 & 0 & \cdots & 0 & 0 \\
0 & I\sin(\omega) & I\cos(\omega) & 0 & 0 & \cdots & 0 & 0 \\
0 & 0 & 0 & I\cos(2\omega) & -I\sin(2\omega) & \cdots & 0 & 0 \\
0 & 0 & 0 & I\sin(2\omega) & I\cos(2\omega) & \ddots & 0 & 0 \\
\vdots & \vdots & \vdots & \vdots & \ddots & \ddots & \ddots & \vdots \\
0 & 0 & 0 & 0 & 0 & \ddots & I\cos(N\omega) & -I\sin(N\omega) \\
0 & 0 & 0 & 0 & 0 & \cdots & I\sin(N\omega) & I\cos(N\omega)
\end{pmatrix}.$$

It is important to notice that as a result of this eigenvalues and eigenvectors computation, we will have, for the single shooting case, $n(2N+1)$ pairs (λ, ψ), where the eigenvectors will be, themselves, truncated Fourier series, in other words, if we would like to visualize the vectors in the tangent space of the phase space, we should compute the series in the given point, i.e., to see the vector in the place where it corresponds, we should compute, for $x(\theta_j)$, $\psi(\theta_j)$, for some $j \in \{0, \cdots, 2N\}$.

Remark: We refer to [Jor01] for a complete discussion on how to choose the eigenvector related to which eigenvalue to choose. Here, as we will restrict our attention to the special case of considering just the stable and the unstable manifolds of the invariant curve, we will take the eigenvectors related to the pure real and positive eigenvalues of the greatest and of the smallest circles.

Let us proceed to the case of parallel shooting.

Let $A^i(\theta) = D_x P^i(x(\theta))$ for $i = 0, 1, 2, 3$.

In order to compute the eigenvalues and eigenvectors of the system (already in its discretized version), we should solve the following equation: $A^3 \cdot A^2 \cdot A^1 \cdot A^0\, u = \lambda\, T_\omega\, u$, which is equivalent to solve the system:

$$\begin{cases}
A^0 u = \lambda^{\frac{1}{4}} v \\
A^1 v = \lambda^{\frac{1}{4}} w \\
A^2 w = \lambda^{\frac{1}{4}} t \\
B^3 t = \lambda^{\frac{1}{4}} u
\end{cases} \Leftrightarrow \left(\begin{array}{c:c:c:c}
 & & & B^3 \\ \hdashline
A^0 & & & \\ \hdashline
 & A^1 & & \\ \hdashline
 & & A^2 &
\end{array}\right) \begin{pmatrix} u \\ v \\ w \\ t \end{pmatrix} = \lambda^{\frac{1}{4}} \begin{pmatrix} u \\ v \\ w \\ t \end{pmatrix},$$

where $B^3 = T_{-\omega} \cdot A^3$.

In Figure 5.4 it is shown the computed circles of eigenvalues for one torus around each equilibrium point L_1 and L_2.

Remark: It is important to notice that what is plotted are the values of $\sqrt[4]{\lambda}$.

We have already seen how to compute A^i in the previous section.

Remark: In opposition to what happens when computing a parameterization to a torus, when dealing with its eigenvalues and eigenvalues, even for practical reasons, we need to compute the Fourier transformation of the integrated points, as the operator $T_{-\omega}$ acts in the space of coefficients.

As it happens in the case of single shooting, at the end of the computation of the eigenvalues and eigenvectors, we will have $ns(2N+1)$ pairs (λ, ψ), where n is the dimension of the problem and s is the number of sections (in the case of the PERTBP, $n = s = 4$).

These eigenvectors will came out as a truncated Fourier series. To produce Figure 5.5 we have evaluated these series in a mesh of angles to produce vectors over the torus in the direction of the stable and the unstable manifolds.

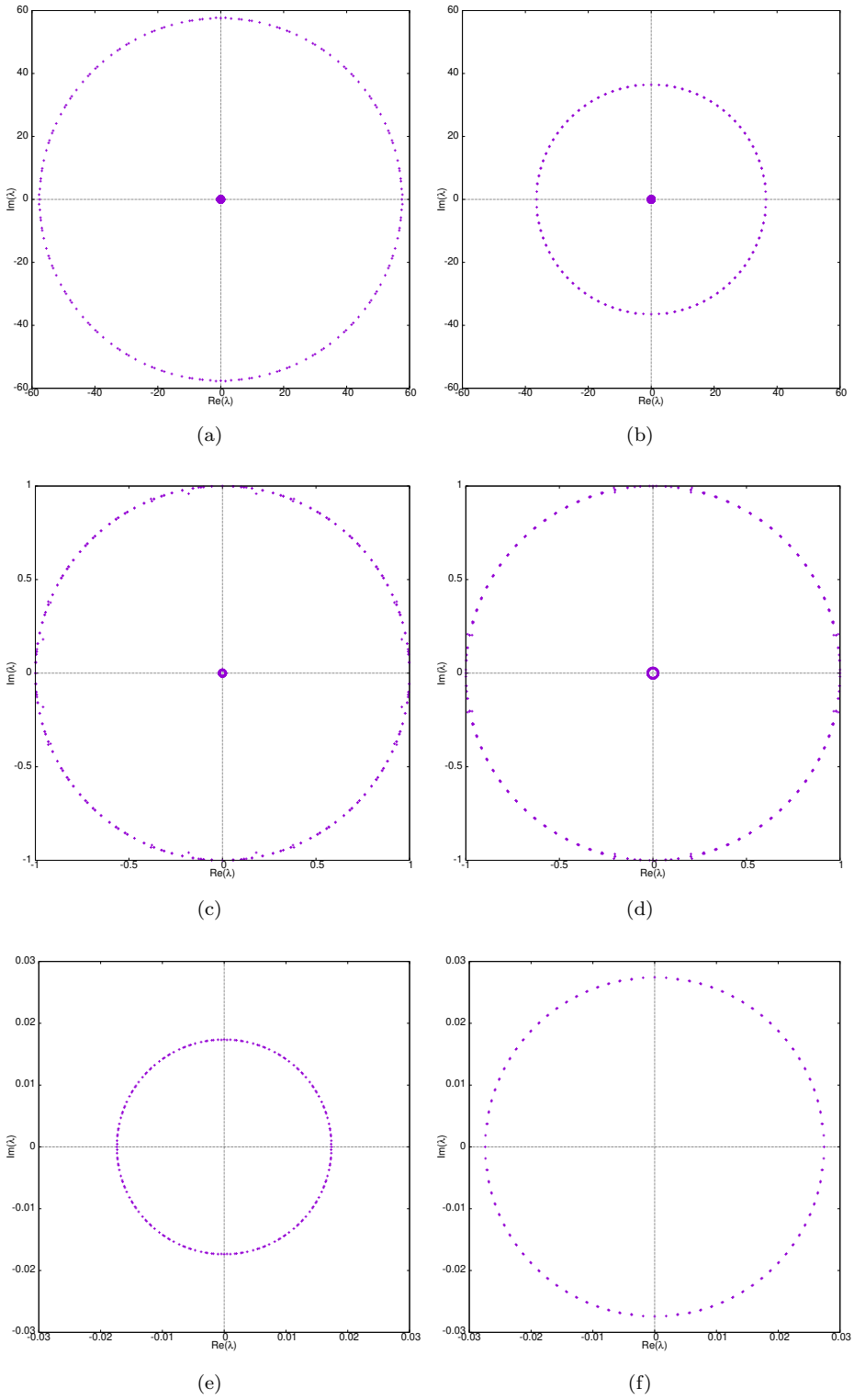

Figure 5.4: Three circles of eigenvalues represented in different scales for magnification. We refer to [Jor01] for the discussion of the accuracy in the computation of these eigenvalues. The ones on the left are related to the torus around L_1 with $\omega = 13.43094470049$ and the ones on the right to the one around L_2 with $\omega = 12.29412293886$.

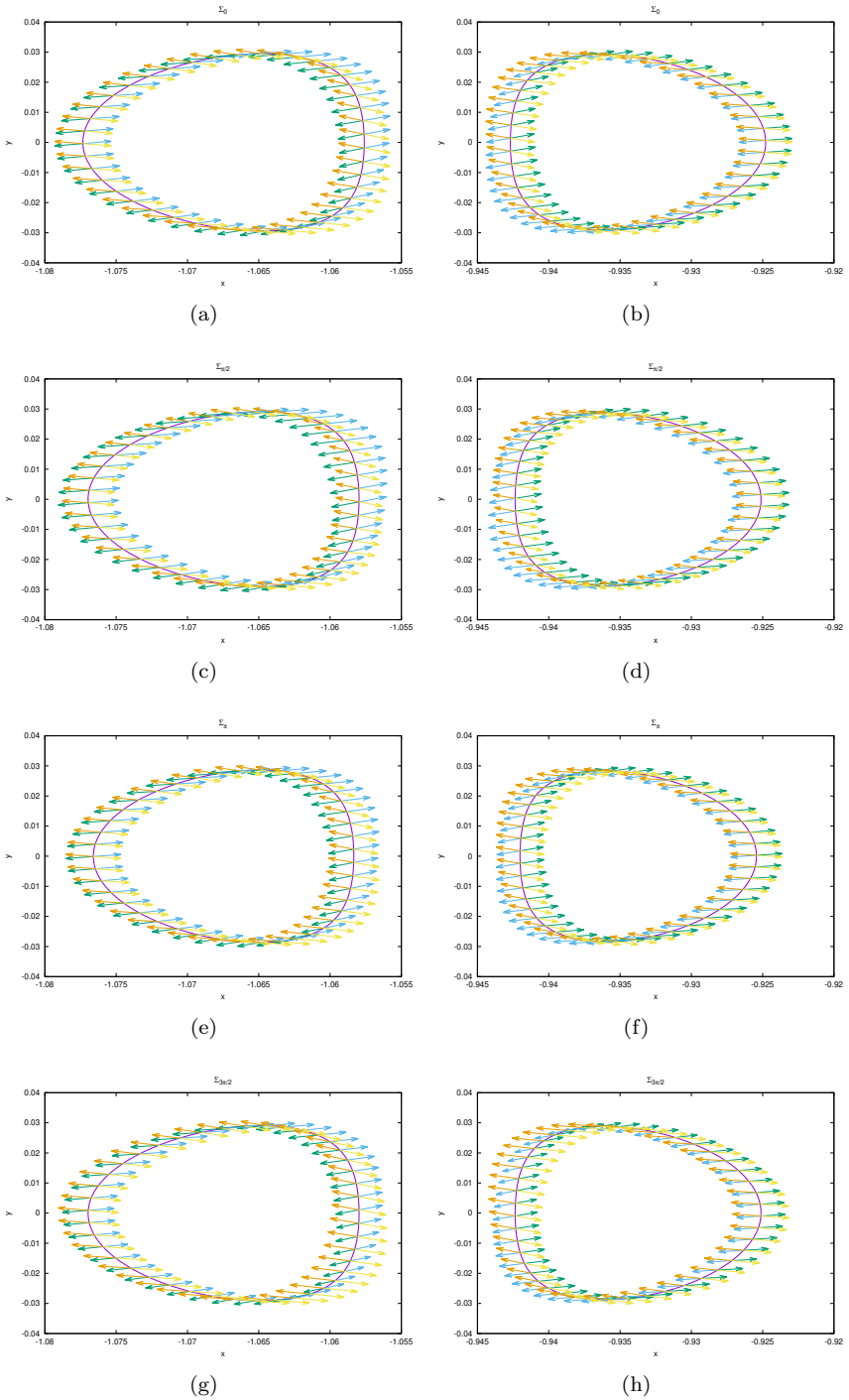

Figure 5.5: Invariant curves around L_1 ((b), (d), (f) and (h)) and L_2 ((a), (c), (e) and (g)) with a mesh of approximations of eigenvectors on each point. Out of scale for better visualization. (a) and (b) are in Σ_0, (c) and (d) are in $\Sigma_{\frac{\pi}{2}}$, (e) and (f) are in Σ_π, (g) and (h) are in $\Sigma_{\frac{3\pi}{2}}$. For the invariant curve around L_1, $\omega = 13.43094470049$ and for the one around L_2, $\omega = 12.29412293886$. In blue and green the eigenvectors related to the smaller eigenvalue (that approximate the stable manifold), and in yellow and orange the ones related to the greater eigenvalue (that approximate the unstable manifold).

5.4 Continuation of a Torus

The idea of conitnuation can be also implemented to compute some tori.

In [GM01] the authors explain how to start this computation from a fixed point of the map (a periodic orbit in the flow).

The main idea is to compute two curves of small radii in the direction of the centre eigenvectors, using, for each one of them, arbitrarily defined small values for their radii, correct them via a Newton's method, so that they are indeed parameterizations and, using them, predict a third one and correct it using a standard Newton's method and so on. It is also possible to use $n > 2$ tori to determine the next one.

In this thesis, we have used $n = 3$, but a different approach, as it was already explained (continuation using e as a parameter).

Remark: We have not used a pseudo-arc length algorithm here because we considered that, as the perturbation parameter was small, for a restricted range of the parameter, the behaviour would be similar to the one found in Figure A.11, i.e., no turning points or bifurcations. It is a possible future direction to investigate this system for greater values of e (for other systems) and so, it would be interesting to implement this strategy.

In the case of the continuation of the computed tori around L_1 and L_2, we have used:

- ω as a continuation parameter;
- a continuation step of $\pm 10^{-4}$;
- a tolerance of 10^{-9}.

Remark: The initial trial were to compute using a tolerance value of 10^{-12}, but for some specific values of ω the convergence were not reached. We strongly believe that the main reason for this is the proximity with a resonance region, but this should be investigated in more details. When setting the tolerance value to 10^{-9}, these tori were computed succesfully and the method were able to move on in the continuation process. A great number of tori could be computed using a more severe tolerance, including the ones we will focus our attention from now on, that were computed using a tolerance value of 10^{-12}, namely, the ones with the greatest rotation number, the ones with the smallest ones and the first computed ones (the ones coming from the periodic orbits in the PCRTBP related to $H = -1.5175$).

Figure 5.6 shows the continuation diagram for the computed tori around L_1 and L_2.

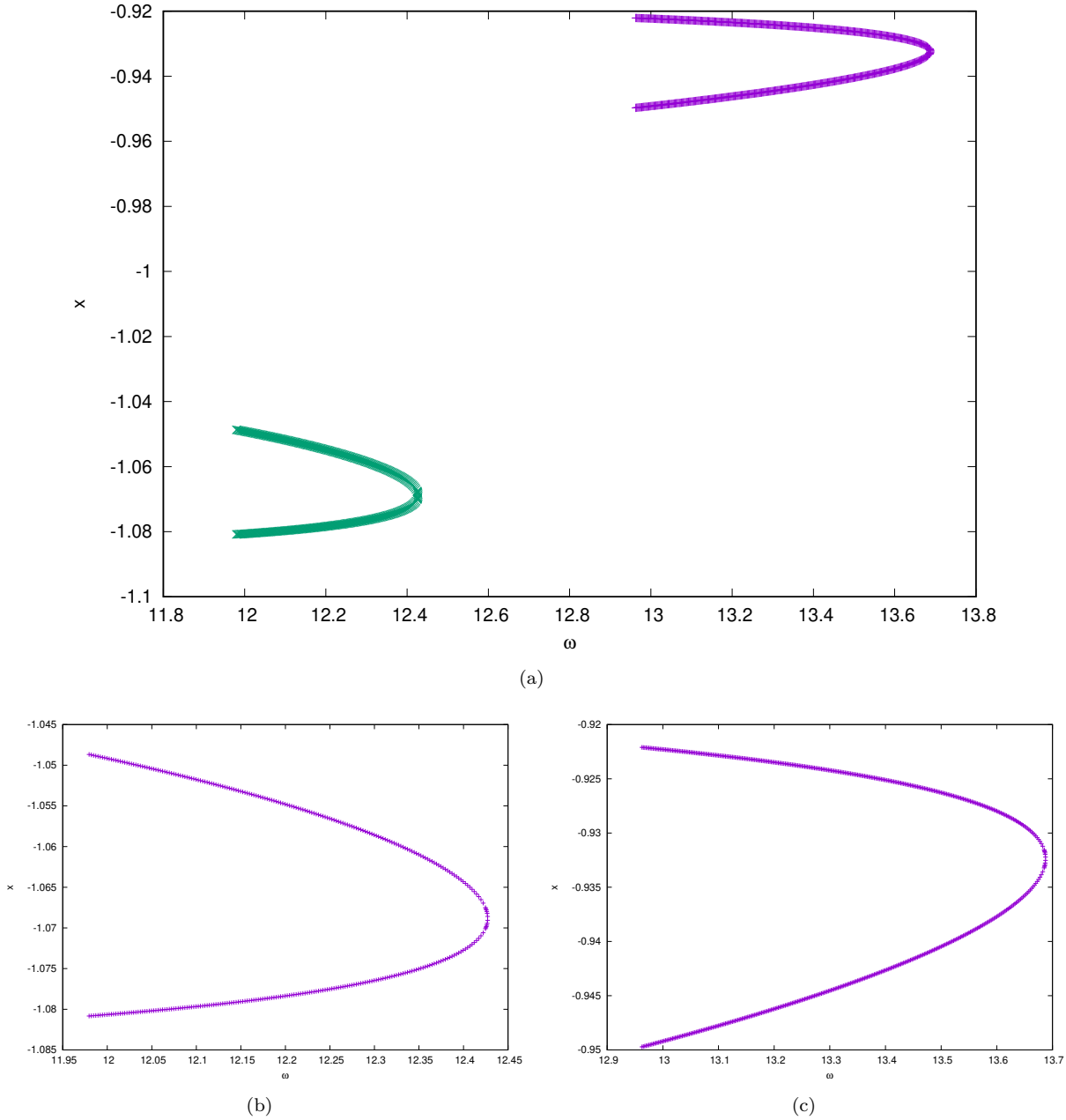

Figure 5.6: Continuation diagram with respect to the rotation number ω as a parameter.

Figure 5.7 shows some of the computed tori around L_1 and L_2.

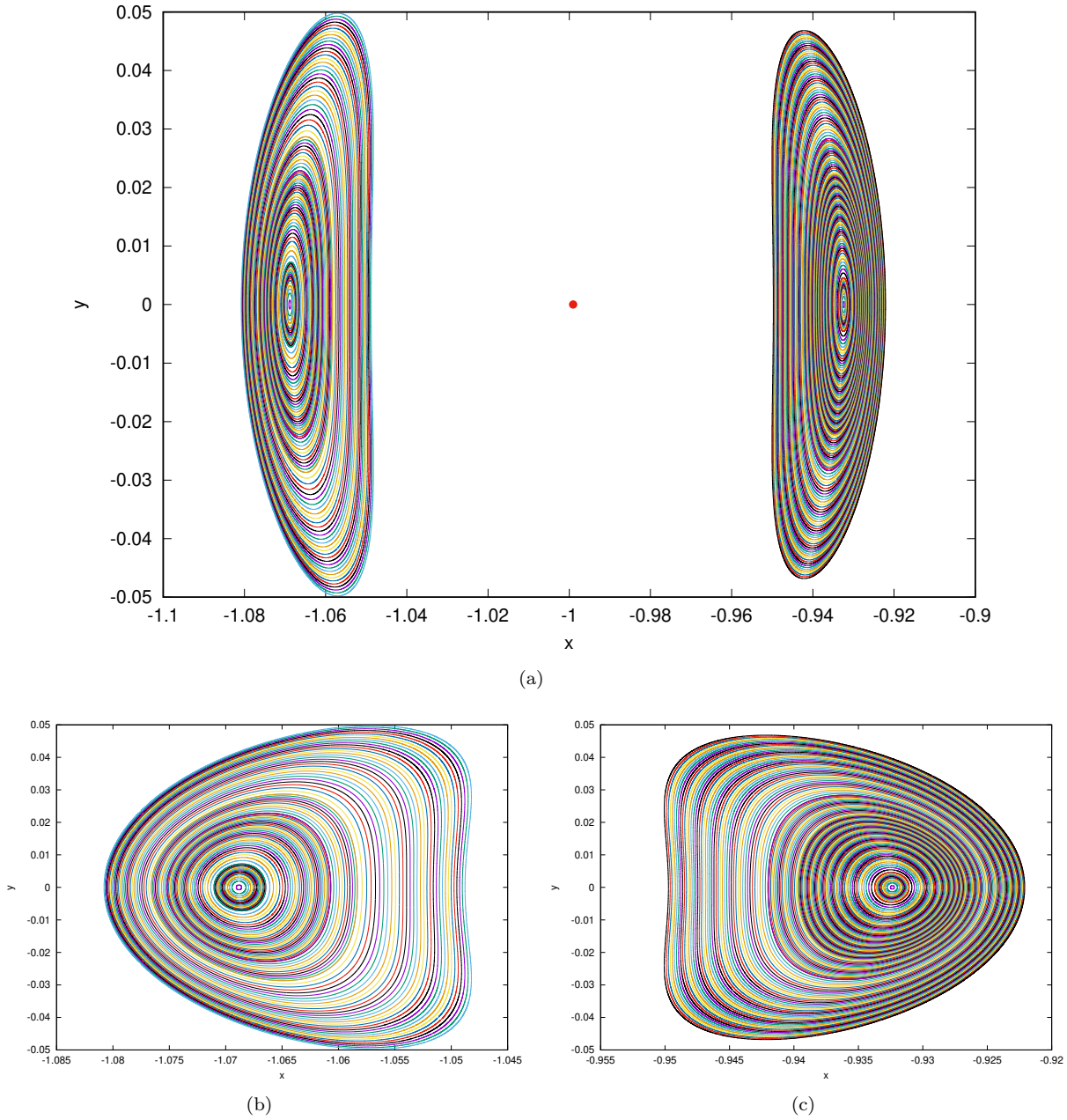

Figure 5.7: Computed tori around L_1 and L_2. In red, Jupiter. See text for details.

With the above specification of the continuation parameter, the continuation step and the tolerance value, we were able to compute:

- 7270 tori for L_1: the ones with $\omega \in [12.96064470049, 13.68754470049]$, N ranging from 20 to 195;

- 4498 tori for L_2: the ones with $\omega \in [11.97742293886, 12.42712293886]$, N ranging from 20 to 140.

Let $T_j^{L_1}$ and $T_k^{L_2}$ be these tori, where $j = -2565, \cdots, 4704$ and $k = -1330, \cdots, 2565$. The sets of indexes is built as it follows: let the tori of indexes $j = 0$ and $k = 0$ be the first computed ones (the ones coming from the periodic orbits in the PCRTBP), the tori with larger rotation number ω will be denoted by negative indexes (they will be smaller) and the ones with smaller rotation number will be assigned the positive indexes.

In Figure 5.7 not every computed tori is shown. We have

- For the ones around L_1:
  - for the ones between $T_{-2565}^{L_1}$ and $T_{-2500}^{L_1}$ every 5;
  - for the ones between $T_{-2500}^{L_1}$ and $T_{-1000}^{L_1}$ every 25;
  - for the ones between $T_{-1000}^{L_1}$ and $T_0^{L_1}$ every 50;
  - for the ones between $T_0^{L_1}$ and $T_{4704}^{L_1}$ every 100;
- For the ones around L_2:
  - for the ones between $T_{-1330}^{L_2}$ and $T_{-1250}^{L_2}$ every 5;
  - for the ones between $T_{-1250}^{L_2}$ and $T_{-500}^{L_2}$ every 25;
  - for the ones between $T_{-500}^{L_2}$ and $T_0^{L_2}$ every 50;
  - for the ones between $T_0^{L_2}$ and $T_{3167}^{L_2}$ every 100;

Compare Figures A.11(a) and 5.6(a).

It is true that they are not exactly the same, but they somehow resemble each other.

Notice that we have shown two different parameters for the continuation in the circular and in the elliptic cases: in the former one, we have chosen the Hamiltonian value while, in the latter one, the rotation number.

It should also be mentioned is that, it is computationally expensive to compute these tori beyond the ones that are presented so, as these tori are enough for the main application of this research - to be presented in Chapter 6 - we have decided to stop the computation. We will discuss, in the next chapter, the reason why the values where the computations were stopped are good stopping values, in the case of modelling the dynamics of Oterma.

Compare also Figures A.10(a) and 5.7(a).

These figures also resemble each other. More specifically, we can foresee that, letting the continuation of tori go further, will produce a set of tori that, if plotted, mimic the periodic orbits.

It should be mentioned that everything we are stating here are to be understood as the case for the eccentricity e of the Sun-Jupiter system, which is a small perturbation parameter. For greater values of e, these features should be investigated.

5.5 Computation of the Stable and Unstable Manifolds of a Torus

Analogously to the case of a periodic orbit, when computing the stable and unstable manifolds of a torus, we will used, as an initial approximation, the eigenvectors associated to the real eigenvalues largest (unstable) and smallest (stable) than 1.

Given a computed torus ($x(\theta)$) with its eigenvalues (λ) and associated eigenvectors ($\psi(\theta)$) we are able to produce an initial approximation for the stable and the unstable manifolds in a slightly different way than the one done for the case of a periodic orbit.

Let $m \in \mathbb{N}$.

Let us denote λ^α and $\psi^\alpha(\theta)$ ($\alpha = s, u$) the real, positive, largest ($\alpha = u$) and smallest ($\alpha = s$) eigenvalues and its associated eigenvectors.

Let us focus in the case of the computation of the unstable manifold, as the stable one is similar.

Compute

$$x(\theta_j) + h\psi^u(\theta_j), \tag{5.17}$$

for $j = 0, \cdots, m-1$ - typically $m = 2N + 1$, though it is not necessary - and for h small enough.

This will be a curve that was shifted (by a small quantity) in the direction of the unstable manifold.

It is important to notice that it does not belong to the manifold, but it is near it. Moreover, the smaller the value of h, the closer to the manifold it is. More specifically, the distance from the manfold is of the order $O(h^2)$. We have chosen, for the computations presented in this section, $h = 10^{-5}$.

As it is near the unstable manifold, if we apply the mapping on it, this curve will land in another one also near the unstable manifold.

If we proceed in this application of the mapping in the curves, eventually the initial approximation will not be enough, but for a finite number of them, it is reasonable to consider all of them as close to the manifold.

In other words, applying the mapping a modest number of times on the initial curve (5.17), will produce

a sequence of curves close to the unstable manifold, that serve as a way of visualizing it.

We refer to Section 4.2.1 and Figure 8 of [Jor01] for an example of this.

In the above-mentioned section, the author comment on the usage of a fundamental domain for a better visualization.

The idea of fundamental domain were already explained in Section A.5.1.

We will only point out here the difference that, when using the concept of fundamental domain in this context, we will interpolate, instead of points, curves, so we will end up with a number of curves that we should apply the dynamics on each of them to produce another set of curves, that will lie close to the unstable manifold, and apply again the dynamics and so forth, a reasonable number of times.

Differently from what is was explained in Section A.5.1 (and illustrated in Figure A.13), here we will not use a point and its iterate to interpolate between, but instead an approximation of it.

As

$$\begin{aligned} P(x(\theta)+h\psi^u(\theta)) &= P(x(\theta))+hD_xP(x(\theta))\psi^u(\theta)+\mathcal{O}(h^2) \\ &= x(\theta+\omega)+h\lambda\psi^u(\theta+\omega)+\mathcal{O}(h^2). \end{aligned} \tag{5.18}$$

we will approximate $P(x(\theta-\omega)+h\psi^u(\theta-\omega))$ by its linear part, i.e.,

$$P(x(\theta-\omega)+h\psi^u(\theta-\omega)) \approx x(\theta)+h\lambda\psi^u(\theta).$$

So, the interpolation will be done between the curves $x(\theta_j)+h\psi^u(\theta_j)$ and $x(\theta_j)+h\lambda\psi^u(\theta_j)$, $j=0,\cdots,m-1$.

Remark: It is also possible to interpolate between $x(\theta_j)+h\psi^u(\theta_j)$ and $P(x(\theta-\omega)+h\psi^u(\theta-\omega))$, but, computationally, it is easier and faster to approximate the second one by its linear part.

Remark: Notice that the curves $x(\theta_j)+h\lambda\psi^u(\theta_j)$ and $P(x(\theta-\omega)+h\psi^u(\theta-\omega))$, $j=0,\cdots,m-1$ are approximately the same shiftted by an angle of ω.

Let us see now how the ideas of fundamental domain and parallel shooting can be mixed so that we are able to produce a satisfactory visualization of the invariant stable/unstable manifolds in the case of a highly-unstable environment.

In the case of using parallel shooting, Equation (5.18) turns out to be written as

$$\begin{aligned}
P^0(x_0(\theta)+h\psi_0(\theta)) &= P^0(x_0(\theta))+hD_xP^0(x_0(\theta))\psi_0(\theta)+\mathcal{O}(h^2)\\
&= x_1(\theta)+h\sqrt[4]{\lambda}\psi_1(\theta)+\mathcal{O}(h^2)\\
P^1(x_1(\theta)+h\psi_1(\theta)) &= P^1(x_1(\theta))+hD_xP^1(x_1(\theta))\psi_1(\theta)+\mathcal{O}(h^2)\\
&= x_2(\theta)+h\sqrt[4]{\lambda}\psi_2(\theta)+\mathcal{O}(h^2)\\
P^2(x_2(\theta)+h\psi_2(\theta)) &= P^2(x_2(\theta))+hD_xP^2(x_2(\theta))\psi_2(\theta)+\mathcal{O}(h^2)\\
&= x_3(\theta)+h\sqrt[4]{\lambda}\psi_3(\theta)+\mathcal{O}(h^2)\\
P^3(x_3(\theta)+h\psi_3(\theta)) &= P^3(x_3(\theta))+hD_xP^3(x_3(\theta))\psi_3(\theta)+\mathcal{O}(h^2)\\
&= x_0(\theta+\omega)+h\sqrt[4]{\lambda}\psi_0(\theta+\omega)+\mathcal{O}(h^2).
\end{aligned} \tag{5.19}$$

Notice that the last equation can be written as

$$\begin{aligned}
P^3(x_3(\theta-\omega)+h\psi_3(\theta-\omega)) &= P^3(x_3(\theta-\omega))+hD_xP^3(x_3(\theta-\omega))\psi_3(\theta-\omega)+\mathcal{O}(h^2)\\
&= x_0(\theta)+h\sqrt[4]{\lambda}\psi_0(\theta)+\mathcal{O}(h^2).
\end{aligned}$$

In Figure 5.8 the points represent the tori (which are invariant curves, as we are intersecting them with a transversal plane) and the curves represent its manifolds. The bigger numbers, from 0 to 3, denote the curves and the smaller ones, from 1 to 10, the points on them. For the points, we have

- 1: $x_j(\theta)$;
- 2: $x_j(\theta)+h\psi_j(\theta)$;
- 3: $x_j(\theta)+h\sqrt[4]{\lambda}\psi_j(\theta)\approx P^k(x_{j-1}(\theta)+h\psi_{j-1}(\theta))$;
- 4: $P^k(x_j(\theta)+h\sqrt[4]{\lambda}\psi_j(\theta))$;
- 5: $P^l(P^k(x_j(\theta)+h\sqrt[4]{\lambda}\psi_j(\theta)))$;
- 6: $P^m(P^l(P^k(x_j(\theta)+h\sqrt[4]{\lambda}\psi_j(\theta))))$,
- and so forth,

for $j,k,l,m=0,1,2,3$ and $k,l,m\neq j$.

The part between points 2 and 3 is a straight line close to the invariant manifold, and each of these small parts will be integrated to compute the region between points 3 and 7.

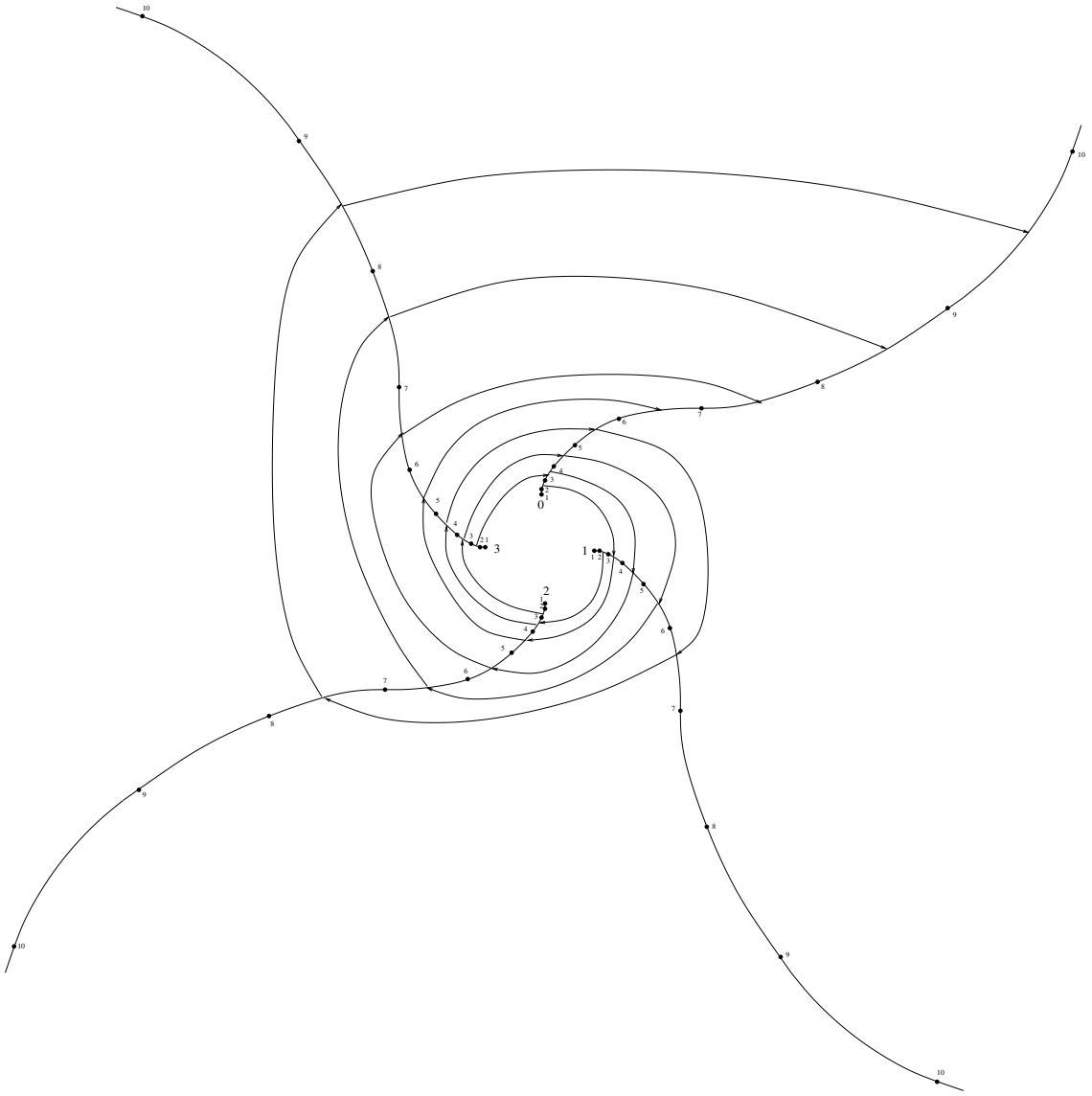

Figure 5.8: Illustration on how the parallel shooting technique can be used together with the fundamental domain concept in order to have a more precise computation of the invariant manifolds of a torus. See the text for details.

If, instead of parallel shooting, we were using single shooting, the part between points 2 and 6 would be a straight line, i.e., all this region of the manifold would approximated by a straight line, and the region between 6 and 10 would be the image of it, which would be a worst approximation than the one presented here.

The number of intermediate curves were set to 10 between each pair of points 2 and 3 and $h = 10^{-5}$.

Let us now present a number of figures showing slices of the stable and unstable manifolds for some tori around L_1 and L_2.

All the figures that will be presented here lie in Σ_π.

Except when specified the opposite, in every set of 4 figures:

- the subfigure (a) will be composed by the curves coming from $\Sigma_{\frac{3\pi}{2}}$ for the stable manifold and from $\Sigma_{\frac{\pi}{2}}$ for the unstable one;
- the subfigure (b) will be composed, in addition to the previous ones, by the curves coming from Σ_0 for both the stable and the unstable manifolds;
- the subfigure (c) will be composed, in addition to the previous ones, by the curves coming from $\Sigma_{\frac{\pi}{2}}$ for the stable manifold and from $\Sigma_{\frac{3\pi}{2}}$ for the unstable one;
- finally, the subfigure (d) will be composed, in addition to the previous ones, by the curves coming from Σ_π for both the stable and the unstable manifolds.

They will be presented in pairs:

- $T_0^{L_1}$ and $T_0^{L_2}$, as they are the ones that result from the continuation wth respect to e from the orbits in the PCRTBP around the equilibrium points related to $H = -1.5175$;
- $T_{-2565}^{L_1}$ and $T_{-1330}^{L_2}$, as they are the largest ones.
- $T_{4704}^{L_1}$ and $T_{3167}^{L_2}$, as they are the ones with the smallest computed distance to the equilibrium points;

Remark: It is not mandatory to presented them in pairs, and, if so, it is not true that they are related one-to-one, as it was the case in the PCRTBP. In other words, $T_0^{L_1}$ for instance, may have some influence in (and/or be influenced by) $T_0^{L_2}$, but not only this one, as other ones with closer values of ω.

In all the following tori, the stable and unstable manifolds are as the following illustration:

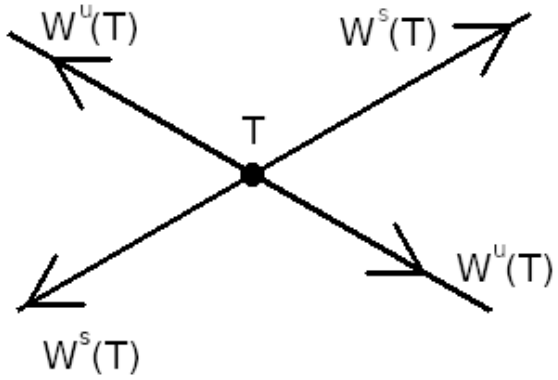

Figure 5.9: Illustration on how the directions of the stable and the unstable tori in what follows.

The following figures refer to the following pairs of tori:

- Figures 5.10, 5.11, 5.12 and 5.13 refer to $T^{L_1}_{-2565}$ and $T^{L_2}_{-1330}$;
- Figures 5.14, 5.15, and 5.16 refer to $T^{L_1}_0$ and $T^{L_2}_0$;
- Figure 5.17 refers to $T^{L_1}_{4704}$ and $T^{L_2}_{3167}$;

In Figure 5.10 we can see how the stable and the unstable manifolds of the considered tori expand in all directions, while in Figure 5.11 we consider only the expansion in the direction of Jupiter. The construction of the latter in a more step-by-step way in shown in Figures 5.12 and 5.13.

In Figure 5.14 it is shown just the stable manifold of $T^{L_2}_0$ and the unstable one of $T^{L_1}_0$ in the direction of Jupiter, it is almost the same case as Figure 5.11, but instead of showing both the stable and the unstable parts, we have chosen just one for each to be displayed. Notice the difference in scale between these two figures. It may seem, at first sight, that these parts of the manifolds running out of the region which is close to Jupiter escape for no reason, but actually, they follow the parts of the manifolds which goes in the opposite direction. These parts are shown in Figure 5.15 and a slice of the escaping manifolds around each tori, together with the manifolds going outside is shown in Figure 5.16.

Finally, Figure 5.17 shows that the above-described phenomena also happens for the tori $T^{L_1}_{4704}$ and $T^{L_2}_{3167}$.

In the next chapter we will see how to use these manifolds to explain the movement of Oterma when seen in the PERTBP. We will be using some sections in these manifolds and looking for the dynamical objects which interact with Oterma, and make it possible for it to transition between different regions in the phase space.

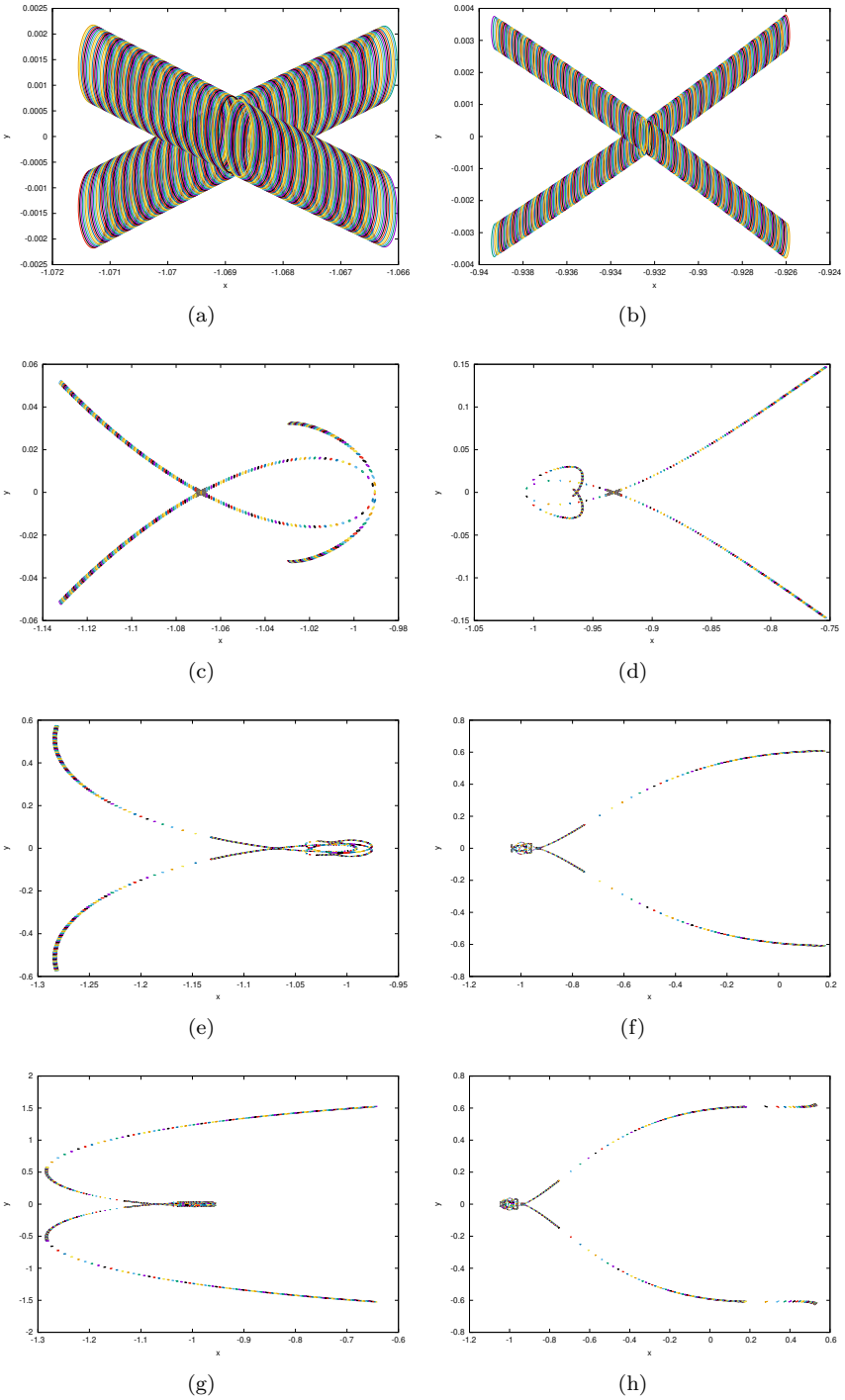

Figure 5.10: Manifolds of the tori $T^{L_2}_{-1330}$ (left column) and $T^{L_1}_{-2565}$ (right column).

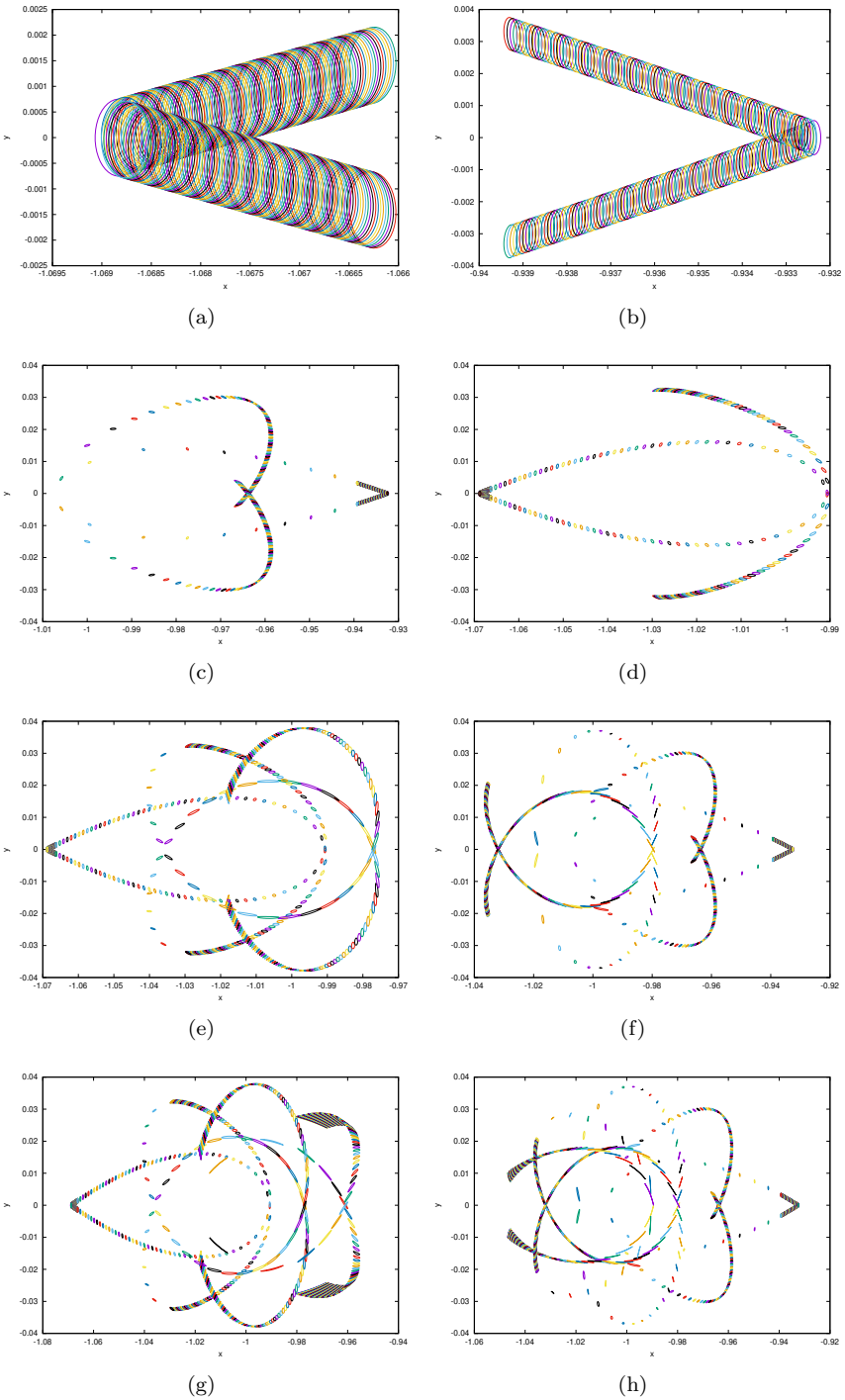

Figure 5.11: Zoom in Figure 5.10 in the region around Jupiter.

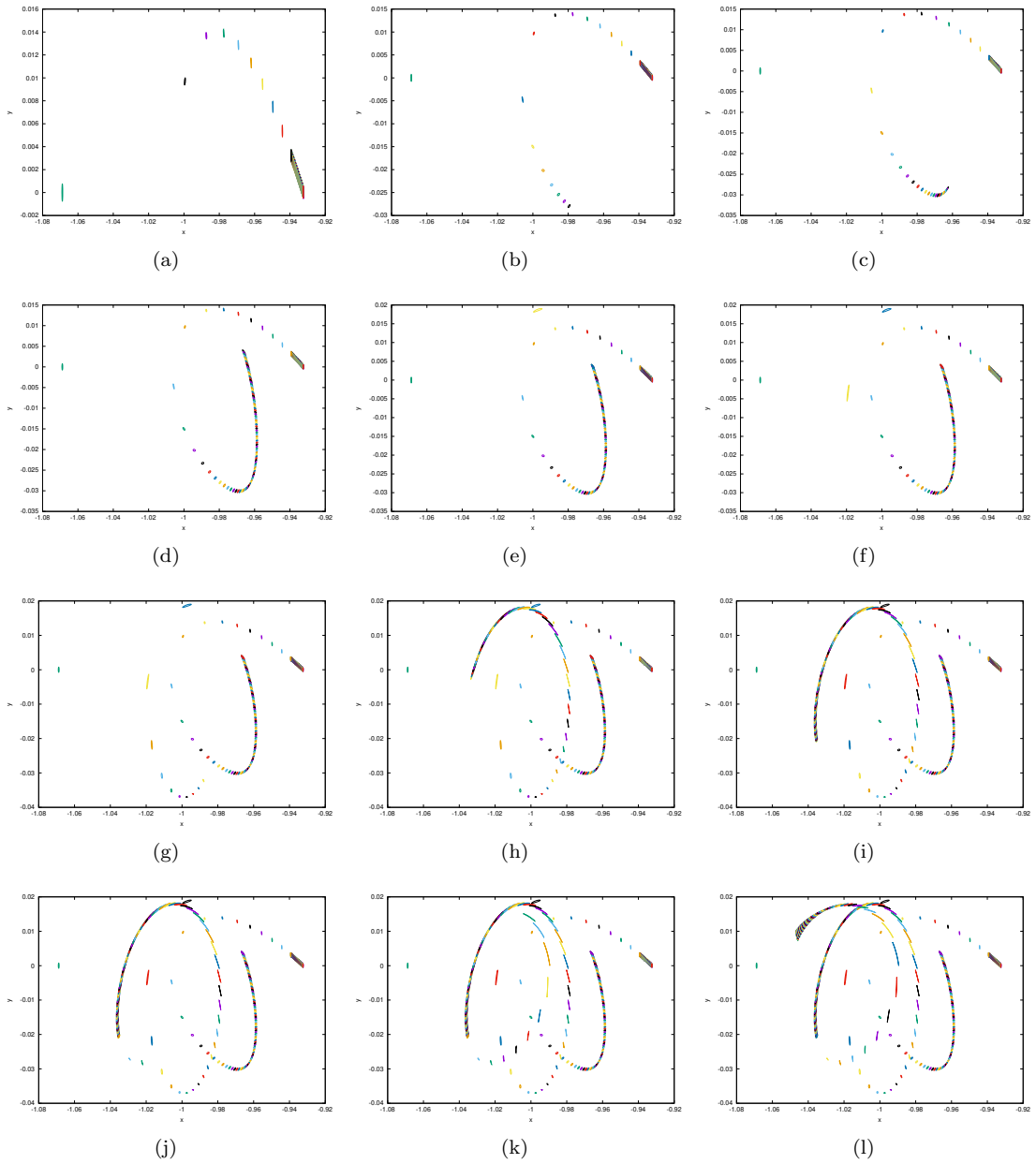

Figure 5.12: Construction step-by-step of a slice of the unstable manifold of the torus $T^{L_1}_{-2565}$ by adding the curves which form the fundamental domain.

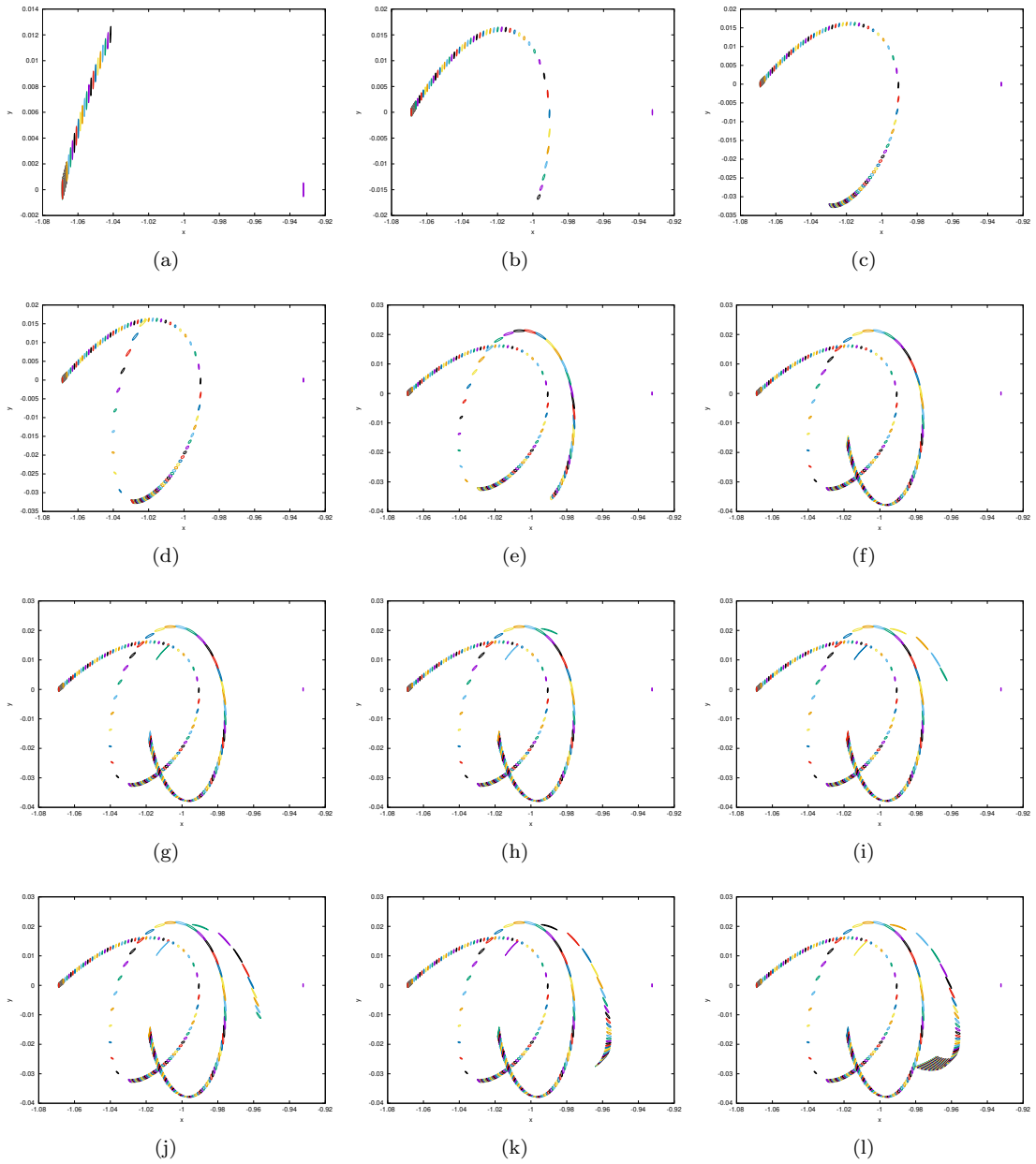

Figure 5.13: Construction step-by-step of a slice of the stable manifold of the torus $T^{L_2}_{-1330}$ by adding the curves which form the fundamental domain.

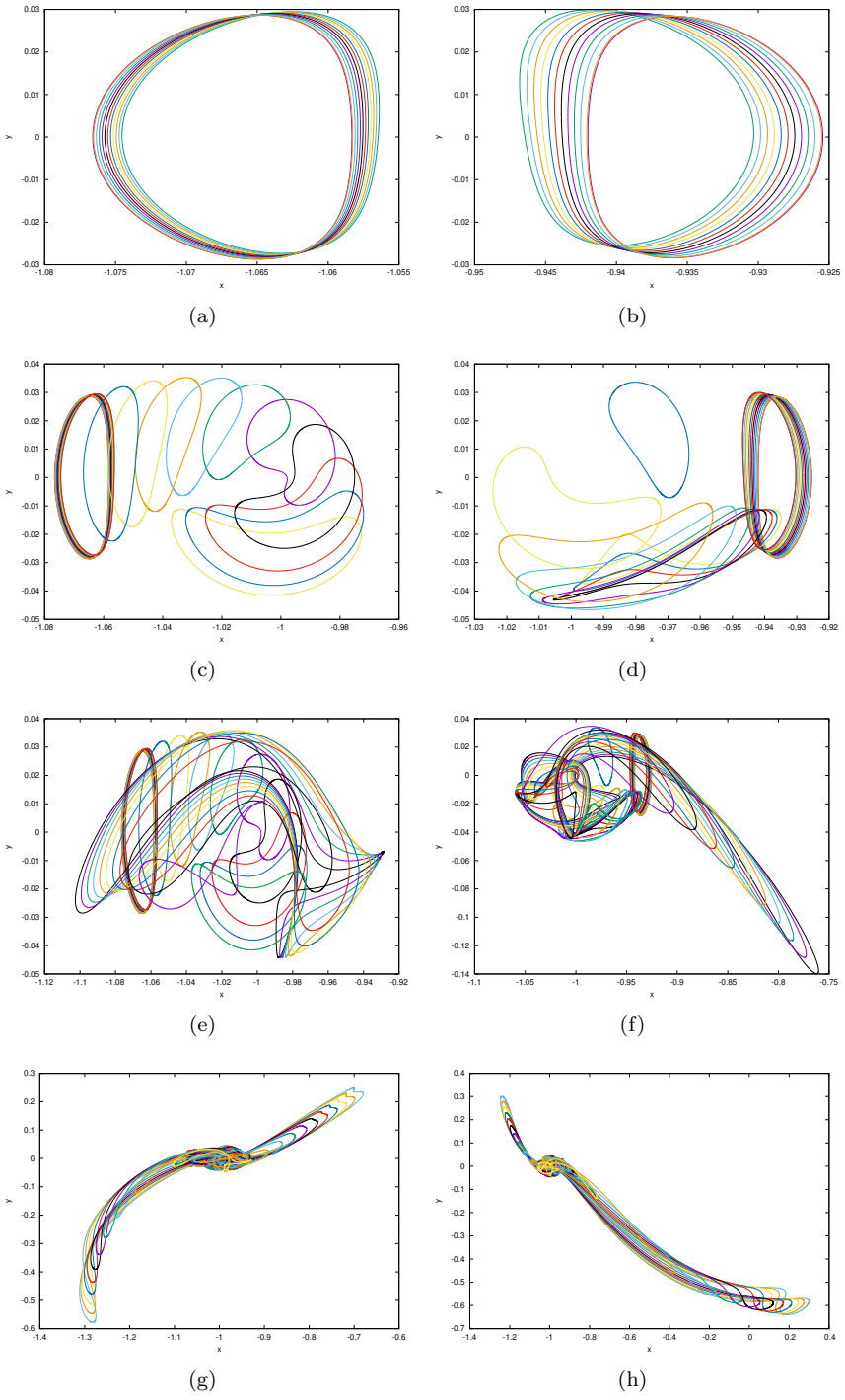

Figure 5.14: Slices of the stable manifold of $T_0^{L_2}$ (left column) and the unstable one of $T_0^{L_1}$ (right column) in the direction of Jupiter.

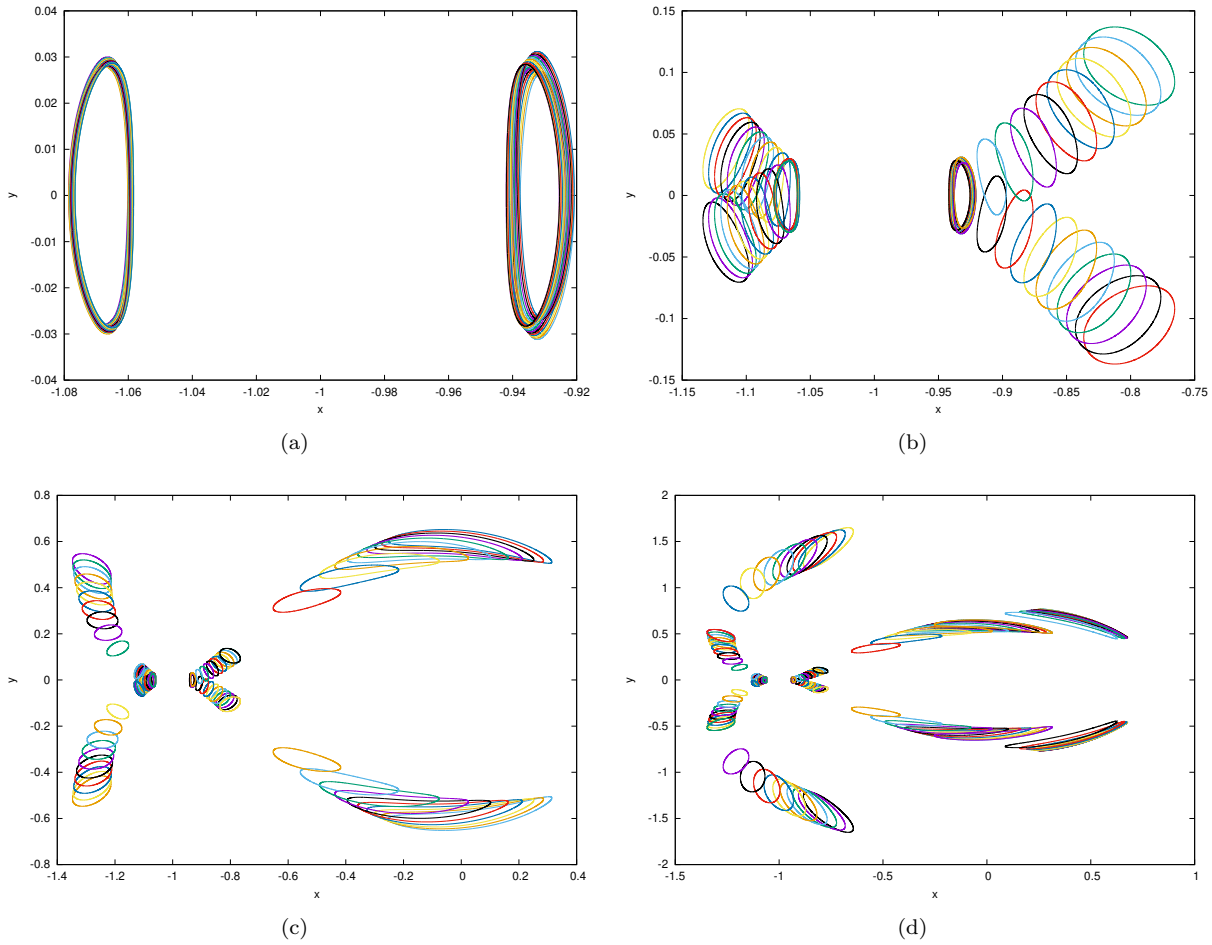

Figure 5.15: Slices of the manifolds of the tori $T_0^{L_1}$ and $T_0^{L_2}$ in the opposite-to-Jupiter direction.

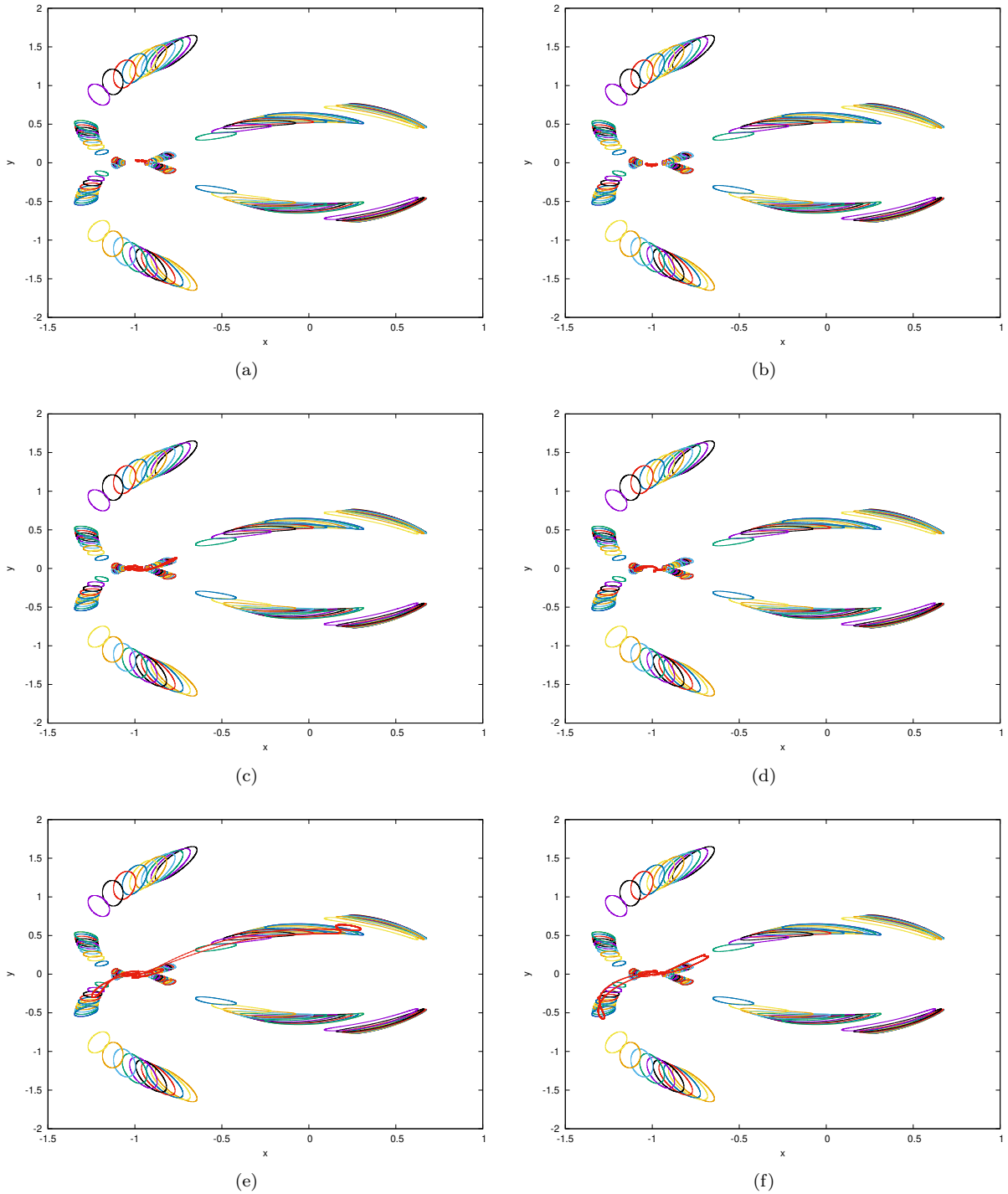

Figure 5.16: Slices of the manifolds represented in Figure 5.15 (opposite-to-Jupiter direction) together with some slices in the direction of Jupiter (in red with interpolated points). On the left side, slices of the stable manifold of $T_0^{L_1}$ and, on the right side, the stable manifold of $T_0^{L_2}$.

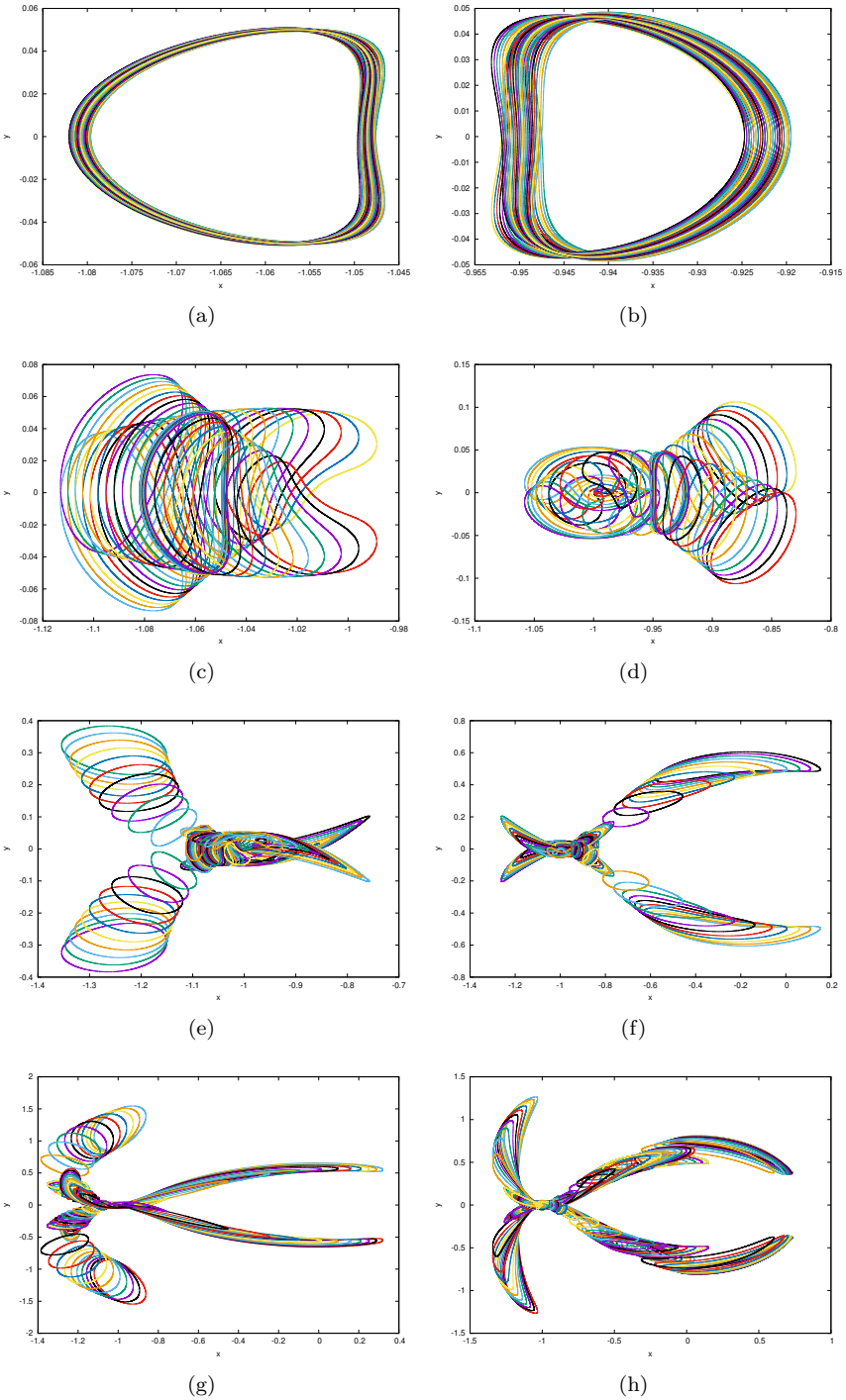

Figure 5.17: Manifolds of the tori $T^{L_2}_{3167}$ (left column) and $T^{L_1}_{4704}$ (right column).

Chapter 6

Oterma in the Planar Elliptic Restricted Three-Body Problem

In this chapter we present the main application and also the main motivation for this thesis: the computation of the dynamical objects possibly responsable for Oterma's dynamics, when fitting its real data in the Planar Elliptic Restricted Three-Body Problem.

Recall that, in Chapters 1 and 2, we saw that, when getting Oterma's data for its position and velocity, applying a change of coordinates to set them in the PCRTBP and integrating them using Equations (1.6), we have, as shown in Figure 2.2, that it does not reproduce its behaviour qualitatively, but, instead of integrating the initial data we have from the change of variables, we modify it slightly, we get, as shown in Figure 2.3, a more feasible reproduction of its dynamics, although this change is arbitrary and it was computed by an trial-and-error approach.

On the other hand, when getting Oterma's data, changing them to fit in the PERTBP and integrating them, using Equations (1.7), we get, as shown in Figures 2.4 and 2.5 a more appropriate reproduction of its dynamics, even though it is not completely accurate, specially due to the revolution it makes around Jupiter when transitioning to the exterior region.

This effect is related to the fact that Oterma's orbit is not inside the same plane that Sun and Jupiter described their movement, the SERTBP is a more natural environment to study this problem, although we believe that the improvement of being able to reproduce partially its dynamics systematically, and not by an arbitrary adjustment, is a considerable improvement.

We will now move on to the visualization, computation and analysis of the dynamical objects that are the

responsible for Oterma's transition, which are, as in the case of the PCRTBP, the heteroclinic connections of invariant manifolds of the tori (periodic orbits in the circular case) around L_1 and L_2.

One important thing to notice here is the difference between the two scenarios:

- In the PCRTBP, once a value for the Hamiltonian is chosen, the orbit gets confined in a three-dimensional submanifold. The periodic orbit around L_1 and the one around L_2 corresponding to this value of the Hamiltonian have dimension 1 and their stable and unstable manifolds have dimension 2. This implies that these manifolds divide the region of possible motion into two.

- In the PERTBP, the Hamiltonian is not constant anymore, so the whole five-dimensional phase space needs to be considered. The tori around L_1 and L_2 have dimension 2 and their stable and unstable manifolds have dimension 3. As the codimension, in this case, is 2, it is not true that these manifolds divide the region of possible motion in two.

This implies that what is described in Section 3.7 of [KLM+01] about the stable and unstable manifolds of the periodic orbits being the separatrices between different types of orbit (transit and nontransit) is not true in the PERTBP, as it is not possible to define what is the inside and the outside of the manifolds, however, for a finite time, it is reasonable to hope for a similar behaviour.

Still concerning the dimensions of this problem of visualization and categorization of these objects: again, we have a five-dimensional phase space in which the dynamics occur, and no reduction to a submanifold is known to be valid. So, if we would like to use the same tools as in the previous case, we should proceed with caution. It is not an easy task to represent higher-dimensional objects.

Take a torus around L_1 and one around L_2. We start by slicing them with the temporal sections $\Sigma_{\frac{i\pi}{2}}$, $i = 0, 1, 2, 3$, as they were the ones used in Chapter 5 to compute the invariant tori.

Figure 6.1 shows these intersections together with projected Oterma's position in these same sections.

Remark:The initial data for Oterma has been selected when the comet is close to L_2 (see Chapter 3). For this initial data, $f = 3.8817002439241626$. So, the positions plotted in Figure 6.1 were computed via forward integration for $\Sigma_{\frac{3\pi}{2}}$ and backward for the others.

It would be interesting to choose one of the sections $\Sigma_{\frac{i\pi}{2}}$ to visualize the computations, for instance, the stable and unstable manifolds of the tori. It would also be interesting to choose some tori to compute these manifolds as it is computationally expensive to compute them for each computed torus, and the amount of data would be enormous.

From Figure 6.1 we may see that the section Σ_π is the best one to be chosen, since it is the closest one before the first transition to happen (in $\Sigma_{\frac{3\pi}{2}}$, Oterma is already between L_1 and L_2).

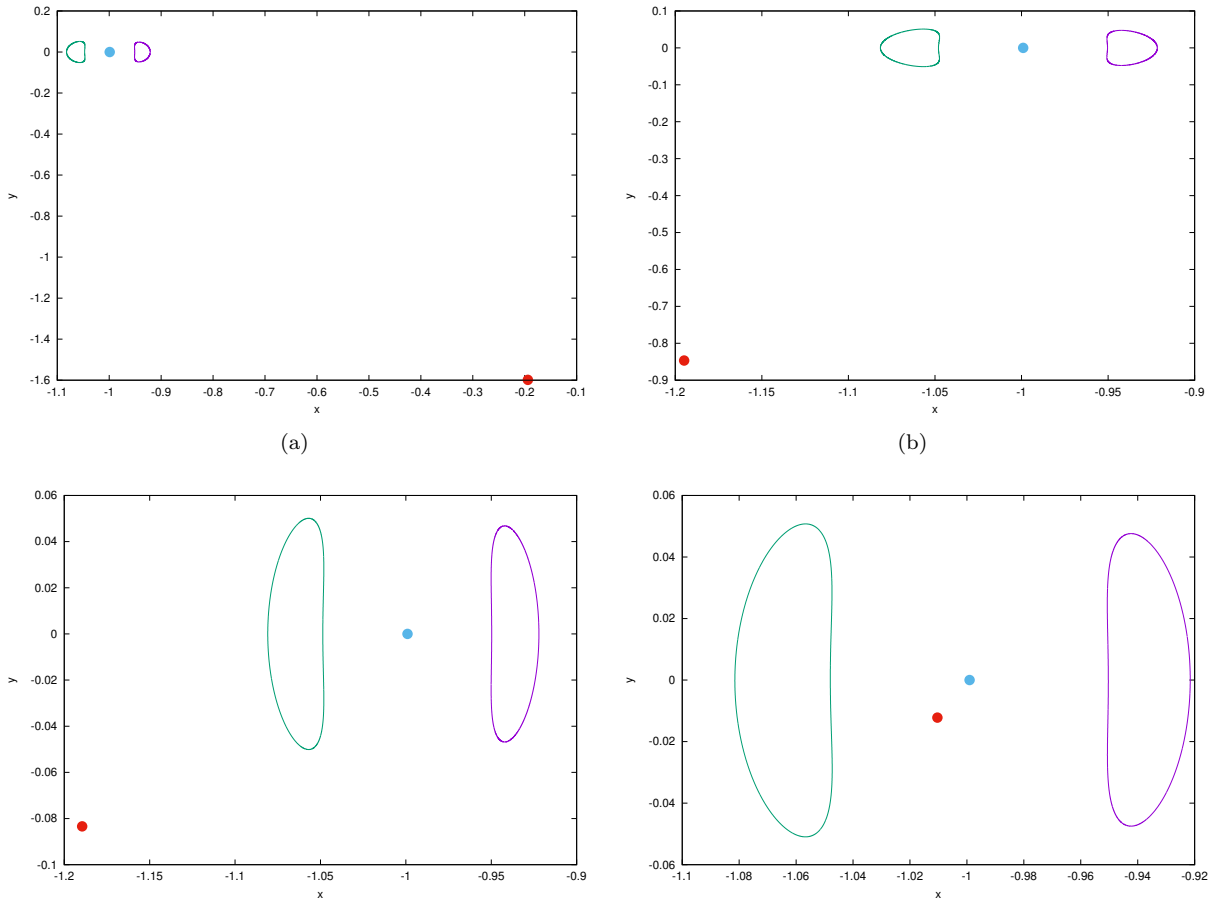

Figure 6.1: $T^{L_1}_{-2565}$ and $T^{L_2}_{-1330}$ together with Oterma, in red, and Jupiter, in blue, in (a) Σ_0, (b) $\Sigma_{\frac{\pi}{2}}$, (c) Σ_π, (d) $\Sigma_{\frac{3\pi}{2}}$.

Notice that Σ_π is a four-dimensional environment. It is still not obvious how to visualize the manifolds and their infuence over Oterma, as it may be seen, for instance, in Figure 6.2, that shows some slices of the stable manifold of some tori around L_2 together with Oterma, in the configuration space.

Let us proceed in the search for the dimension decreasing.

In opposition to the situation in the circular case, where we have a continuous flow in the phase space, here in the PERTBP, we have defined a discrete mapping $P^i : \Sigma_{\frac{i\pi}{2}} \longrightarrow \Sigma_{\frac{(i+1)\pi}{2}}$, which means that Oterma's orbit would be given as a set of discrete points in the temporal sections $\Sigma_{\frac{i\pi}{2}}$, instead of a 1-dimensional curve. So we should be careful when choosing a section to reduce the dimension, as Oterma may not belong to it.

Inside the sections $\Sigma_{\frac{i\pi}{2}}$ the tori have dimension 1 and their manifolds are 2-dimensional, so if we cut

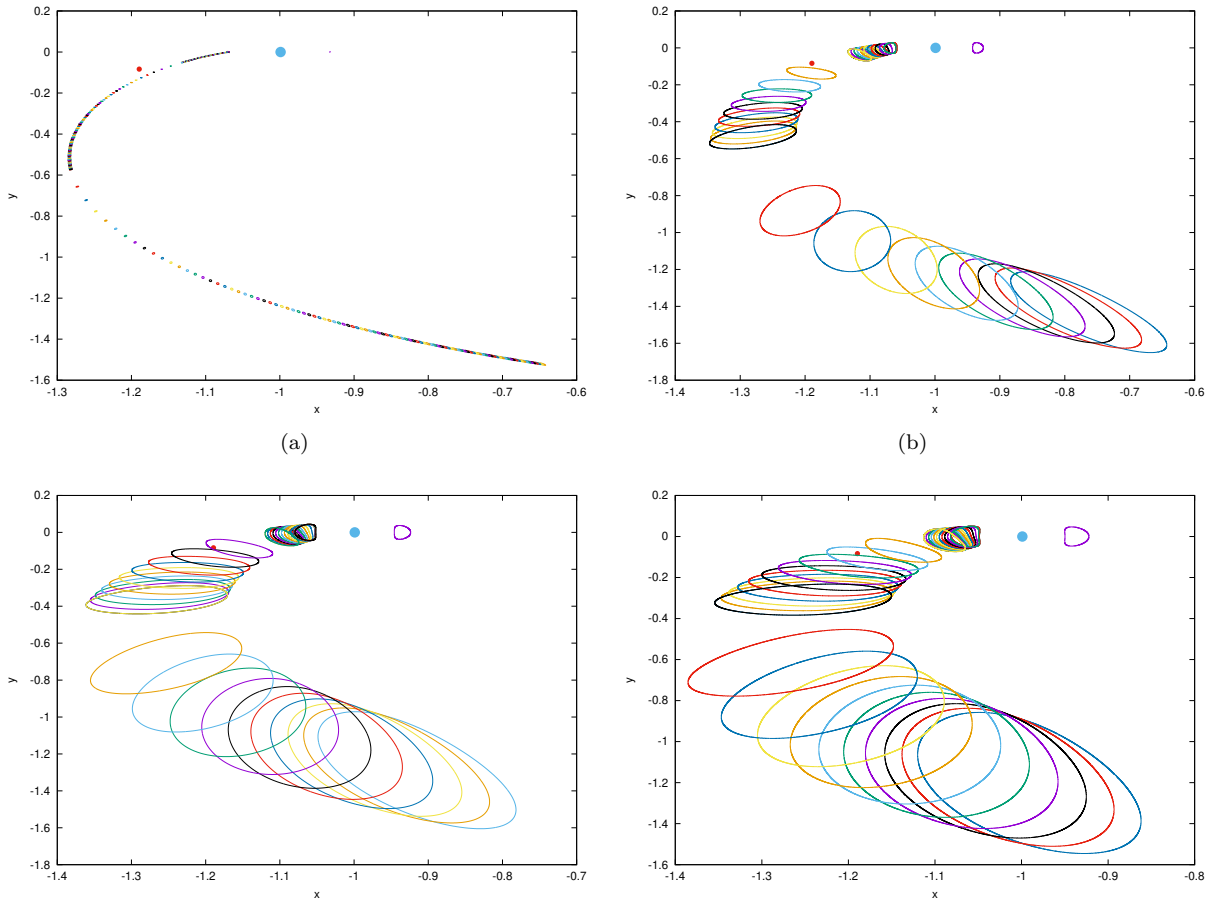

Figure 6.2: Plots of the stable manifolds of the tori (a) $T^{L_2}_{-1330}$, (b) $T^{L_2}_{0}$, (c) $T^{L_2}_{2000}$, (d) $T^{L_2}_{3167}$, together with Oterma position in section Σ_π. The red point is Oterma and the blue one Jupiter.

them by a spatial section (inside the temporal ones), they will be represented respectively by a point and a closed curve.

Let us look for some spatial sections inside Σ_π on which we would be able to conclude some results about the dynamical objects that play a key role in Oterma's dynamics.

Based on what was presented in Chapter 4, we will look for sections in the x variable inside the temporal sections.

Define x_O, x_J as the x-coordinates of Oterma and Jupiter, respectively, in Σ_π.

Once again, choosing Σ_π as the section where the computations are done and shown is not mandatory and it is simply a choice, but as we are going to present now some sections (specifically, when $x = x_O$ and $x = x_J$), we should compute the intersections of the manifolds with these sections, and, choosing the section

where Oterma is closer, gives us the opportunity to perform less steps in the numerical integration, which permits us to have more precise results.

Remark: The above mentioned sections in x should be read as "subsections" of Σ_π, i.e., they will be sections given by $\{f = \pi, x = x_O\}$ and $\{f = \pi, x = x_J\}$.

As it may be seen by Figure 6.2, it is difficult at first sight to make a decision about which torus should be considered to be the most representative one, concerning the major influence of its manifolds over Oterma.

In order to support this choice, let us plot some intersections of the above-drawn manifolds and the section $x = x_O$. They are shown in Figure 6.3.

Recall that fixing f and x coordinates leaves us with 3 more. So, instead of showing a 3D plot (coordinates (y, p_x, p_y)), Figure 6.3 shows the projections (y, p_x), (y, p_y) and (p_x, p_y) for a better visualization.

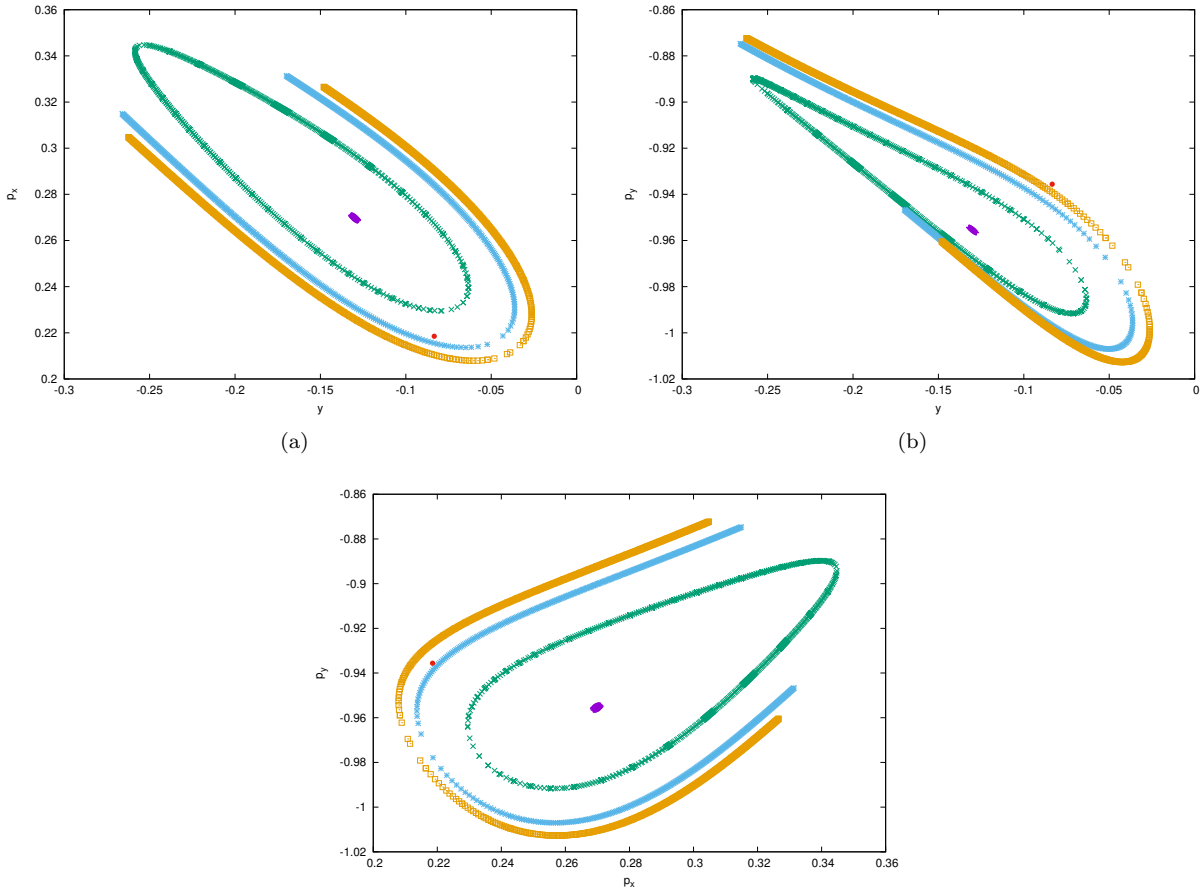

(a) (b)

(c)

Figure 6.3: Sections (a) $\{(y, p_x)/f = \pi, x = x_O\}$, (b) $\{(y, p_y)/f = \pi, x = x_O\}$, (c) $\{(p_x, p_y)/f = \pi, x = x_O\}$. The red point is Oterma; in purple, the stable manifold of $T^{L_2}_{-1330}$; in green, the stable manifold of $T^{L_2}_{0}$; in blue, the stable manifold of $T^{L_2}_{2000}$; and, in orange, the stable manifold of $T^{L_2}_{3167}$.

There is a considerable computational effort involved in the computation of the intersections of the manifolds and the temporal+spatial secions. Hence we have presented, in Figure 6.3, the parts of these manifolds which are closer to Oterma. Notice that, as shown in Figure 6.2(d), the range of y is wider than the one presented in Figure 6.3. For $T^{L_2}_{3167}$ and $T^{L_2}_{2000}$ this slice is a connected curve while, for the other two tori, it would be represented by two connected curves.

If we intersect the manifolds of every torus around L_2 with the section $x = x_O$ we would obtain a two-dimensional manifold (that contain the numerically computed curves in Figure 6.3 but that expands beyond them) in this three-dimensional environment, so that it is not mandatory for Oterma to belong to this submanifold, which means that there is a minimum distance between them.

For the four tori around L_2 presented so far, we have computed, not the above-mentioned minimum distance, instead the distances between the slices of their manifolds in the four-dimensional space Σ_π, to obtain the data presented in Table 6.1.

tori	ω	distance	number of curves used
$T^{L_2}_{-1330}$	12.42712293886	6.95×10^{-2}	10000
$T^{L_2}_{0}$	12.29412293886	2.34×10^{-2}	1000
$T^{L_2}_{2000}$	12.09412293886	8.55×10^{-3}	1000
$T^{L_2}_{3167}$	11.97742293886	5.04×10^{-3}	1000

Table 6.1: Approximation to the distances of the presented manifolds of the tori to Oterma and number of curves used on each of them on the mesh of the fundamental domain.

It should se mentioned that there is no formal reason to selected these tori, it could have been other ones. They were selected because their intersections in a temporal+spatial section that will be discussed future in this chapter illustrate some of the main features we would like to discuss.

We choose the greater torus ($T^{L_2}_{3167}$) to be the one we will analyse in more details, as the distance is small and, from what can be seen in Figure 6.3 it cannot be improved by a significant amount (notice that, in Figures 6.3(a) and 6.3(c), Oterma is in between the manifolds of the second and the third torus while, in Figure 6.3(b), it is beyond the greater one), i.e., this is a good approximation for the distance between the family of stable manifolds of the tori around L_2 and Oterma.

Having computed the torus we will use as a representative of the greater influence of their manifolds over Oterma, let us see how its manifolds relate to ones of tori around L_1.

For this let us plot, now, intersections of the stable and the unstable manifolds of some tori around L_1 and L_2 in $x = x_J$.

Figure 6.4 shows these intersections for the greater tori.

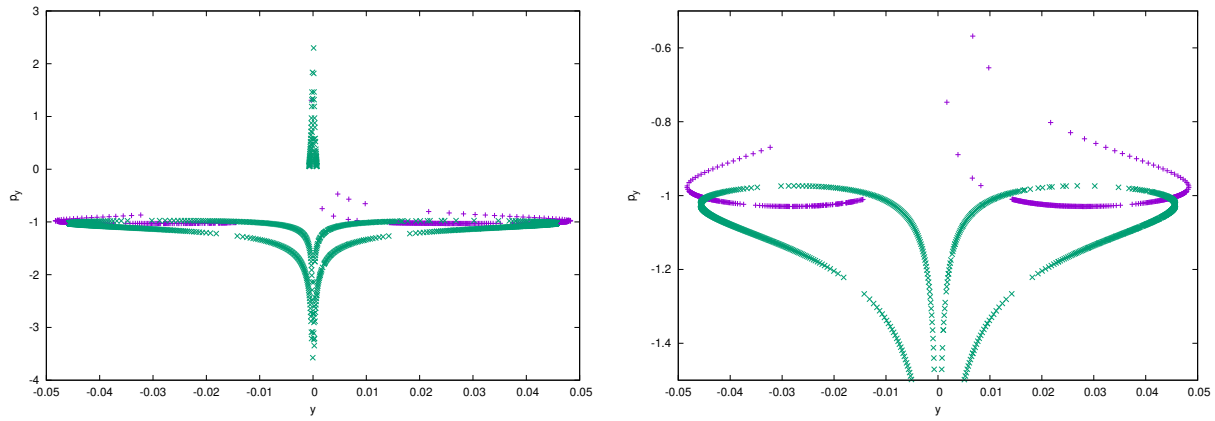

(a) (b)

Figure 6.4: Sections $\{(y, p_y)/f = \pi, x = x_J\}$. The purple points are the intersection of the manifolds of L_2 (the ones with $y > 0$ are the stable one, and the ones with $y < 0$ the unstable), and the ones in green, of L_1 (the opposite stability code for this case).

Notice the resemblance of Figures 6.4 and 4.5.

This means, as in the case of the PCRTBP, that there are heteroclinic connections between tori near L_1 and L_2, so that the transition is possible in the case of the PERTBP.

Let us see now the intersection of manifolds of more than one torus.

Figure 6.5 may be understood as the superposition of two types of behaviour presented in Figures 4.5 and 4.4, where there are presented the intersection and the no-intersection phenomena.

Let us see now, how to fit Oterma inside this framework of intersections of manifolds.

If we were dealing with the PCRTBP we could simply integrate Oterma until it reaches the section and visualize it, but, as the PERTBP is a non-autonomous sytem (in particular, the system of coordiantes adopted in this thesis varies with the independent variable), the path is not as simple as this.

In order to have Oterma represented in this section (of Figures 6.4 and 6.5) we should compute all the objects (tori, manifolds, intersections) in a new f - the one that makes Oterma and Jupiter to have the same x-coordinates.

This value of f is computed by integrating Oterma in the PERTBP flow until it reaches the same x-coordinate as Jupiter. Let f^* be such value of f.

Recall that the value of f for the initial conditions of Oterma (the one chosen based in the numerical experiments of Chapter 3) is given by $f_0 = 3.8817002439241626$.

Integrating forward (as Oterma's initial position were chosen before the transition to happen), we have that the value of f^* is given by $f^* = 4.750563615740$.

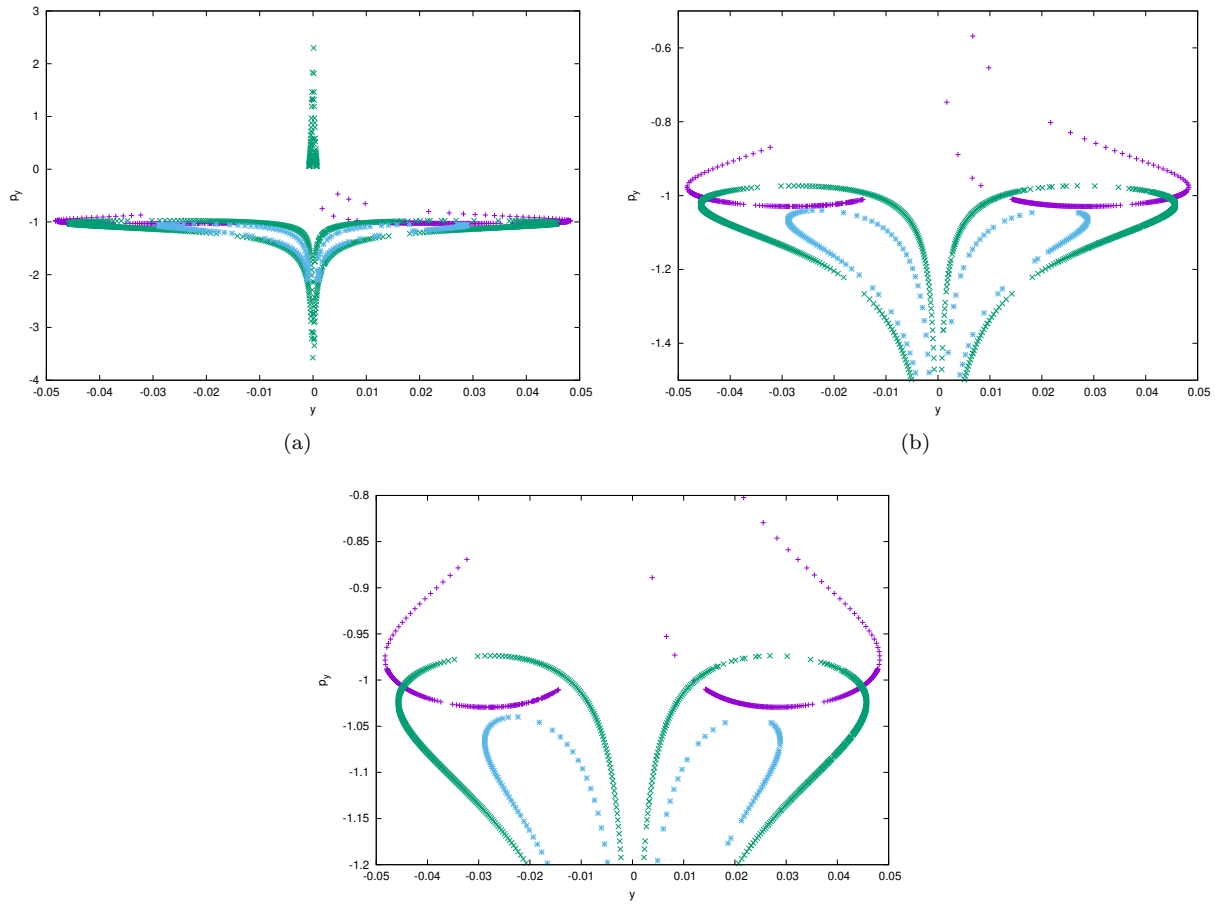

Figure 6.5: Sections $\{(y, p_y)/f = \pi, x = x_J\}$. The purple points are the intersection of the manifolds of L_2 (the ones with $y > 0$ are the stable one, and the ones with $y < 0$ the unstable), and the ones in green and in blue, for L_1 (the opposite stability code for this case).

Notice that, for this value, we have that f^* is slightly greater than $\dfrac{3\pi}{2} \approx 4.71238898$, as it was expected from Figure 6.1(d).

So, it is a good choice to compute the objects we would like to visualize starting from $\Sigma_{\frac{3\pi}{2}}$, as the instability produced by the numerical integration will be smaller.

Remark: It is important to state here that all the computations from the start could have been done taking, instead of the sections $\Sigma_{\frac{i\pi}{2}}$ of the phase space, sections related to Σ_{f^*}. Everything was computed in a more general frame to show that it is not dependent on the problem and that it is easier to go from a general computation to a specific one than the opposite way, we could, for instance be interested in also computing all the objects in Σ_{f_0} and this section would not be an chosen one if we had everything strictly related from to beginning to f^*.

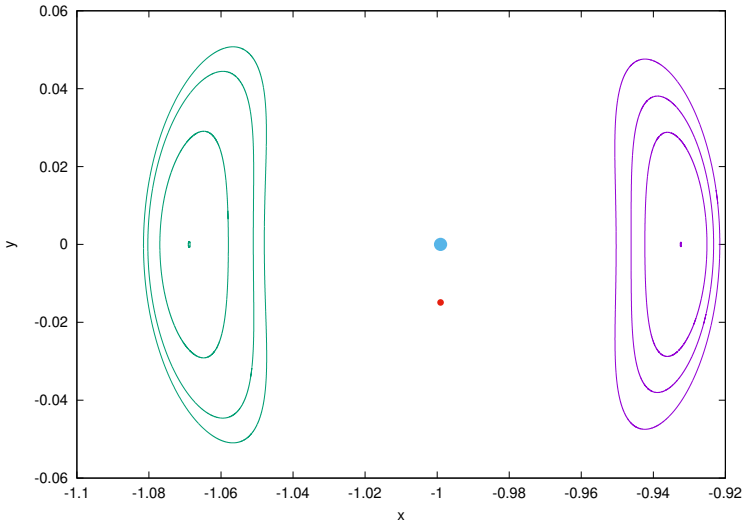

Figure 6.6: Some tori around L_1 and L_2 together with Oterma and Jupiter in Σ_{f^*}. These tori are the ones whose manifolds were computed and will be shown in the following figures.

Figure 6.6 shows the tori around L_2 described in Table 6.1 and, the ones around L_1, with rotation numbers $\omega = 13.68754470049$, $\omega = 13.43094470049$, $\omega = 13.23094470049$ and $\omega = 12.96064470049$, being the ones with greater rotation number the smaller ones.

So, from now on, to reproduce Figures 6.4 and 6.5 visualizing also Oterma, we should proceed to the computation of the section $\{f = f^*, x = -1 + \mu\}$. This means that in the following figures, we will be presenting some intersections of manifolds with this section and how they are related to Oterma.

As stated before, as the codimension of the manifolds of the tori is 2, we cannot say, in this context of the PERTBP, that they divide the space in "inside" and "outside" regions. We will, however, be referring to some regions in the sections using these words, by an abuse of speech, due to the similarities with the PCRTBP, as we are considering a short time interval to study the targeted phenomenon (the Rapid Transition Mechanism).

We start by showing, in Figure 6.7, the intersection of the manifolds of the largests tori ($T^{L_1}_{4704}$ and $T^{L_2}_{3167}$).

It is important to notice, from Figure 6.7, that Oterma is inside the region between the two manifolds. This means that these tori can be considered as responsibles for influencing in Oterma's transition.

In what follows we will see examples of pairs of tori which cannot be considered to explain Oterma's transition.

In Figures 6.8(a) and 6.8(b) we can see that, even though the intersection of these manifolds exist, Oterma is not inside the region between them - it is inside each of them separetely - which does not guarantee the rapid transition.

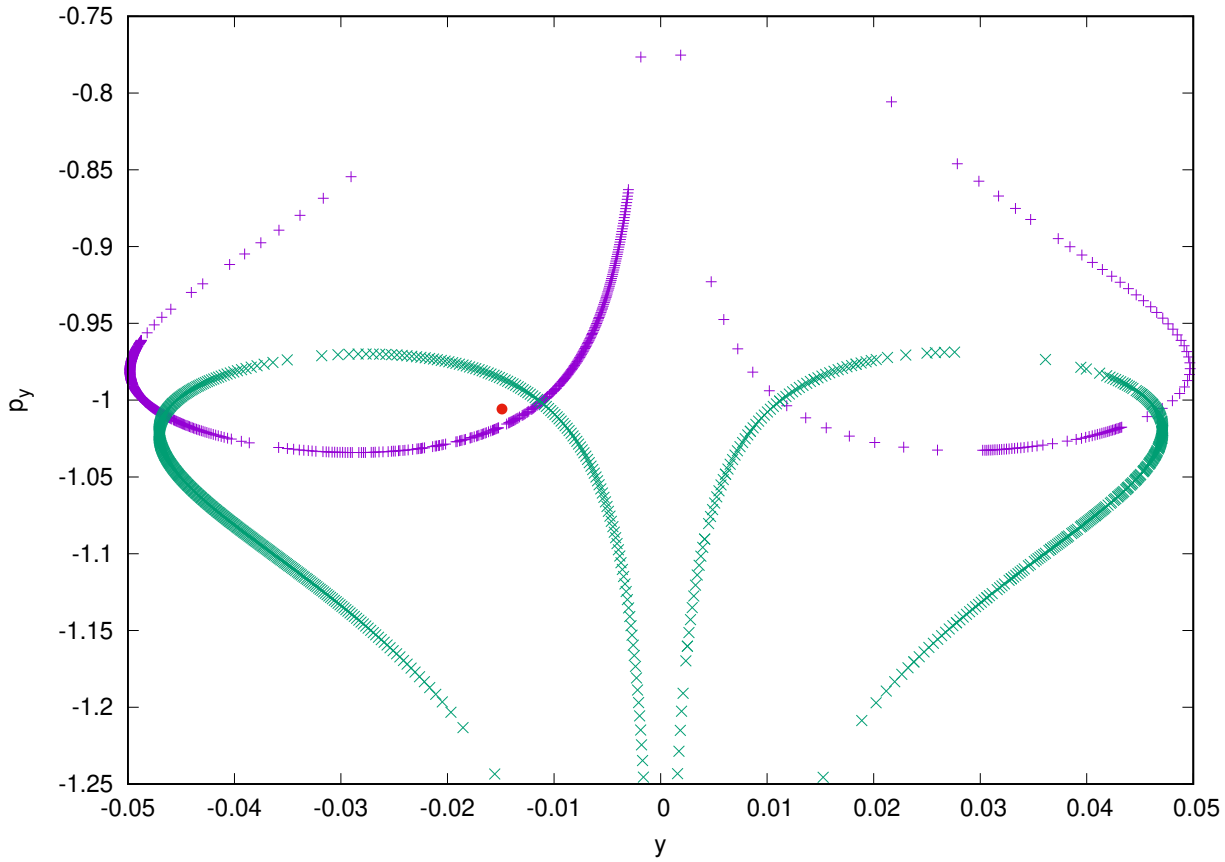

Figure 6.7: Intersection of manifolds of the tori $T^{L_1}_{4704}$ (in green) and $T^{L_2}_{3167}$ (in purple) together with Oterma (in red).

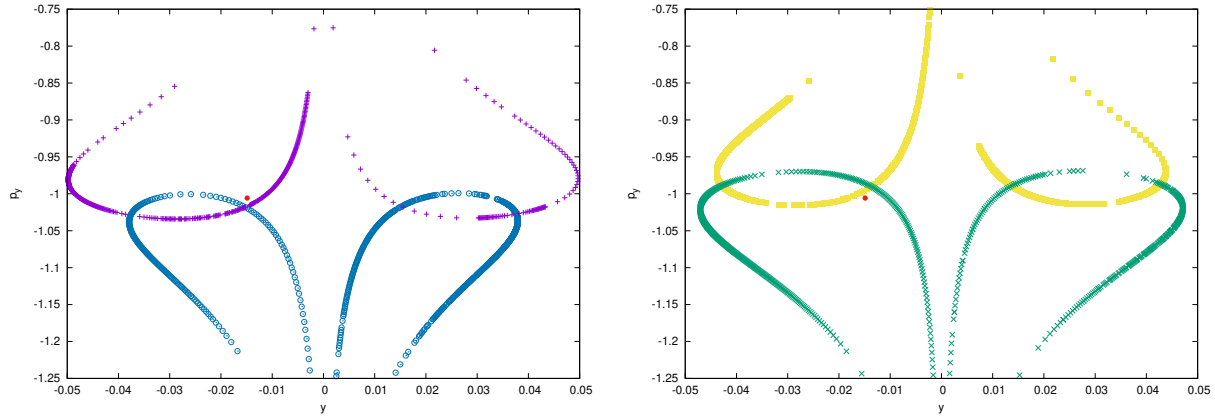

(a) (b)

Figure 6.8: Intersection of manifolds of the tori (a) $T^{L_1}_{2000}$ (in blue) and $T^{L_2}_{3167}$ (in purple); (b) $T^{L_1}_{4704}$ (in green) and $T^{L_2}_{2000}$ (in yellow) together with Oterma (in red).

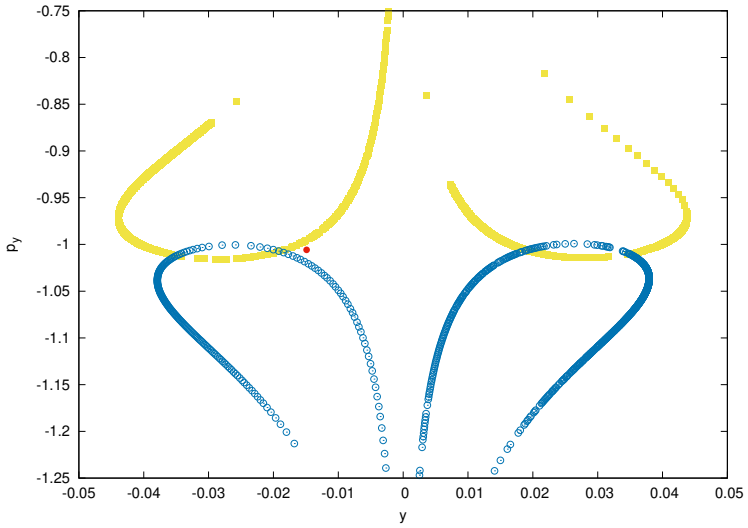

Figure 6.9: Intersection of manifolds of the tori $T^{L_1}_{2000}$ (in blue) and $T^{L_2}_{2000}$ (in yellow) together with Oterma (in red).

We may see, from Figure 6.9 that the manifolds pictured there intersect, but that Oterma is outside the region between them. So for this transition mechnism, the existence of an intersection does not imply directly a transition.

Figure 6.10 shows the intersection of the four above-mentioned tori all plotted together.

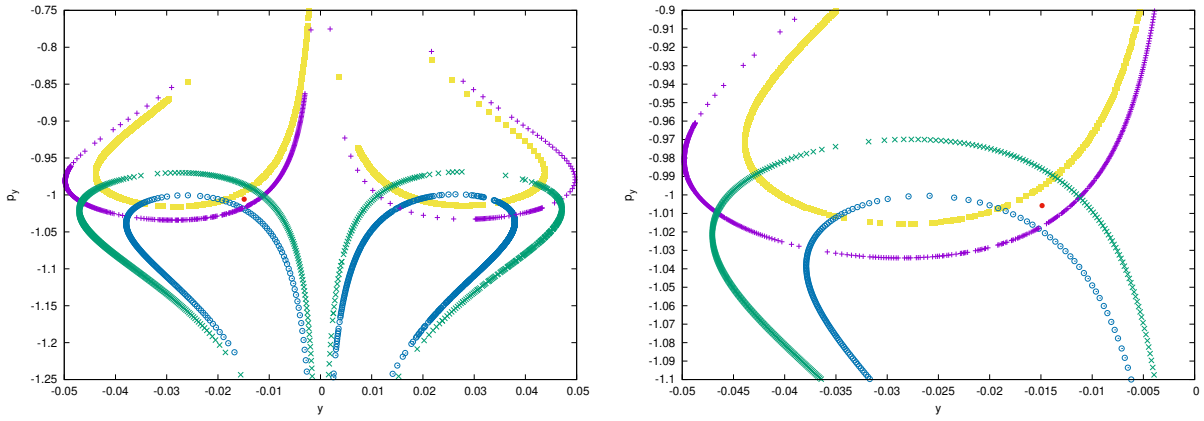

(a) (b)

Figure 6.10: Intersection of manifolds of the tori $T^{L_1}_{4704}$ (in green), $T^{L_1}_{2000}$ (in blue), $T^{L_2}_{3167}$ (in purple) and $T^{L_2}_{2000}$ (in yellow) together with Oterma (in red).

For the tori computed from the continuation with respect to the eccentricity from the initial periodic orbits in the PCRTBP we have the sections shown in Figure 6.11.

Notice the resemblance of Figures 6.11 and 4.4.

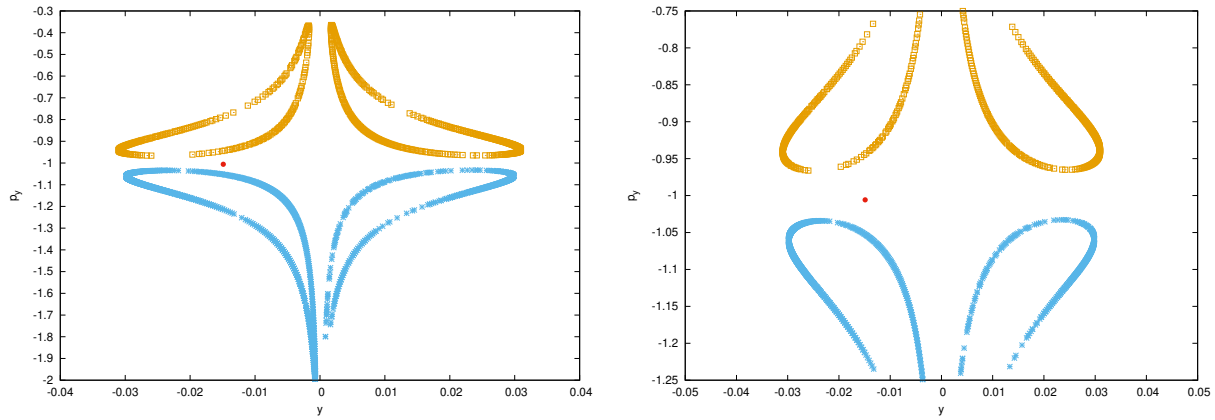

Figure 6.11: Intersection of manifolds of the tori $T_0^{L_1}$ (in light blue) and $T_0^{L_2}$ (in orange) together with Oterma (in red).

Finally, let us plot all the intersection of all eight above tori.

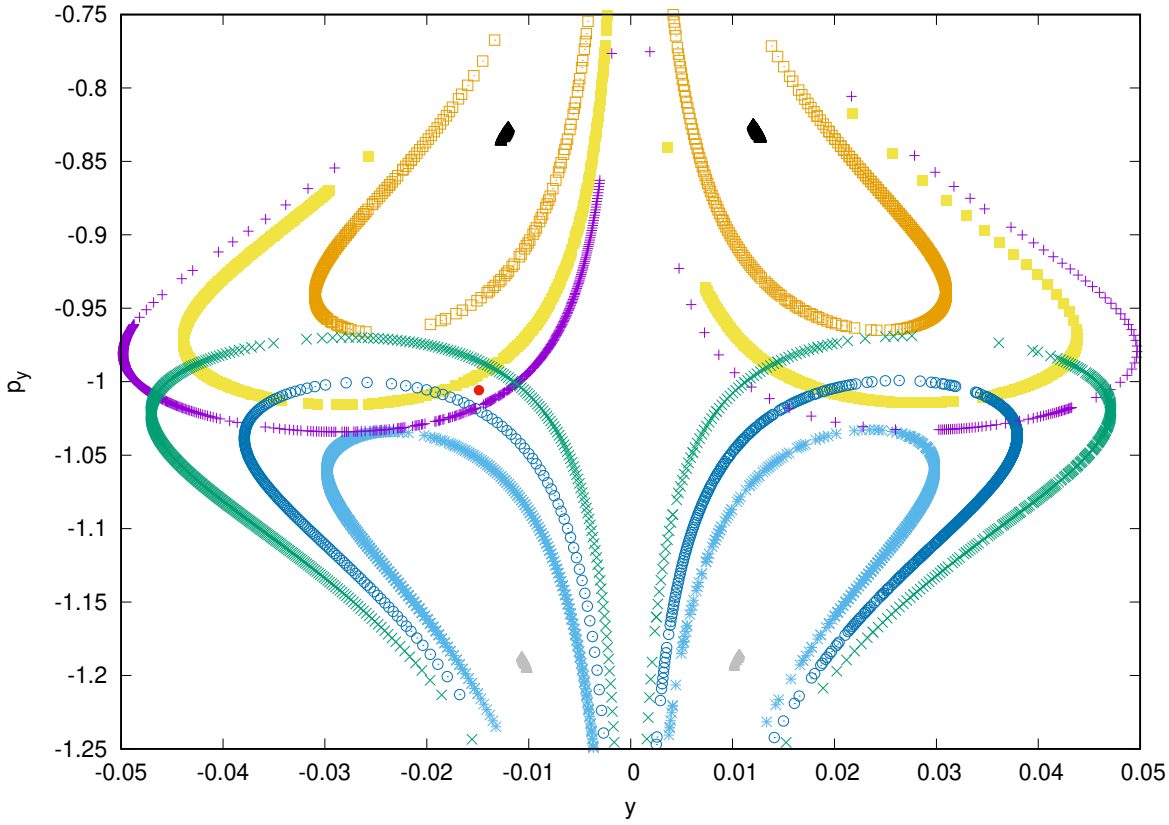

Figure 6.12: Intersection of manifolds of the tori $T_{4704}^{L_1}$ (in green), $T_{2000}^{L_1}$ (in blue), $T_0^{L_1}$ (in light blue), $T_{-2565}^{L_1}$ (in gray), $T_{3167}^{L_2}$ (in purple), $T_{2000}^{L_2}$ (in yellow), $T_0^{L_2}$ (in orange) and $T_{-1330}^{L_2}$ (in black) together with Oterma (in red).

It is important to recall that these intersections presented here in this chapter are the first intersections of the manifolds and the sections, i.e., as it could be seen in Chapter 5, if we integrate for a longer time, the manifolds will have more intersections, but, as we are interested in the Rapid Transition Mechanism, we discard the intersections which revolve around Jupiter.

In summary, in this chapter we have seen that it is possible to identify the dynamical objects the influence Oterma to do the transition between different regions in the configuration space of the PERTBP and visualize them together with Oterma using some temporal+spatial section that are ought to be chosen carefully. This was possible due to

- the use of numerical techniques described in Chapter 5, namely, how to compute a torus, how to continue it with respect to a parameter, how to compute its invariant stable and unstable manifolds and the usage of parallel shooting to diminish the instability involved in these computations;
- the possibility to fit Oterma in the PERTBP via a change of variables discussed in Chapter 2;
- the fact that the PERTBP can be seen as a periodic perturbation of the PCRTBP where the theory of this transition mechanism was already stated, although, for the case of analysing Oterma's real data, the latter model is not accurate enough, as the comet has a different behaviour than what it is expected.

Chapter 7

Conclusions and Perspectives

As conclusions, we can mention:

- according to [KLM+01], it is possible to see the transition in the PCRTBP, i.e., there exists some initial conditions for Equations (1.6) such that this behaviour of transitioning between regions in the phase space, as shown in Figures 1.3 and 2.3;

- contrasting [KLM+01], it was possible to fit Oterma's orbit in the PCRTBP, although it was necessary some adjustments in its velocity in order to compensate the oversimplification of this model, so that its behaviour could be accurate (Figures 2.2 and 2.3), in other words, in the real problem, even if one consider just Sun and Jupiter as the primaries, their movement is elliptic (with small eccentricity) and three-dimensional (with relatively small movement in the vertical direction), so, even though these quantities - Jupiter's eccentricity and the vertical component of the movement - are small, they can contribute to make this model not accurate enough;

- besides that, still concerning the PCRTBP, there are some energy levels where one can see connections between the stable/unstable manifolds of the periodic oribts around L_1 and L_2, being these connections the way for a rapid transition from outside to inside and vice-versa;

- in the PERTBP this feature of presence or absence of intersection of manifolds in also the key mechanism for the transition of Oterma, and we are able to see some manifolds intersectioning and some not; the diference now is that there is no level of energy that prevent different objects (periodic orbits in the PCRTBP, tori in the PERTBP) to intersect through their stable and unstable manifolds, i.e., while a periodic orbit around L_2 can interact with just one around L_1, this is not true anymore for the

tori around the equilibrium points in the PERTBP;

- when fitting Oterma's data in the PERTBP, it is possible to see the Rapid Transition Mechanism (explained in Chapter 1), although it was a partial one, as for the returning to the original region it was not rapid, but with a revolution around Jupiter, this is due to the fact the projecting Oterma in the Sun-Jupiter's plane of movement modifies its trajectory enough to have an influence on qualitative results;

As future works, to name a few, we can cite:

- use the SERTBP as a model to compare the accuracy of the results obtained here;
- based on the computations of Chapter 4, look for other model in Celestial Mechanics to try to extend the validity of the modelling process for Oterma's dynamics, like the Bicircular or the Quasi-Bicircular ones, or even a Bielliptic as both Jupiter and Saturn have elliptic orbits;
- the pseudo-arc length algorithm were presented for the case of periodic orbits, but not for tori, as it was not implemented in this case; it can be a possible direction to investigate the presence or absence of turning points and bifurcations in the case of continuing the tori in the PERTBP, specially for greater values of the eccentricity;
- study the resonant tori present in the continuation process;
- a goal that is more immediate is to study the whole family of tori, i.e., not to interrupt the continuation until either they approach the smaller primary or they are destroyed by other phenomenon;
- another easy one is to compute these objects for systems with other eccentricities;
- study Temporary Satellite Capture to investigate collisions, in the Sun-Jupiter case or, even more interestingly, in the Sun-Earth or the Earth-Moon cases;
- there are some works that deal with maneuvers in order to get some advantages of these manifolds to do some prescribed trajectory, like [GKM+04]; the tools studied here may be also used for these situations, so it can be another scenario to investigate.

Appendix A

Computation of Periodic Orbits and their Invariant Manifolds

We write this appendix in order to make this thesis as self-contained as possible.

Everything that is written here is already known in the literature and the tools and methods presented here were extensively applied not just to celestial mechanics problems, but to a variety of other areas.

The goal of this appendix is to present this knowledge in an easier environment and as simple as possible, so that, when dealing with tori, we could be able to reference the ideas and insights from here when it is necessary to make the reading of Chapter 5 easier.

A.1 How to Compute a Periodic Orbit?

Let

$$\dot{x} = f(x) \tag{A.1}$$

define a dynamical system which we would like to study, where $x \in \mathbb{R}^n$.

Define

$$\begin{array}{rccc} P\colon & \Sigma \subset \mathbb{R}^n & \to & \Sigma \subset \mathbb{R}^n \\ & x & \mapsto & P(x), \end{array}$$

where Σ is a smooth manifold, of dimension $n-1$, transversal to the flow, as a map depending on the flow.

Remark: It is also possible to use temporal Poincaré sections to study a dynamical system. In fact, this will be applied in Chapter 5.

In any of the above-mentioned cases, the (system of) differential equation(s) are to be numerically integrated.

In order to compute a periodic orbit in this system, together with Equation (A.1), we should integrate also a set of n^2 equations known as variational equations.

The idea behind the variational equations is to study how small variations in the initial data affect the flow.

Changing notation, let $x(t; x_0)$ be a solution of (A.1) on itme t having as initial condition x_0. We will assume, without loss of generality that the initial time is 0.

Writing again Equation (A.1), we have $\frac{d}{dt}x(t; x_0) = f(x(t; x_0))$.

Deriving with respect to x_0, we have $\left(\frac{d}{dt}(D_{x_0}x(t; x_0)) =\right) D_{x_0}\left(\frac{d}{dt}x(t; x_0)\right) = D_{x_0}f(x(t; x_0))$.

By the chain rule, $\frac{d}{dt}(\underbrace{D_{x_0}x(t; x_0)}_{V}) = D_x f(x(t; x_0))D_{x_0}x(t; x_0)$.

As $V = D_{x_0}x(t; x_0)$, it is true that, in the initial time $t = 0$, $x = x_0$, so that $V = I$.

So, the system we should integrate is the following

$$\begin{cases} \dot{x} &= f(x) \\ \dot{V} &= D_x f(x)V \end{cases} \tag{A.2}$$

with initial conditions

$$\begin{cases} x(0) &= x_0 \\ V(0) &= I \end{cases} \tag{A.3}$$

If we are interested in computing a periodic orbit, we can consider the map P, independently of the case - whether it is defined as an integration for a fixed amount of time, or integration until a hypersurface is reached - the solution of the equation $P(x_0) = x_0$ gives us the initial condition x_0 that gives rise to a periodic orbit.

This equation can be written as

$$F(x) = P(x) - x = 0,$$

with derivative

$$DF(x) = DP(x) - I,$$

and the problem now turns out to be finding a zero of a system of equations.

Applying Newton's method for nonlinear systems of equations, we have the following iteration scheme

$x_{k+1} = x_k - (DF(x_k))^{-1}F(x_k)$, but inverting matrices is an expensive process, so that this scheme can be written as $DF(x_k)(x_{k+1} - x_k) = -F(x_k)$.

Calling $h_k = x_{k+1} - x_k$, the iteration we should solve to compute the initial conditions of a periodic orbit is given by

$$\begin{cases} DF(x_k)h_k &= -F(x_k) \\ x_{k+1} &= x_k + h_k. \end{cases}$$

A.1.1 Initial Guess

Unfortunately, there is no general method that one can apply to compute a good approximation to a set of initial conditions, with which the Newton's method will converge, it is something that should be examinated case by case, and can be a big problem by itself.

There are some cases where some strategies can be applied.

Specifically in the PCRTBP, for L_1 and L_2 (our focus here in this thesis), there is a one-parametric family of periodic orbits around each of them, the Lyapunov familt of periodic orbits, so that the task of looking for initial conditions is somehow easier.

If we fix an energy level and use a section, say, $y = 0$, then we should define two more variables: We have four variables (x, y, p_x, p_y), fixing $y = 0$ we have three left, and, by fixing the energy level, it is possible to compute one of the variables with respect to the others, using the expression of the Hamiltonian (1.3).

Although it is a gain to have reduced the dimension of the space where to look for a solution, this is not enough for us to say that now it is not difficult to find initial conditions to compute an orbit, specially because, in the case of L_1 and L_2, the biggest eigenvalue of the monodromy matrix is of order $\sim 10^3$, this computation turns out to be quite unstable, in the sense that, we would need very good initial condition for the Newton's method to ensure a convergence of it.

Remark: To overcome this difficulty is precisely the idea of the parallel shooting, that will be explained in the next section. We, in fact, have used it to compute the above-mentioned periodic orbits.

A.1.2 Variational Matrix

For a general dynamical system (A.1), the variational matrix is given by

$$D_x f(x(t;x_0)) = \begin{pmatrix} \left.\frac{\partial f_1}{\partial x_1}\right|_x & \left.\frac{\partial f_1}{\partial x_2}\right|_x & \cdots & \left.\frac{\partial f_1}{\partial x_n}\right|_x \\ \left.\frac{\partial f_2}{\partial x_1}\right|_x & \left.\frac{\partial f_2}{\partial x_2}\right|_x & \cdots & \left.\frac{\partial f_2}{\partial x_n}\right|_x \\ \vdots & \vdots & \ddots & \vdots \\ \left.\frac{\partial f_n}{\partial x_1}\right|_x & \left.\frac{\partial f_n}{\partial x_2}\right|_x & \cdots & \left.\frac{\partial f_n}{\partial x_n}\right|_x \end{pmatrix},$$

where we are using the notation $x = (x_1, x_2, \cdots, x_n)$ and $f(x) = (f_1(x), f_2(x), \cdots, f_n(x))$.

In the case of the PCRTBP (Equations (1.6)) the matrix is given by

$$\begin{pmatrix} \frac{\partial \dot{x}}{\partial x} & \frac{\partial \dot{x}}{\partial y} & \frac{\partial \dot{x}}{\partial p_x} & \frac{\partial \dot{x}}{\partial p_y} \\ \frac{\partial \dot{y}}{\partial x} & \frac{\partial \dot{y}}{\partial y} & \frac{\partial \dot{y}}{\partial p_x} & \frac{\partial \dot{y}}{\partial p_y} \\ \frac{\partial \dot{p_x}}{\partial x} & \frac{\partial \dot{p_x}}{\partial y} & \frac{\partial \dot{p_x}}{\partial p_x} & \frac{\partial \dot{p_x}}{\partial p_y} \\ \frac{\partial \dot{p_y}}{\partial x} & \frac{\partial \dot{p_y}}{\partial y} & \frac{\partial \dot{p_y}}{\partial p_x} & \frac{\partial \dot{p_y}}{\partial p_y} \end{pmatrix} = \begin{pmatrix} 0 & 1 & 1 & 0 \\ -1 & 0 & 0 & 1 \\ \frac{\partial \dot{p_x}}{\partial x} & \frac{\partial \dot{p_x}}{\partial y} & 0 & 1 \\ \frac{\partial \dot{p_y}}{\partial x} & \frac{\partial \dot{p_y}}{\partial y} & -1 & 0 \end{pmatrix}, \tag{A.4}$$

where r_1 and r_2 are the distances between the particle and the primaries located in $(-1+\mu, 0)$ and $(\mu, 0)$, respectively, and

- $\frac{\partial \dot{p_x}}{\partial x} = -\frac{(1-\mu)(r_1^2 - 3(x-\mu)^2)}{r_1^5} - \frac{\mu(r_2^2 - 3(x+1-\mu)^2)}{r_2^5}$;
- $\frac{\partial \dot{p_x}}{\partial y} = \frac{\partial \dot{p_y}}{\partial x} = 3\frac{(1-\mu)(x-\mu)y}{r_1^5} + 3\frac{\mu(x+1-\mu)y}{r_2^5}$;
- $\frac{\partial \dot{p_y}}{\partial y} = -\frac{(1-\mu)(r_1^2 - 3y^2)}{r_1^5} - \frac{\mu(r_2^2 - 3y^2)}{r_2^5}$.

A.1.3 A Spatial Section

The idea behind using sections to compute the periodic orbit, in addition to turn its computation into a root-finding problem, also transform the dynamical system from a continuous world to the discrete one, since

now, we can define the map

$$\begin{aligned} \Sigma \subset \mathbb{R}^2 \quad &\longrightarrow \quad \Sigma \subset \mathbb{R}^2 \\ (x, p_x) \quad &\longmapsto \quad (\overline{x}, \overline{p_x}), \end{aligned}$$

integrating (x, p_x) until they reach the final section.

Remark: In the easiest case, one can use the same section as the one from where the flow departs and arrives, and so far, that is the case that has been explained so far in this section. In the next section, it will be presented a tool, called parallel shooting, in which one can define several sections in order to overcome numerical instabilities.

In more details, in the case of the PCRTBP, the above map is given by

$$\begin{pmatrix} x \\ p_x \end{pmatrix} \overset{\Pi_0}{\longmapsto} \begin{pmatrix} x \\ y(=0) \\ p_x \\ p_y \end{pmatrix} \overset{\phi}{\longmapsto} \begin{pmatrix} \overline{x} \\ \overline{y}(=0) \\ \overline{p_x} \\ \overline{p_y} \end{pmatrix} \overset{\Pi_1}{\longmapsto} \begin{pmatrix} \overline{x} \\ \overline{p_x} \end{pmatrix}, \tag{A.5}$$

where p_y is calculated using the expression of $H(x, y, p_x, p_y)$.

The phase space on which we integrate the system (1.6) is four dimensional, so there are four vectors that form the variational matrix.

It is not guaranteed that those four vectors land exactly inside the desired section, as it is illustrated by Figure A.1.

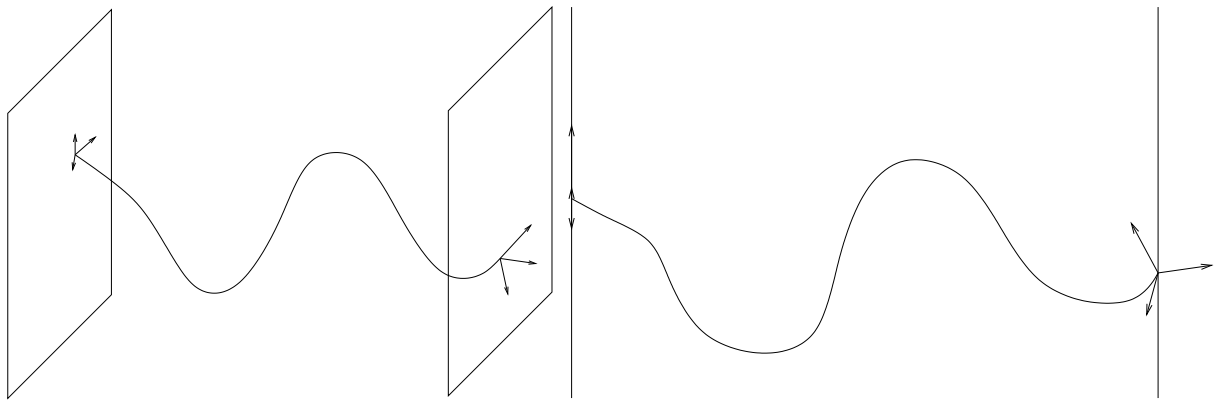

(a) (b)

Figure A.1: Illustration of an integrated flow from one hypersurface to another one on the phase space, together with the vectors that form the variational matrix. (a) A general point of view. (b) A highlight in the fact that these vectors, in general, do not lie inside the final section.

In order to have an application in which the vectors land inside the section, we can project them over it in the direction of the flow tangent vector.

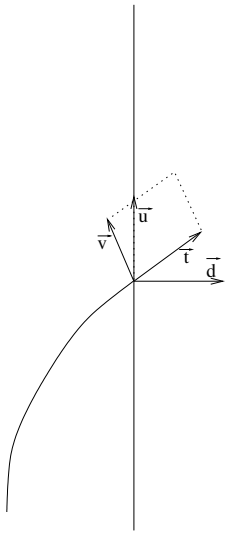

Figure A.2: Illustration of the projection of one of the column vectors of the variational matrix in the direction of the vector tangent to the flow. $\vec{d}$ is the section normal vector; $\vec{t}$ is the flow tangent vector; $\vec{v}$ is a vector that form the variational matrix to be projected; $\vec{u}$ is the projection of $\vec{v}$ in $\vec{t}$ direction.

A simple computation gives us the vector $\vec{u}$:

Let $\vec{u} = \vec{v} + \alpha\vec{t}$, the value of α to be determined.

As $< \vec{d}, \vec{u} >= 0$, by the bilinearity of $< \cdot, \cdot >$ we can see that $\alpha = -\dfrac{< \vec{d}, \vec{v} >}{< \vec{d}, \vec{t} >}$.

So, doing this for all the column vectors of the variational matrix, we would have the an approximation of these vectors lying inside the section.

Let us now check how to handle the mapping (A.5).

Calling $\Phi = \Pi_1 \circ \phi \circ \Pi_0$, we have, for the derivatives

$$\begin{aligned} D\Phi &= D\Pi_1 \cdot D\phi \cdot D\Pi_0 \\ &= \begin{pmatrix} 1 & 0 & 0 & 0 \\ 0 & 0 & 1 & 0 \end{pmatrix} \begin{pmatrix} v_{11} & v_{12} & v_{13} & v_{14} \\ v_{21} & v_{22} & v_{23} & v_{24} \\ v_{31} & v_{32} & v_{33} & v_{34} \\ v_{41} & v_{42} & v_{43} & v_{44} \end{pmatrix} \begin{pmatrix} 1 & 0 \\ 0 & 0 \\ 0 & 1 \\ \dfrac{\partial p_y}{\partial x} & \dfrac{\partial p_y}{\partial p_x} \end{pmatrix} \\ &= \begin{pmatrix} v_{11} + \dfrac{\partial p_y}{\partial x} v_{13} & v_{13} + \dfrac{\partial p_y}{\partial p_x} v_{14} \\ v_{31} + \dfrac{\partial p_y}{\partial x} v_{34} & v_{33} + \dfrac{\partial p_y}{\partial p_x} v_{34} \end{pmatrix}. \end{aligned}$$

The values of $\dfrac{\partial p_y}{\partial x}$ and $\dfrac{\partial p_y}{\partial p_x}$ are computed via implicit derivation of (1.3):

We may rewrite this equation isolating the terms with contain p_y as

$$p_y^2 - 2xp_y = 2H - p_x^2 - 2yp_x + \frac{2-2\mu}{\sqrt{(x-\mu)^2+y^2}} + \frac{2\mu}{\sqrt{(x-\mu+1)^2+y^2}}.$$

- Derivating with respect to x: $2p_y\dfrac{\partial p_y}{\partial x} - 2p_y - 2x\dfrac{\partial p_y}{\partial x} = -\dfrac{(2-2\mu)(x-\mu)}{((x-\mu)^2+y^2)^{3/2}} - \dfrac{2\mu(x-\mu+1)}{((x-\mu+1)^2+y^2)^{3/2}}$, so $\dfrac{\partial p_y}{\partial x} = \dfrac{1}{x-p_y}\left(\dfrac{(1-\mu)(x-\mu)}{((x-\mu)^2+y^2)^{3/2}} - \dfrac{\mu(x-\mu+1)}{((x-\mu+1)^2+y^2)^{3/2}} + p_y\right)$.

- Derivating with respect to p_x: $2p_y\dfrac{\partial p_y}{\partial p_x} - 2x\dfrac{\partial p_y}{\partial p_x} = -2p_x - 2y$ so $\dfrac{\partial p_y}{\partial p_x} = \dfrac{p_x+y}{x-p_y}$.

A.2 Parallel Shooting

The parallel shooting technique is a numerical tool to overcome numerical difficulties when handling an environment with large instability.

Roughly speaking, the error propagation when applying the Poincaré map is proportional to the largest eigenvalue of the monodromy matrix of a mapping. This is due to the fact that this eigenvalue appears in the computation of the image of a point if we approximate it by its Taylor's series, as follows.

Let $p \in \Sigma$, being Σ a Poincaré section, be the intersection of the periodic orbit and the section. Let P be the Poincaré mapping. And let λ and v be the eigenvalue and its associated eigenvector of $DP(p)$. We have that

$$\begin{aligned} P(p+\epsilon v) &= P(p) + \epsilon DP(p)v + \cdots \\ &= p + \epsilon\lambda v + \cdots, \end{aligned}$$

which means that the eigenvalue apprears itself in the computation of the image, i.e., the separation between $P(p) = p$ and $P(p+\epsilon v)$ is proportional to the eigenvalue (as well as the initial separation).

Therefore, it is important that, besides taking and as good as possible approximation, pay a close attention to the greatest eigenvalue of the monodromy matrix, in order to be aware of the instability of the application and to decide whether it would be worthy to use or not a parallel shooting scheme.

The main idea of the parallel shooting technique is to set some sections instead of just one and integrate the flow from section to section, as illustrated in Figure A.3.

For the sake of simplicity, let us consider two sections from now on.

Remark: In fact, for the computations in this appendix, the number of sections was two. In Chapter 5 we have handled more sections as the application was more unstable.

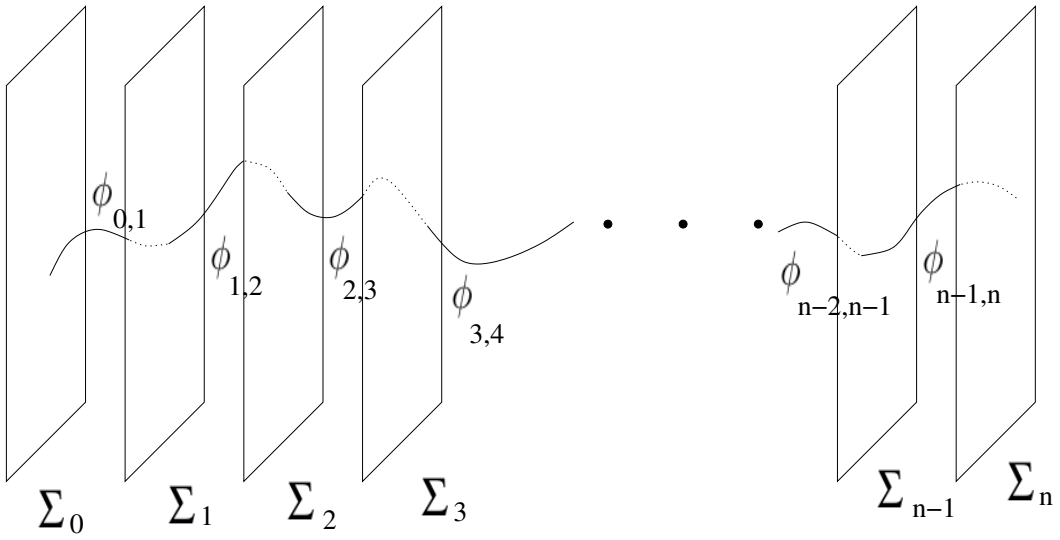

Figure A.3: Illustration of the idea of parallel shooting. It is not mandatory that the last section should be different from the first one, although that is, in general, the case.

Let Σ_0 and Σ_1 be sections that we will use to compute the periodic orbit using the parallel shooting technique.

Let $\phi_{0,1} : \Sigma_0 \longrightarrow \Sigma_1$ and $\phi_{1,0} : \Sigma_1 \longrightarrow \Sigma_0$ be the flow from Σ_0 to Σ_1 and vice-versa. To fix notation, without loss of generality, let $\phi : \Sigma_0 \longrightarrow \Sigma_0$ be the complete flow. As an abuse of notation, we will also consider $\phi : \Sigma_1 \longrightarrow \Sigma_1$ to be the complete flow.

Let also $p_0^{(0)} \in \Sigma_0$ and $p_1^{(0)} \in \Sigma_1$ be the initial guesses for the Newton's method to compute the periodic orbit.

Remark: It is important to notice that neither $p_1^{(0)}$ should be taken as $p_1^{(0)} = \phi_{0,1}(p_0^{(0)})$ nor the opposite $(p_0^{(0)} = \phi_{1,0}(p_1^{(0)}))$ because, in such a case, we would have $\phi_{1,0}(p_1^{(0)}) = \phi_{1,0}(\phi_{0,1}(p_0^{(0)})) = \phi(p_0^{(0)})$, as if we were not using the parallel shooting. Certainly the problems we have in finding an initial condition in one section are now amplified, because we are supposed to find two sets of initial conditions (one for each section), and we should have this in mind when using parallel shooting.

And finally let $p_0 \in \Sigma_0$ and $p_1 \in \Sigma_1$ be the intersections of the periodic orbit with Σ_0 and Σ_1, respectively.

These objects are shown in Figure A.4.

We have that

$$\phi(p_0) = p_0 \Longleftrightarrow \left\{ \begin{array}{rcl} \phi_{0,1}(p_0) & = & p_1 \\ \phi_{1,0}(p_1) & = & p_0 \end{array} \right. \Longleftrightarrow \Phi \begin{pmatrix} p_0 \\ p_1 \end{pmatrix} = \begin{pmatrix} p_1 \\ p_0 \end{pmatrix},$$

where $\Phi = (\phi_{0,1}, \phi_{1,0})$.

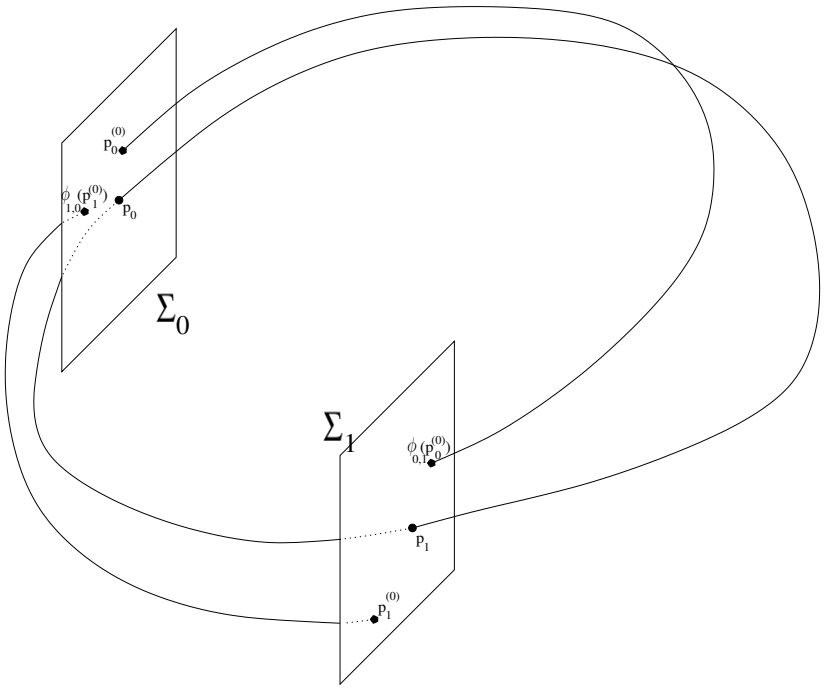

Figure A.4: Illustration of a periodic orbit intersecting two sections and the first iterate of a Newton's method to compute it.

Hence

$$D\Phi = \begin{pmatrix} 0 & D\phi_{0,1}(p_0) \\ D\phi_{1,0}(p_1) & 0 \end{pmatrix}.$$

The dimension of the problem is now doubled so that the instability is reduced by (approximately) its square root.

In fact, considering the linear part of the flow, we may write the fundamental solution of $\dot{x} = Ax$ as e^{At}.

Considering the eigenvalues of A, it is the one with maximum norm, say λ, the responsible for the largest amount of error acumulated, as if we consider a random error source (truncation, for example) of the order of the machine precision - if we are doing the computations in double, order 10^{-16} - as we evolve the flow, this error will be approximately given by $e^{\lambda T} \cdot 10^{-16}$, where T is the period of the orbit.

So if we integrate for, say half-time the whole flow (this is not necessarily the case when doing spatial projection, but for simplicity we will assume it is) so the amount of error will be $e^{\lambda T/2} \cdot 10^{-16} = \sqrt{e^{\lambda T}} \cdot 10^{-16}$.

In the PCRTBP case, we have used two spatial sections:

- $\Sigma_0 : \{(x, y, p_x, p_y)/y = 0; x < -1 + \mu\}$;
- $\Sigma_1 : \{(x, y, p_x, p_y)/y = 0; x > -1 + \mu\}$.

For the orbits related to $H = -1.5175$ we have

- $e^{\lambda_1} \approx 1903.192581883$;

- $e^{\lambda_2} \approx 1560.970008742$;

and this is the main reason for us to use two sections: it is easier to handle eigenvalues of the magnitude of the square root of these numbers when the integration is not long enough, which is precisely our case when computing the dynamical objects that play a key role in Oterma's orbit, due to the fact that its transition is a rapid one.

In the case of the PCRTBP studied here, let us see how to write the mapping (A.5).

Let the superscripts $^-$ and $^+$ denote a variable belonging to Σ_0 and to Σ_1 respectively.

We may write the mapping as

$$\begin{pmatrix} x^- \\ p_x^- \\ x^+ \\ p_x^+ \end{pmatrix} \overset{\Pi_0}{\longmapsto} \begin{pmatrix} x^- \\ y^-(=0) \\ p_x^- \\ p_y^- \\ x^+ \\ y^+(=0) \\ p_x^+ \\ p_y^+ \end{pmatrix} \overset{\phi}{\longmapsto} \begin{pmatrix} \overline{x}^+ \\ \overline{y}^+(=0) \\ \overline{p_x}^+ \\ \overline{p_y}^+ \\ \overline{x}^- \\ \overline{y}^-(=0) \\ \overline{p_x}^- \\ \overline{p_y}^- \end{pmatrix} \overset{\Pi_1}{\longmapsto} \begin{pmatrix} \overline{x}^+ \\ \overline{p_x}^+ \\ \overline{x}^- \\ \overline{p_x}^- \end{pmatrix}, \tag{A.6}$$

where we are using the same names for the functions for the sake of simplicity.

And now, for the derivatives, calling $\Phi = \Pi_1 \circ \phi \circ \Pi_0$, we have

$$
\begin{aligned}
D\Phi &= D\Pi_1 \cdot D\phi \cdot D\Pi_0 \\
&= \begin{pmatrix} 1 & 0 & 0 & 0 & 0 & 0 & 0 & 0 \\ 0 & 0 & 1 & 0 & 0 & 0 & 0 & 0 \\ 0 & 0 & 0 & 0 & 1 & 0 & 0 & 0 \\ 0 & 0 & 0 & 0 & 0 & 0 & 0 & 1 \end{pmatrix}
\begin{pmatrix} v_{11}^- & v_{12}^- & v_{13}^- & v_{14}^- & 0 & 0 & 0 & 0 \\ v_{21}^- & v_{22}^- & v_{23}^- & v_{24}^- & 0 & 0 & 0 & 0 \\ v_{31}^- & v_{32}^- & v_{33}^- & v_{34}^- & 0 & 0 & 0 & 0 \\ v_{41}^- & v_{42}^- & v_{43}^- & v_{44}^- & 0 & 0 & 0 & 0 \\ 0 & 0 & 0 & 0 & v_{11}^+ & v_{12}^+ & v_{13}^+ & v_{14}^+ \\ 0 & 0 & 0 & 0 & v_{21}^+ & v_{22}^+ & v_{23}^+ & v_{24}^+ \\ 0 & 0 & 0 & 0 & v_{31}^+ & v_{32}^+ & v_{33}^+ & v_{34}^+ \\ 0 & 0 & 0 & 0 & v_{41}^+ & v_{42}^+ & v_{43}^+ & v_{44}^+ \end{pmatrix}
\begin{pmatrix} 1 & 0 & 0 & 0 \\ 0 & 0 & 0 & 0 \\ 0 & 1 & 0 & 0 \\ \frac{\partial p_y^-}{\partial x^-} & \frac{\partial p_y^-}{\partial p_x^-} & 0 & 0 \\ 0 & 0 & 1 & 0 \\ 0 & 0 & 0 & 0 \\ 0 & 0 & 0 & 1 \\ 0 & 0 & \frac{\partial p_y^+}{\partial x^+} & \frac{\partial p_y^+}{\partial p_x^+} \end{pmatrix} \\
&= \begin{pmatrix} v_{11}^- + \frac{\partial p_y^-}{\partial x^-} v_{13}^- & v_{13}^- + \frac{\partial p_y^-}{\partial p_x^-} v_{14}^- & 0 & 0 \\ v_{31}^- + \frac{\partial p_y^-}{\partial x^-} v_{34}^- & v_{33}^- + \frac{\partial p_y^-}{\partial p_x^-} v_{34}^- & 0 & 0 \\ 0 & 0 & v_{11}^+ + \frac{\partial p_y^+}{\partial x^+} v_{13}^+ & v_{13}^+ + \frac{\partial p_y^+}{\partial p_x^+} v_{14}^+ \\ 0 & 0 & v_{31}^+ + \frac{\partial p_y^+}{\partial x^+} v_{34}^- & v_{31}^+ + \frac{\partial p_y^+}{\partial p_x^+} v_{34}^+ \end{pmatrix}.
\end{aligned}
\tag{A.7}
$$

A.3 Computation of the Stability of a Periodic Orbit

The computation of the stability of a periodic orbit is done by computing the eigenvalues of the monodromy matrix.

For the case of a single shooting computation, there is nothing else to be added, it is enough to compute the eigenvalues of the monodromy matrix, and the biggest one gives us the amount of instability of the application.

But, for the case of a parallel shooting, the way of assembling the matrix to compute the eigenvalues can be done in a different way, as follows.

Let v be an eigenvector of $A = D\phi$ associated to the eigenvalue λ.

Let $A_0 = D\phi_{0,1}$ and $A_1 = D\phi_{1,0}$.

So $A = A_1 A_0$.

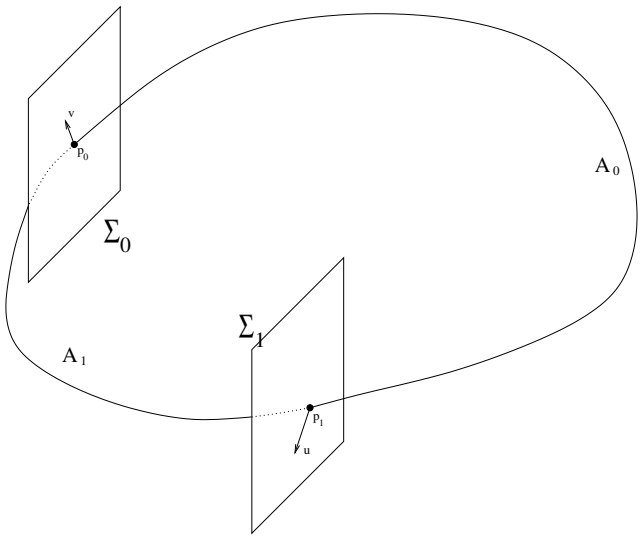

Figure A.5: Illustration of a periodic orbit intersecting two sections with an eigenvector.

We have that

$$Av = A_1A_0v = \lambda v \Longleftrightarrow \left\{ \begin{array}{rcl} A_1u & = & \sqrt{\lambda}v \\ A_0v & = & \sqrt{\lambda}u. \end{array} \right. \Longleftrightarrow \left(\begin{array}{c|c} & A_0 \\ \hline A_1 & \end{array} \right) \begin{pmatrix} u \\ v \end{pmatrix} = \sqrt{\lambda} \begin{pmatrix} u \\ v \end{pmatrix}.$$

Remark: In the case of tori computation, the above computation is extended to 4 sections.

A.4 Continuation of a Periodic Orbit

In many applications it is interesting to investigate not only a single periodic orbit, but how it changes according to variation of the parameters.

The numerical continuation of periodic orbits is a widely-known tool and we will briefly explain three ways on how it can be implemented and the results for the PCRTBP.

The main idea is to used the already computed orbit(s) to predict a new one and correct this prediction until a desired accuracy is reached.

A.4.1 First Approach

In this first approach, the prediction is done as simply as possible: the initial guess for the orbit to be computed are exactly the one that was already done.

Taking, as shown in Figure A.6, as a computed periodic orbit, the one with parameter μ_0 and initial data

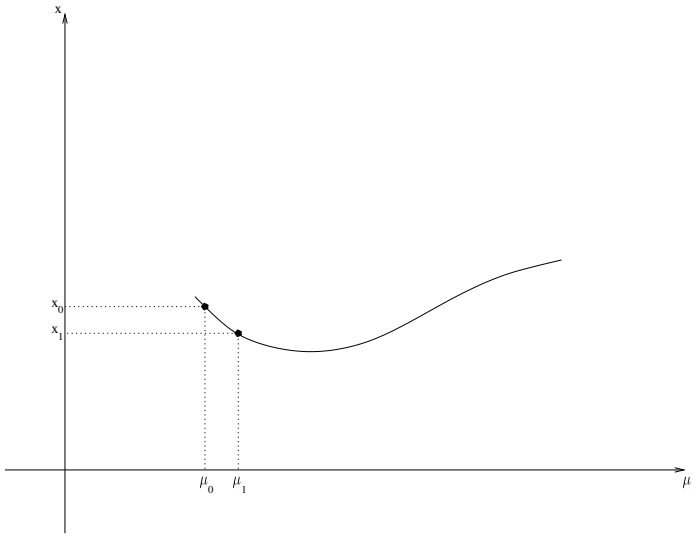

Figure A.6: Illustration of a curve of continuation of periodic orbits highlighting two of them.

x_0 and the one we would like to compute the one with index 1.

We are assuming that an increment is made in the parameter (from μ_0 to μ_1) and that we would like to compute the initial data for the new parameter, i.e., we would like to compute x_1, using, as initial seed, x_0.

Remark: This refinement is done by a Newton's method.

This approach is valid in the sense of being simple - all we need to do is to change the parameter and applying the same method to compute the next orbit - and also that in case it do not converge, it is easy to set a smaller variation in the parameter and run the program again.

Now that we have at least two sets of initial data to periodic orbits and two different values of parameters, let us see how this can be used in improving the predicting part.

A.4.2 A Slight Modification

As we have two computed periodic orbits, we are able to use both in order to give a best prediction, instead of using just one.

The idea is illustrated in Figure A.7.

Remark: It is important to notice that the parameter value of the initial guess is ignored in this approach. It can be used, if it is seen as a variable also to be computed, but it is not the case here. In the case of equal variation of the parameter, this value will be already correct. All the computations hereafter will be done considering equal-spaced parameters.

The vectors that are represented in Figure A.7 are, actually, the same, but with different starting points:

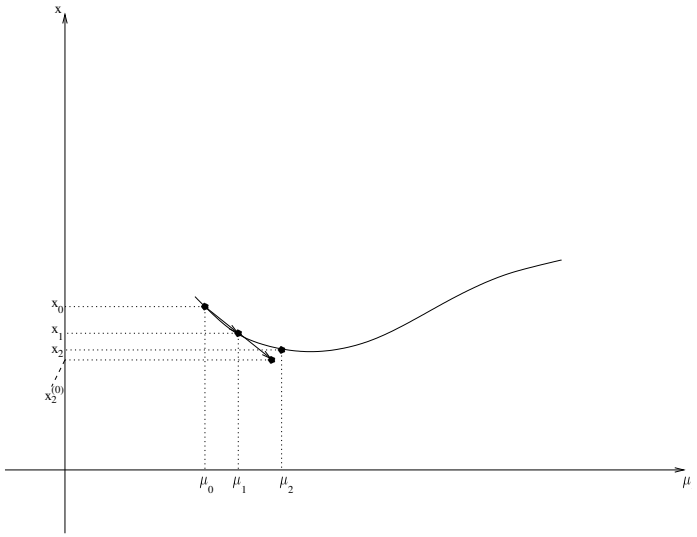

Figure A.7: Illustration of a curve of continuation of periodic orbits highlighting three of them, two already computed that are used to compute an initial guess for the third one.

It is defined as the vector that goes from (x_0, μ_0) to (x_1, μ_1), i.e., $(x_1, \mu_1) - (x_0, \mu_0)$, and it is translated to start in (x_1, μ_1).

The reason for this is because if we consider x as a function of μ, it is already known that the first-order approximation of a function is a straight line with angular coefficient given by its derivative, and, as we do not have the explicit computation of the derivative, we can approximate it by the secant between two near points and use this to extrapolate to the next point.

Once we have the third point calculated, it is also possible to use three points, instead of two, in the prediction of the fourth, i.e., to compute an initial approximation $x_3^{(0)}$ to the fourth point x_3, instead of using x_1 and x_2 it is possible to use x_0, x_1 and x_2, as follows.

Notice that, doing the above-explained scheme with vectors is equivalent to compute $x_2^{(0)}$ the following way:

Consider the Taylor series of $x(\mu)$ around μ_0, truncated in the first order:

$$x(\mu) \approx x(\mu_0) + x'(\mu)(x - x_0).$$

Consider now the approximation of the derivative of $x(\mu)$ in x_0 by a forward difference:

$$x'(\mu) \approx \frac{x(\mu_1) - x(\mu_0)}{\mu_1 - \mu_0} = \frac{x_1 - x_0}{\mu_1 - \mu_0}.$$

Mixing the last two approximations, we are able to produce an approximation for $x(\mu_2)$:

$$x(\mu_2) \approx x_0 + \frac{x_1 - x_0}{\mu_1 - \mu_0}(\mu_2 - \mu_0) \stackrel{*}{=} x_0 - 2(x_1 - x_0) = 2x_1 - x_0.$$

* As we are dealing with an equal spaced mesh in the parameters, $\mu_2 - \mu_0 = 2(\mu_1 - \mu_0)$.

Call $x_2^{(0)} := 2x_1 - x_0$.

Let us now see how this can be extended to three points:

Interpolating (x_0, μ_0), (x_1, μ_1) and (x_2, μ_2) by the Newton's divided differences method we have that

$$x(\mu) \approx x(\mu_0) + \frac{x(\mu_1) - x(\mu_0)}{\mu_1 - \mu_0}(\mu - \mu_0) + \frac{\dfrac{x(\mu_2) - x(\mu_1)}{\mu_2 - \mu_1} + \dfrac{x(\mu_1) - x(\mu_0)}{\mu_1 - \mu_0}}{\mu_2 - \mu_0}(\mu - \mu_0)(\mu - \mu_1).$$

Calling $\delta = \mu_1 - \mu_0 = \mu_2 - \mu_1$, we have that the above expression can be used to approximate $x(\mu_3)$:

$$\begin{aligned} x(\mu_3) &\approx x_0 + \frac{x_1 - x_0}{\delta}(3\delta) + \frac{\dfrac{x_2 - x_1}{\delta} + \dfrac{x_1 - x_0}{\delta}}{2\delta}(3\delta)(2\delta) \\ &= 3x_2 - 3x_1 + x_0. \end{aligned}$$

Call $x_3^{(0)} := 3x_2 - 3x_1 + x_0$.

This algorithm can be extended to any number of points, although in this thesis we have just used 3 points in the continuation of tori, in Chapter 5.

A.4.3 Pseudo-arc Length

The approaches explained above have a problem: they are not able to compute curves with turning points.

A turning point is a point in the curve where the tangent line is vertical, as illustrated in Figure A.8.

In order to overcome this difficulty, we may use what is known as the pseudo arc-length technique.

The idea is instead of considering the parameter as something that varies in a fixed way, consider it as one variable more of the system, computing a prediction for the next iteration and correcting it until some prescribed precision is reached.

The geometry behind this idea is to compute the intersection between the curve and a circle of small radius centered at the computed initial data of the previous periodic orbit using the idea of translating the vector between the last two orbits as a prediction.

Figure A.9 illustrates this idea.

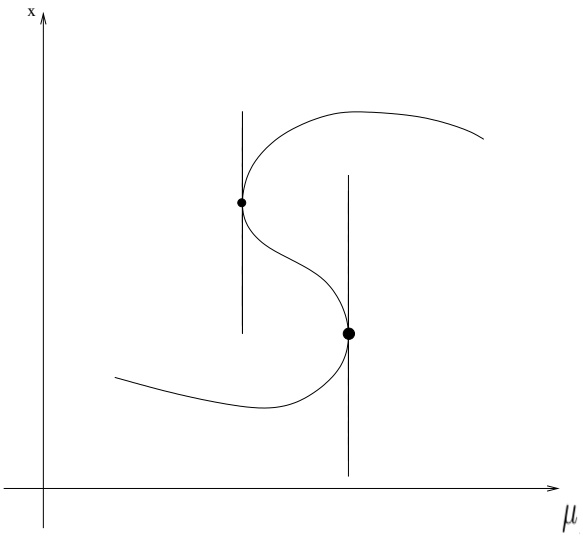

Figure A.8: Illustration of a curve of continuation of periodic orbits with two turning points.

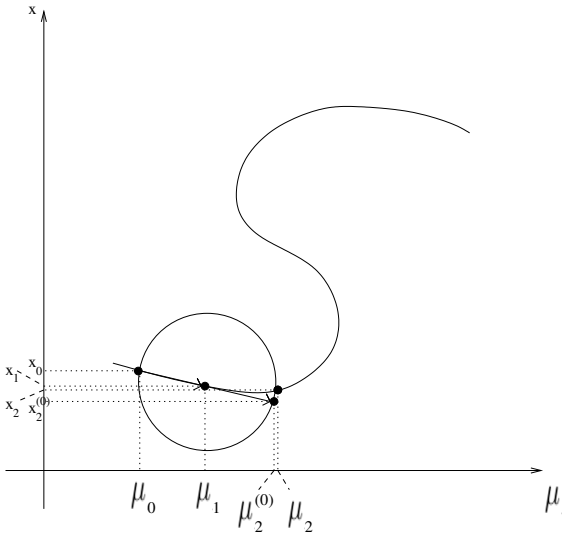

Figure A.9: Illustration of the pseudo-arc length tool.

When using this technique, we are considering the parameteer as a variable, so as we have earned a new variable, we should provide the system a new equation, and it comes exactly from the idea that the new point should belong to the this circle, i.e., in addition to the system of equations are we supposed to solve to compute the initial data for the periodic orbit, we have an equation of a sphere.

Let us now see how to organize all of this to implement it.

Let us consider now a dynamical system depending on a parameter μ:

$$\dot{x} = f(x, \mu), \tag{A.8}$$

where $x \in \mathbb{R}^n$, $t \in \mathbb{R}$ and $\mu \in \mathbb{R}$.

Rewriting (A.8) as $\dfrac{dx}{dt} = f(x,\mu)$ and derivating with respect to μ we have $\left(\dfrac{d}{dt}\dfrac{\partial x}{\partial \mu} =\right) \dfrac{\partial}{\partial \mu}\dfrac{dx}{dt} = \dfrac{\partial}{\partial \mu} f(x,\mu)$ which, by the chain rule, gives us $\dfrac{d}{dt}\underbrace{\dfrac{\partial x}{\partial \mu}}_{p} = D_x f(x,\mu)\cdot \underbrace{\dfrac{\partial x}{\partial \mu}}_{p} + \dfrac{\partial f}{\partial \mu}$.

Writing $x(t; x_0, \mu)$ and considering, without loss of generality the initial time to be $t = 0$, we have that $x(0; x_0, \mu) = x_0$, so $\left.\dfrac{\partial x}{\partial \mu}\right|_{t=0} = 0$.

So now, the system we should integrate is given by the following $n + n^2 + n$ equations:

$$\begin{cases} \dot{x} &= f(x,\mu) \\ \dot{V} &= D_x f(x,\mu) V \\ \dot{p} &= D_x f(x,\mu) p + \dfrac{\partial f}{\partial \mu} \end{cases} \tag{A.9}$$

with initial conditions

$$\begin{cases} x(0) &= x_0 \\ V(0) &= I \\ p(0) &= 0 \end{cases} \tag{A.10}$$

Now, let us focus in the correction part.

We have, as stated above, one variable together with one equation more, so we should see now how to assemble the derivative matrix.

Schematically, we have that

$$\begin{pmatrix} & A & & B & \\ \hdashline & \multicolumn{3}{c}{\mathrm{C}} & \end{pmatrix},$$

where A is the variational matrix without considering the parameter as a variable, B is a vector containing the derivatives with respect to the parameter and C is a row vector containing the derivatives of the equation of the sphere centered in (x_0, μ_0) and radius δ.

For the case of a continuation with parallel shooting, in the PCRTBP, the matrix is (recalling (A.7)) as follows

$$\begin{pmatrix} v_{11}^- + \frac{\partial p_y^-}{\partial x^-} v_{13}^- & v_{13}^- + \frac{\partial p_y^-}{\partial p_x^-} v_{14}^- & 0 & 0 & \frac{\partial p_y^-}{\partial H} v_{14}^- \\ v_{31}^- + \frac{\partial p_y^-}{\partial x^-} v_{34}^- & v_{33}^- + \frac{\partial p_y^-}{\partial p_x^-} v_{34}^- & 0 & 0 & \frac{\partial p_y^-}{\partial H} v_{34}^- \\ 0 & 0 & v_{11}^+ + \frac{\partial p_y^+}{\partial x^+} v_{13}^+ & v_{13}^+ + \frac{\partial p_y^+}{\partial p_x^+} v_{14}^+ & \frac{\partial p_y^-}{\partial H} v_{14}^+ \\ 0 & 0 & v_{31}^+ + \frac{\partial p_y^+}{\partial x^+} v_{34}^- & v_{31}^+ + \frac{\partial p_y^+}{\partial p_x^+} v_{34}^+ & \frac{\partial p_y^-}{\partial H} v_{34}^- \\ 2(x^- - x_0^-) & 2(p_x^- - p_{x_0}^-) & 2(x^+ - x_0^+) & 2(p_x^+ - p_{x_0}^+) & 2(H - H_0) \end{pmatrix}.$$

Remark: The parameter in this case is the value of the Hamiltonian itself H. We could have chosen other values, for instance, the frequency of the orbit, but fixing one of them is enough for our illustration purposes. For more details, see [GM01]. In addition, the subscript $_0$ denote the previosly computed orbit.

Remark: The reason for the part B of this variational matrix to have these terms is because, considering the parameter H as a variable, the mapping (A.6) turns out to be given by

$$\begin{pmatrix} x^- \\ p_x^- \\ x^+ \\ p_x^+ \\ \mathrm{H} \end{pmatrix} \overset{\Pi_0}{\longmapsto} \begin{pmatrix} x^- \\ y^-(=0) \\ p_x^- \\ p_y^- \\ x^+ \\ y^+(=0) \\ p_x^+ \\ p_y^+ \end{pmatrix} \overset{\phi}{\longmapsto} \begin{pmatrix} \overline{x}^+ \\ \overline{y}^+(=0) \\ \overline{p_x}^+ \\ \overline{p_y}^+ \\ \overline{x}^- \\ \overline{y}^-(=0) \\ \overline{p_x}^- \\ \overline{p_y}^- \end{pmatrix} \overset{\Pi_1}{\longmapsto} \begin{pmatrix} \overline{x}^+ \\ \overline{p_x}^+ \\ \overline{x}^- \\ \overline{p_x}^- \end{pmatrix}, \tag{A.11}$$

and so, the derivative $D\Pi_0$ is given by

$$\begin{pmatrix} 1 & 0 & 0 & 0 & 0 \\ 0 & 0 & 0 & 0 & 0 \\ 0 & 1 & 0 & 0 & 0 \\ \frac{\partial p_y^-}{\partial x^-} & \frac{\partial p_y^-}{\partial p_x^-} & 0 & 0 & \frac{\partial p_y^-}{\partial H} \\ 0 & 0 & 1 & 0 & 0 \\ 0 & 0 & 0 & 0 & 0 \\ 0 & 0 & 0 & 1 & 0 \\ 0 & 0 & \frac{\partial p_y^+}{\partial x^+} & \frac{\partial p_y^+}{\partial p_x^+} & \frac{\partial p_y^+}{\partial H} \end{pmatrix}.$$

Applying these above-explained tools, we have as a result, the computed periodic orbits shown in Figure A.10 and the diagrams shown in Figure A.11.

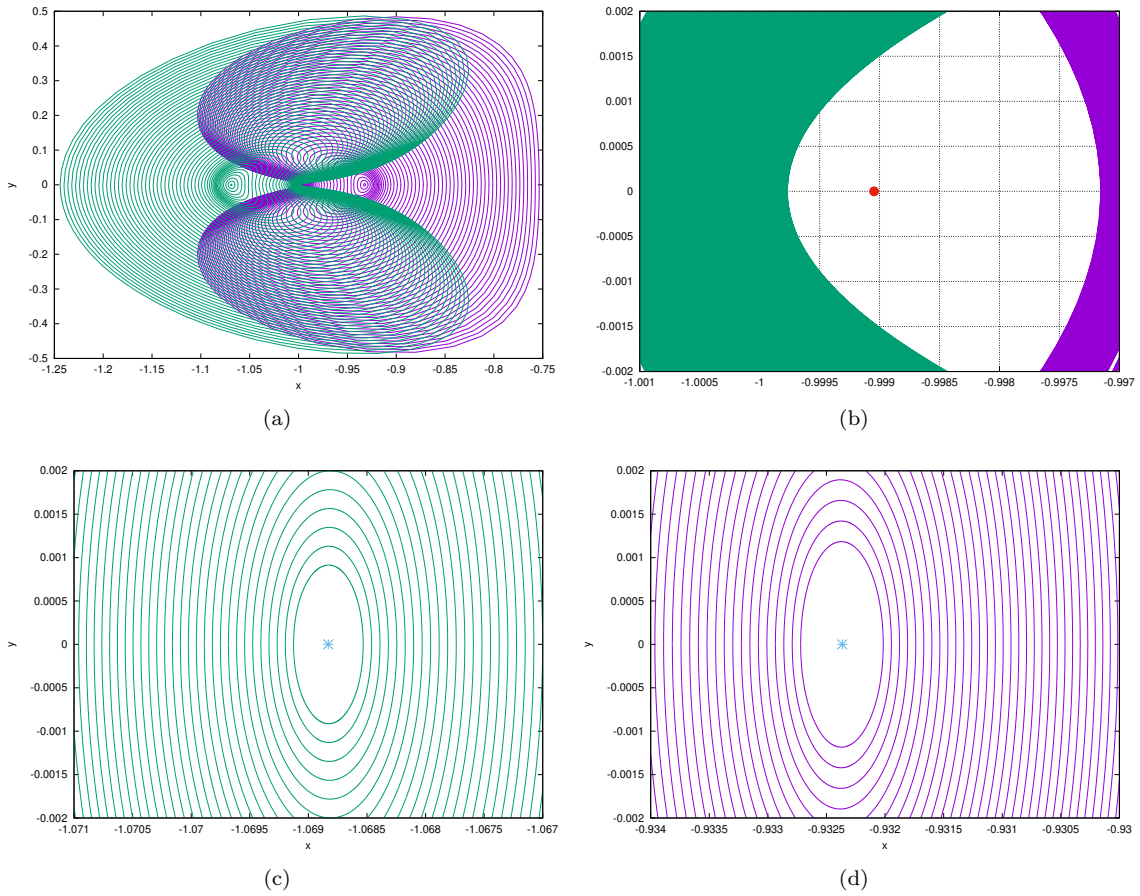

Figure A.10: Computed periodic orbits around L_1 (in green) and L_2 (in purple). (a) The whole picture. (b) Zoom around Jupiter (in red). (c) Zoom around L_2 (in cyan). (d) Zoom around L_1 (in cyan).

In total, 2129 orbits around L_1 and 2125 around L_2 were calculated and, while every orbit is plotted in Figure A.11, in Figure A.10 it is shown every 40 orbits.

All of these data were computed with the pseudo-arc technique with a sphere of radius $\delta = 10^{-4}$ using parallel shooting with 2 sections Σ_0 and Σ_1 already defined before.

The reason for the difference in the number of orbits computed around L_1 and L_2 is because we have started in an orbit in the middle (the one related to $H = -1.5175$ for both) and then subtracting until Newton's method is not able to converge anymore, then going back to $H = -1.5175$ and adding until 2000 orbits (in this direction) were computed.

Remark: There is no formal reason to choose the number 2000, other than it is enough to show that

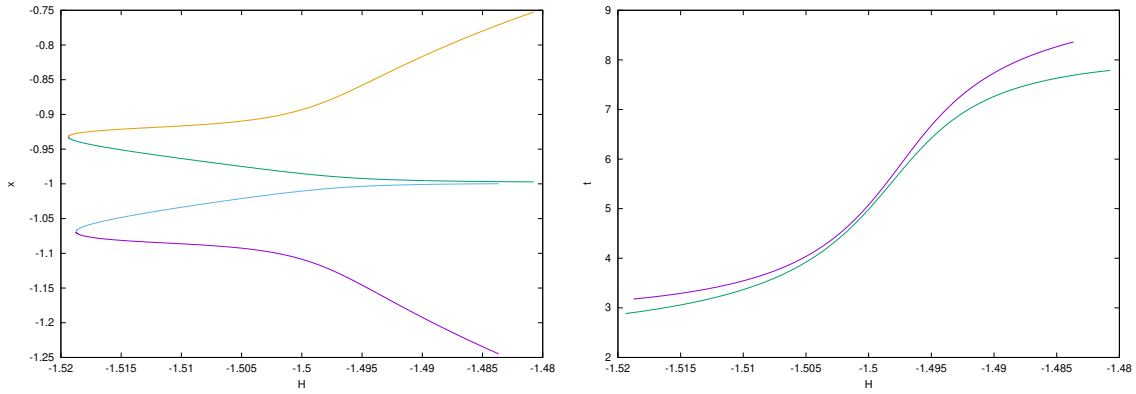

(a) (b)

Figure A.11: Continuation diagram with respect to the energy as a parameter. (a) Both x^- and x^+ of L_1 and L_2 are represented in this figure. (b) Period of the orbit $\times$ Hamiltonian value. In purple the orbits around L_2 and, in green, the ones around L_1.

these orbits grown until almost hit Jupiter, in fact, slightly after passing the number 2000 the correction method start to have some convergence problems, so that number is enough.

A.5 Computation of the Stable and Unstable Manifolds of a Periodic Orbit

When computing the eigenvalues and the eigenvectors of the mapping (A.5), as explained in Section A.3, we use the largest eigenvalue to compute how unstable is the periodic orbit.

Remark: Let us highlight that every concept that will be explained in this section will be in the case of the PCRTBP. A more general approach of beyond the scope of this appendix. We refer to [Sim90] to it.

Now, we will use also the computed eigenvectors as the linear approximation to the stable and the unstable manifolds of a given periodic orbit - the one related to the greater one will give us the direction of the unstable manifold, and the smaller eigenvalue, the stable one.

Let p be a point in the periodic orbit - for instance the one in Σ_0 - and $v^-_>$ ($v^-_<$) the computed eigenvector associated to the greater (smaller) eigenvalue $\lambda_>$ ($\lambda_<$).

In order to have an approximation of the unstable (stable) manifold, take a small h and consider $p \pm hv^-_>$ ($p \pm hv^-_<$).

Notice that this is related to what is illustrated in Figure 4.1.

Remark: The points $p \pm hv^-_>$ ($p \pm hv^-_<$), do not belong to the unstable (stable) manifold, but to the

unstable (stable) eigenspace of p. So, if we take a small value for h these points will still not belong to the manifold, but they will be at a distance of $O(h^2)$.

Remark: The value of h taken in the computations in this section is $h = 10^{-8}$.

Taken the initial point, if we integrate it in the PCRTBP flow, the points we will compute will be close to the stable/unstable manifolds we would like to visualize.

Notice that it will be an orbit, so the visualization will not be the best one possible, as we would like to see a two-dimensional object.

There are some ways of overcoming this issue, and one of them will be explained in the next subsection.

A.5.1 Fundamental Domain

Consider a map $f : \mathbb{R}^n \to \mathbb{R}^n$ and $x \in \mathbb{R}^n$ a hyperbolic fixed point of f.

A fundamental domain of the unstable manifold of x (W_x^u) is the segment of the curve between $a \in W_x^u$ and $f(a)$, as illustrated in Figure A.12. It is analogous for the stable manifold.

This idea is important and can be applied in the computation of the unstable/stable manifolds due to the following property:

Property: The points lying between a and $f(a)$, will land between $f(a)$ and $f^2(a)$ when the map f is applied on them, as a consequence, the points between $f(a)$and $f^2(a)$ will land between $f^2(a)$ and $f^3(a)$, and so forth.

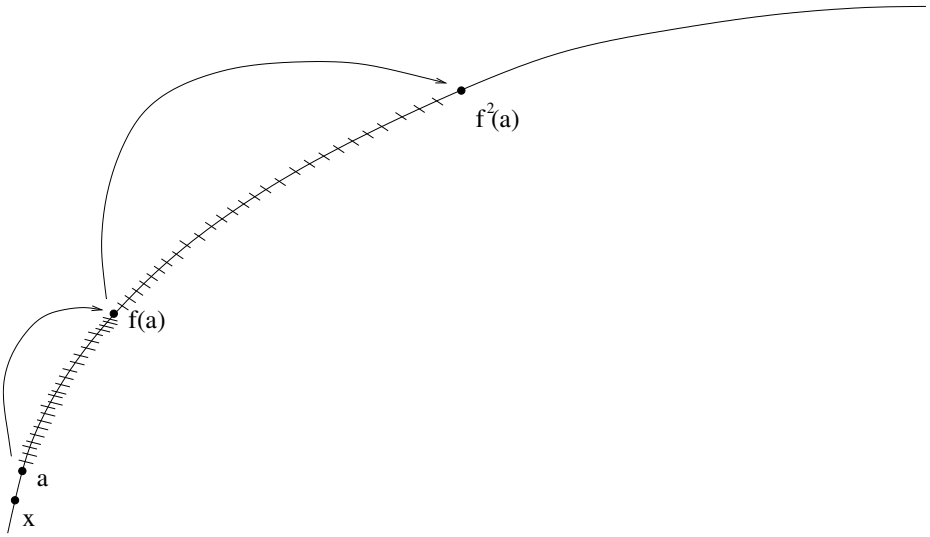

Figure A.12: Illustration of a fundamental domain of an invariant curve under the mapping f.

The problem about using this idea to compute an approximation of $W_x^{u,s}$ is that, in general, we have no idea about the intermediate points lying between x and $f(x)$.

A simple solution for this is to consider x near a in the direction of the unstable eigenspace, say $a = x + hv_>$, for h small enough, so that, $f(a) \approx f(x) + h\lambda v_> = x + h\lambda v_>$. Once again, for the stable manifold, the idea is similar.

With this, the segment of curve between x and $f(x)$ can be well approximated by a straight line.

So, using this idea, we can take the points $p \pm hv_>^-$ ($p \pm hv_<^-$), that were defined in Section A.5, apply the dynamics on them to have $\phi(p \pm hv_>^-)$ ($\phi(p \pm hv_<^-)$), consider the line between them, divide it in some points and integrate each of these to visualize the unstable (stable) manifold.

This approach can also be improved considering the parallel shooting as follows.

We can consider the points p^- and p^+ as the intersections of the computed periodic orbit with Σ_0 and Σ_1 respectively.

Consider also the vectors $v_<^-$ and $v_<^+$ the eigenvectors associated to $\lambda_>$ and $v_>^-$ and $v_>^+$ the ones associated to $\lambda_>$.

Now consider the points $p^- + hv_>^-$ and $p^- + hv_>^+$.

Remark: All the computations presented here can be done also for the other pairs of points, so we will present only for the ones already mentioned.

For the construction of the line between points for the usage of the fundamental domain idea, consider the pairs $\{p^- + hv_>^-, \phi_{1,0}(p^+ + hv_>^+)\}$ and $\{p^+ + hv_>^+, \phi_{0,1}(p^- + hv_>^-)\}$.

See Figure A.13 for the illustration of all of these points.

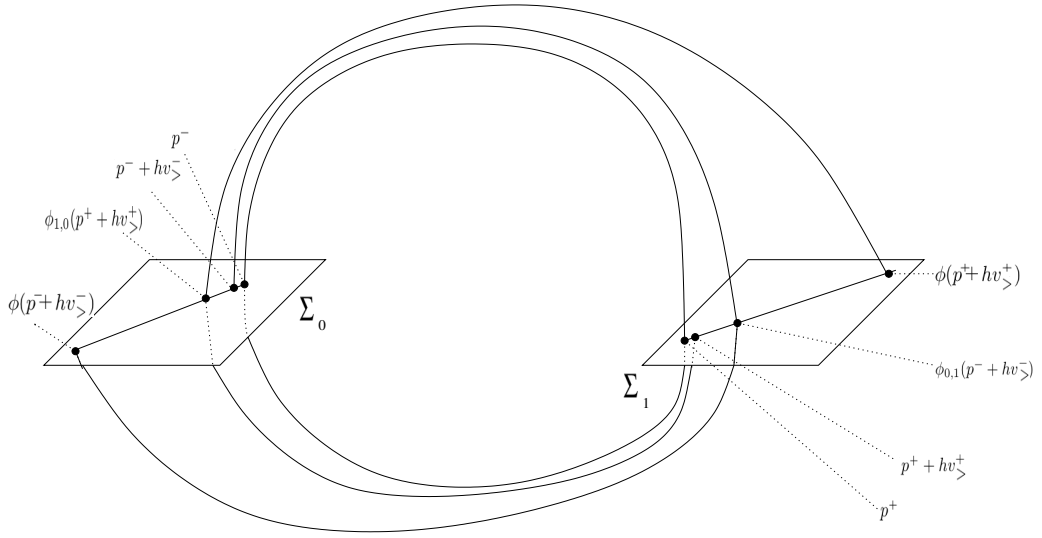

Figure A.13: Illustration of the mixing of the ideas of fundamental domain and parallel shooting.

Notice that the distance between $p^- + hv_>^-$ and $\phi_{1,0}(p^+ + hv_>^+)$ is smaller than the one between $p^- + hv_>^-$ and $\phi(p^- + hv_>^-)$, and this difference can be estimated.

Notice that, as h has a small value, it is possible to linearly approximate $\phi_{1,0}(p^+ + hv_>^+)$ and $\phi(p^- + hv_>^-)$ as follows:

- $\phi_{1,0}(p^+ + hv_>^+) \approx \phi_{1,0}(p^-) + hD\phi_{1,0}v_>^+ = p^- + h\sqrt{\lambda_>}u_>^+$;
- $\phi(p^- + hv_>^-) \approx \phi(p^-) + hD\phi v_>^- = p^- + h\lambda_> v_>^+$.

This means that, while the distance from $p^- + hv_>^-$ to $\phi_{1,0}(p^+ + hv_>^+)$ is of the order $\sqrt{\lambda_>}$ (≈ 43.625595490302 for the periodic orbit around L_1 related to $H = -1.5175$), the one between $p^- + hv_>^-$ and $\phi(p^- + hv_>^-)$ is of the order $\lambda_>$ (≈ 1903.192581883 also for L_1 and $H = -1.5175$), which gives us a better linear approximation.

In the case of the computations for the unstable and stable manifolds of the periodic orbits around L_1 and L_2 in the PCRTBP, we have used 100 intermediate equally spaced points between $p^- + hv_>^-$ and $\phi_{1,0}(p^+ + hv_>^+)$ and 100 more between $p^+ + hv_>^+$ and $\phi_{0,1}(p^- + hv_>^-)$.

The results of these computations are not shown here because they look similar to the ones presented in Chapter 4.

Appendix B

Diagram of Codes and Files

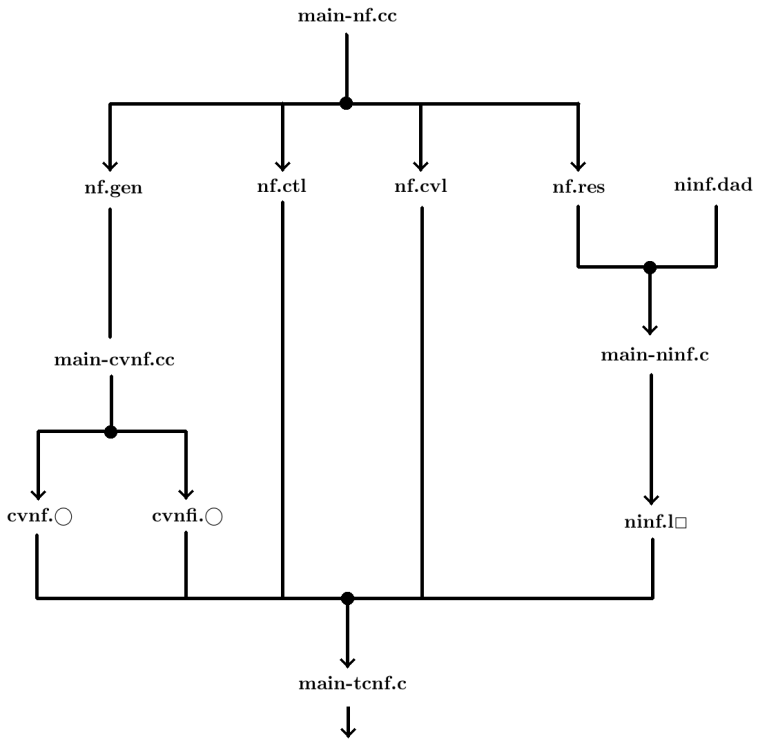

Figure B.1: Normal forms related files

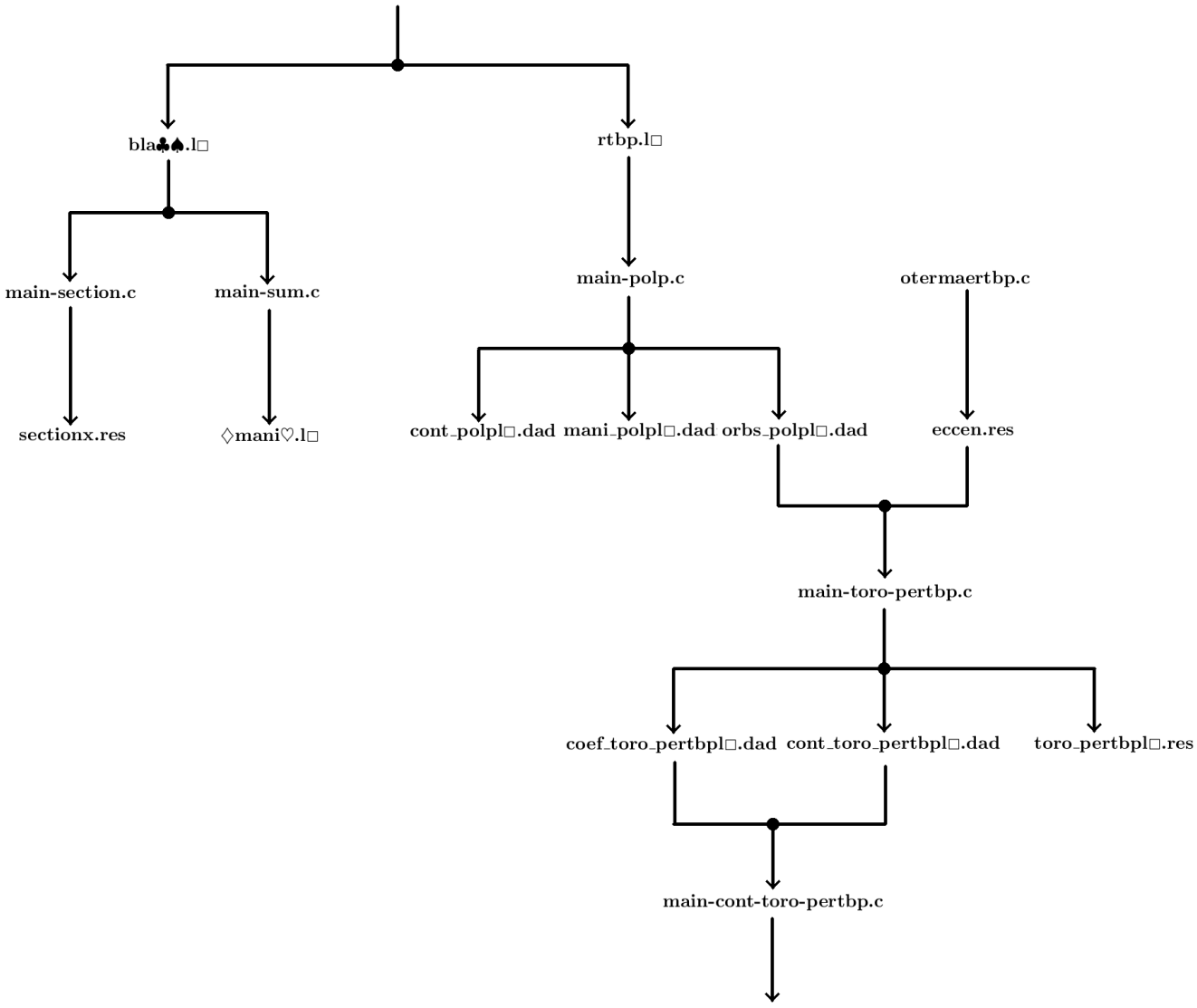

Figure B.2: In this part, there are normal forms (until **rtbp.l□**, **sectionx.res** and **♢mani♡.l□**), periodic orbits and their manifolds (**main-polp.c**, **cont_polpl□.dad**, **mani_polpl□.dad** and **orbs_polpl□.dad**) and tori and their manifolds computation (from **otermaertbp.c** and **main-toro-pertbp.c**) related files.

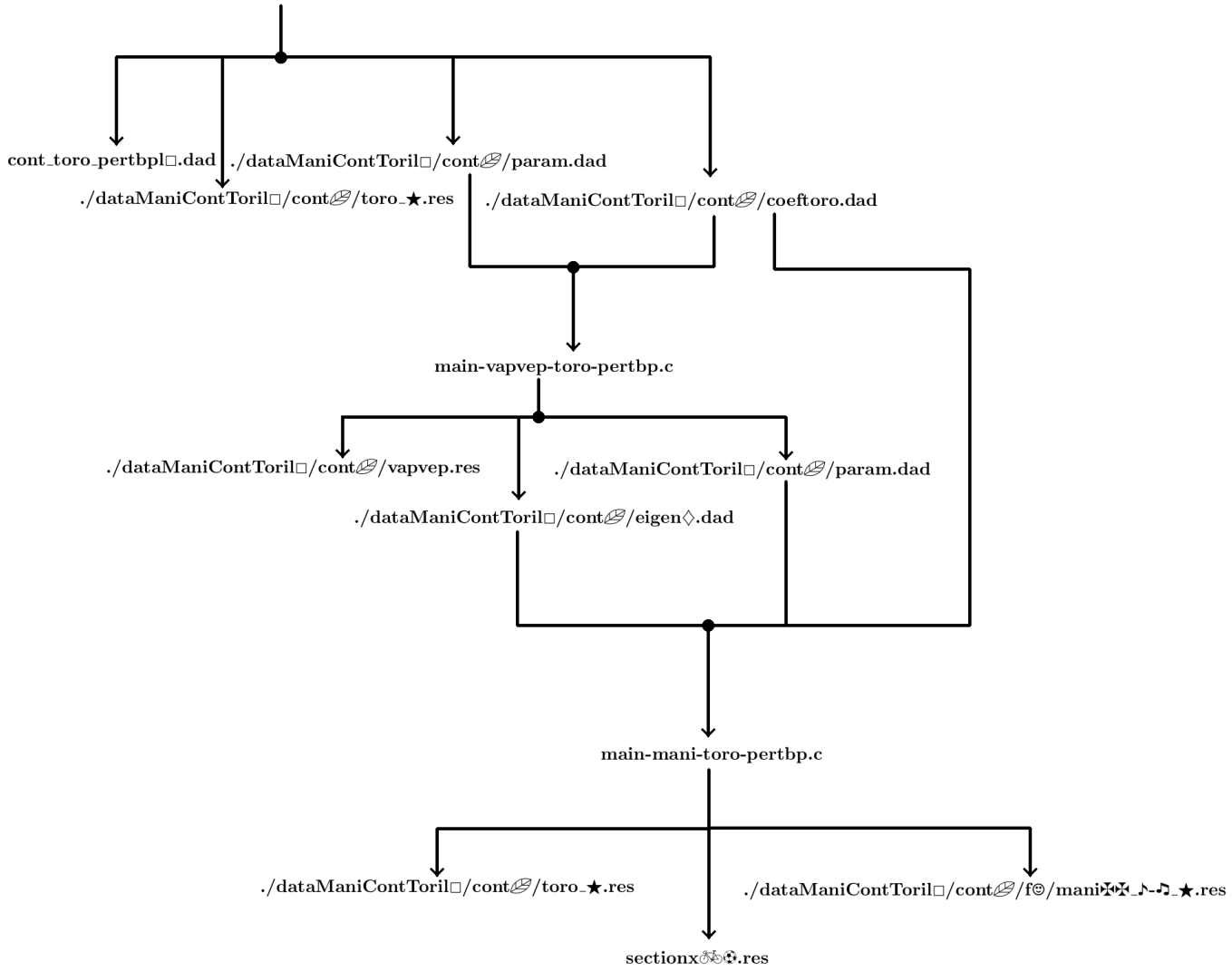

Figure B.3: Tori and their manifolds computation related files

Appendix C

Description of Files

We briefly describe the files used and generated to produce the data presented in this thesis.

The following table shows the variations of the variables used in the names of the files. They will be used in the next sections

◯	$1, \cdots, 6$
□	$1, 2$
🍃	$-1330, \cdots, 3167; -2565, \cdots, 4704$
★	$0, \cdots, 3$
✠	$0, 1$
♪	$0, \cdots, 10; 0, \cdots, 100; 0, \cdots, 1000; 0, \cdots, 10000$
♣	s, u
♠	n, p
♢	stable, unstable
♡	up, down
♫	$10, 100, 1000, 10000$
☺	$0, \cdots, 3, xoj$
🚲	oterma, jupiter, otermajupiter
⚽	$-2565, -1330, 0, 2000, 3167, 4704$

Table C.1: Variation of variables in the names of the used files

C.1 Normal Forms

- **main-nf.cc**: This is the main program to compute the normal forms around L_1 and L_2. It receives as input the primaries' mass ratio (in this thesis $\mu = 9.5388118036310115 \times 10^{-4}$), the degree of the approximation and the point around which it should be computed. The computed degrees were 16, 20, 24, 28 and 32, for comparison. All the computations in Chapter 4 are shown with the degree 32

normal forms. In order to have the normal form around each of the equilibrium point L_1 and L_2, this code should be executed twice, one for each point. As it is based in a previously built code, this code computes the expansion for the SCRTBP. So, to have the computations done to the planar case, it is enough to consider to action variable corresponding to the z direction as 0. It should be mentioned that this is not optimized for this case (as all the allocations are done considering three dimensions, all the computations are also done for the third dimension, among other things), although this is not a serious drawback, as if we are interested in studying the spatial case, this code is already built.

- **nf.gen**: This file is an output of **main-nf.cc** and serves as an input to **main-cvnf.cc**. It stores the generating function responsible for killing the monomials until the Hamiltonian is in it normal form.

- **nf.ctl**: This file is an output of **main-nf.cc** and serves as an input to **main-tcnf.c**. It stores some parameters to be used in the future computations, for instance, around which point the normal form is computed, its degree, the mass ratio and the distance from the closer primary and the equilibrium point.

- **nf.cvl**: This file is an output of **main-nf.cc** and serves as an input to **main-tcnf.c**. It stores the change of variables that put the linear part of the Hamiltonian is its normal form.

- **nf.res**: This file is an output of **main-nf.cc** and serves as an input to **main-ninf.c**. It stores the coefficients of the normal form of the Hamiltonian in action-angle variables.

- **ninf.dad**: This file serves as an input to **main-ninf.c**. It contains the number of points to be computed and initial conditions for each action variable (the saddle and the centre part in the plane and the centre part in the z direction).

- **main-cvnf.cc**: This program computes to nonlinear part of the direct and the inverse change of variables (the linear part was computed in **main-nf.cc** and stored in **nf.cvl**).

- **main-ninf.c**: This program serves just to integrate a given orbit. It should be mentioned that the word "integrate" is used here not necessarily meaning a numerical one, as the approximate Hamiltonian is integrable, instead, it means that the orbit will be computed.

- **cvnf.◯**: This file is an output of **main-cvnf.cc** and serves as an input to **main-tcnf.c**. They store the direct changes of variables, i.e., from normal forms coordinates to synodic ones. $\bigcirc = 1, \cdots, 6$, as, again, this package is adapted from another already built one for the SCRTBP.

- **cvnfi.◯**: This file is an output of **main-cvnf.cc** and serves as an input to **main-tcnf.c**. They store the inverse changes of variables, i.e., from synodic coordinates to normal forms ones. $\bigcirc = 1, \cdots, 6$, as, again, this package is adapted from another already built one for the SCRTBP.

- **ninf.l□**: This file is an output of **main-ninf.c** and serves as an input to **main-tcnf.c**. They store the computed orbits around $L_\square$, $\square = 1, 2$ in normal forms coordinates.

- **main-tcnf.c**: This program transforms coordinates in both directions (from normal form coordinates to synodic ones and vice-versa).

- **bla♣♠.l□**: These files are output of **main-tcnf.c** and serve as inputs to **main-section.c** and **main-sum.c**. They contain the periodic orbit $L_\square$, $\square = 1, 2$ slightly shiftted in each direction ($\spadesuit = n, p$) of the unstable and the stable manifolds $\clubsuit = s, u$, to be numerically integrated in the PCRTBP flow (1.6).

- **rtbp.l□**: This file is an output of **main-tcnf.c** and serves as input to **main-polp.c**. These files contain the periodic orbits around $L_\square$, $\square = 1, 2$ obtained through the transformation of coordinates of the data in file **ninf.l□**.

- **main-section.c**: This program computes the desired sections of the manifolds. In the case of this thesis, it was used just to compute the sections $x = x_J$, where x_J is the x coordinate of Jupiter.

- **main-sum.c**: This program is the responsible for integrating for initial guess for the manifolds in the nonlinear vector field.

- **sectionx.res**: This file is an output of **main-section.c**. It contains the data about the intersection of the manifolds of the periodic orbits around the equilibrium points and the section $x = -1 + \mu$ to produce Figures 4.4 and 4.5.

- **◇mani♡.l□**: These files are outputs of **main-sum.c**. They contain the integrated points of the unstable and the stable manifolds of the periodic orbits around L_1 and L_2.

C.2 Periodic Orbits

- **main-polp.c**: This program computes the periodic orbits around L_1 and L_2 and their stable and unstable manifolds using the tools presented in Appendix A.

- **cont_polpl□.dad**: These files are output of **main-polp.c**. They store the data to produce the continuation diagram shown in Figure A.11.

- **mani_polpl□.dad**: These files are output of **main-polp.c**. They store the computed points of the stable and the unstable manifolds of the periodic orbits around the equilibirum points. They are used for testing as the manifolds' data were already stored in the files ♢**mani**♡**.l**□.

- **orbs_polpl□.dad**: These files are output of **main-polp.c** and serve as input to **main-toro-pertbp.c**. They store the computed orbits shown in Figure A.10.

C.3 Tori

- **otermaertbp.c**: This program computes the change of variables from sidereal to synodic in the PERTBP and integrate the orbit of the projected Oterma.

- **eccen.res**: This file is an output of **otermaertbp.c** and serves as an input to **main-toro-pertbp.c**. It stores the value of the eccentricity of Jupiter. It was computed using the tools presented in Chapter 3.

- **main-toro-pertbp.c**: This program computes a torus around L_1 or L_2 in the PERTBP, using as initial seed, some periodic orbit previously computed in the PCRTBP.

- **toro_pertbpl□.res**: These files are output of **main-toro-pertbp.c** and are split in the following four files **./dataManiContToril□/cont0/toro_★.res**. They store The computed torus in all the four sections ($\Sigma_{\frac{i\pi}{2}}$, $i = 0, 1, 2, 3$).

- **cont_toro_pertbpl□.dad**: These files are output of **main-toro-pertbp.c** and serve as input to **main-cont-toro-pertbp.c**. They store the data to plot to continuation diagram shown in Figure 5.6. To be updated after the execution of **main-cont-toro-pertbp.c**.

- **coef_toro_pertbpl□.dad**: These files are output of **main-toro-pertbp.c** and serve as input to **main-cont-toro-pertbp.c**. They store the Fourier coefficients of the first computed torus. To be copied to the file **./dataManiContToril□/cont0/coeftoro.dad**.

- **main-cont-toro-pertbp.c**: This program implements the continuation method with respect to the rotation number as a parameter.

- **./dataManiContToril□/cont🍃/toro_★.res**: These files are output of **main-cont-toro-pertbp.c** and are updated after the execution of **main-mani-toro-pertbp.c**. They contain first the computed values of a torus in the section $\Sigma_{\frac{\star\pi}{2}}$ and after the computation of the eigenvectors and eigenvalues, they also contain, in addition to these points, the eigenvectors associated to the greater and the smaller eigenvalues on each point, so that the Figure 5.5 could be produced.

- **./dataManiContToril□/cont🍃/param.dad**: These files are, first, output of **main-cont-toro-pertbp.c** and serve as input to **main-vapvep-toro-pertbp.c** than they are updated there and they are used as input also to **main-mani-toro-pertbp.c**. They contain important parameter information of each torus. In their first version, the number of Fourier modes used and the rotation number. After that, they are updated with information about the eigenvalues.

- **./dataManiContToril□/cont🍃/coeftoro.dad**: These files are output of **main-cont-toro-pertbp.c** and serve as input to **main-vapvep-toro-pertbp.c** and **main-mani-toro-pertbp.c**. They contain all the computed coefficients of the tori on each section, stored sequencially.

- **main-vapvep-toro-pertbp.c**: This program computes the eigenvalues and the eigenvectors of a given torus.

- **./dataManiContToril□/cont🍃/vapvep.res**: These files are output of **main-vapvep-toro-pertbp.c**. They store the eigenvalues of each torus.

- **./dataManiContToril□/cont🍃/eigen♢.dad**: These files are output of **main-vapvep-toro-pertbp.c** and are used as an input to **main-mani-toro-pertbp.c**. They store the truncated Fourier series that approximate the eigenfunctions related to the greater and to smaller eigenvalues of each torus to be used to produce approximations to the stable and the unstable manifolds of the given torus.

- **main-mani-toro-pertbp.c**: This program computes the stable and the unstable manifolds of a given torus. It is also the responsible to compute the sections $x = x_O$ and $x = x_J$.

- **sectionx🚲⚽.res**: These files are output of **main-mani-toro-pertbp.c**. They contain the points which belong to the invariant manifolds and the sections, in the case of 🚲=oterma or 🚲=jupiter the section in done in Σ_π, in case 🚲=otermajupiter it is done when $f = f^*$.

- **./dataManiContToril□/cont🍃/f☺/mani✠✠_♪-♫_★.res**: These files are output of **main-mani-toro-pertbp.c**. They contain the manifolds of the tori used to produce Figures **??**-5.13. The first

✠ indicates if it is the stable or the unstable manifold, and the second one, which part of it. ♪ is the number of the curve in the fundamental domain divided in ♫. Finally, ☺ can assume, besides the values 0, 1, 2 and 3, $xoj = 4.7505636157398934$, which represents the section $f = f^*$.

Bibliography

[AM78] R. Abraham, J. E. Marsden. *Foundations of Mechanics*. 2nd Ed., Benjamin/Cummings, Reading, MA, 1978.

[AKN88] V. I. Arnol'd, V. V. Kozlov, A. I. Neĭshtadt. *Dynamical Systems III*. Encyclopaedia of mathematical sciences 3, Springer, Berlin, 1988.

[AEL16] R. L. Anderson, R. W. Easton, M. W. Lo. *Isolating Blocks as Computational Tools in the Circular Restricted Three-Body Problem*. Physica D, 343, 38-50, (2016).

[And98] M. A. Andreu. *The Quasi-Bicircular Problem*. Thesis, Dept. Matemàtica Aplicada i Anàlisi, Universitat de Barcelona (1998).

[AS99] M. A. Andreu, C. Simó. 'Translunar Halo Orbits in the Quasi-Bicircular Problem', B. A. Steves and A. E. Roy editors, *The Dynamics of Small Bodies in the Solar System*, NATO ASI (1997, Maratea, Italy), pp. 309-314 (1999).

[CJ00] E. Castellà, À. Jorba. *On the Vertical Families of Two-Dimensional Tori Near the Triangular Points of the Bicircular Problem*. Celestial Mechanics and Dynamical Astronomy **76** (2000) 35-54.

[Flo04] L. Floría. *On an Analytical Solutuion in the Planar Elliptic Restricted Three–Body Problem*. Monografías del Seminario Matemático García de Galdeano 31, 135–144 (2004).

[GLM+87] G. Gómez, J. Llibre, R. Martínez, C. Simó. *Study on Orbits Near the Triangular Libration Points in the Perturbed Restricted Three-Body Problem*. ESOC contract 6139/84/D/JS(SC), Final Report (1987).

[GLM+00] G. Gómez, J. Llibre, R. Martínez, C. Simó. *Dynamics and Mission Design Near Libration Point Orbits Volume 1: Fundamentals: The Case of Collinear Libration Points*. World Scientific, 2000.

[GKM+04] G. Gómez, W. S. Koon, M. W. Lo, J. E. Marsden, J. Masdemont, S. D. Ross. *Connecting Orbits and Invariant Manifolds in the Spatial Restricted three-Body Problem*. Nonlinearity **17** (2004) 1571-1606.

[GM01] G. Gómez, J. M. Mondelo. *The Dynamics Around the Collinear Equilibrium Points of the RTBP*. Physica D: Nonlinear Phenomena **157** (2001) 283-321.

[GL18] M. Guzzo, E. Lega. *Geometric Chaos Indicators and Computations of the Spherical Hypertube Manifolds of the Spatial Circular Restricted Three-Body Problem*. Physica D 373 (2018) 38–58.

[JV97] À. Jorba, J. Villanueva. *On the persistence of lower dimensional invariant tori under quasiperiodic perturbations*. Journal of Nonlinear Science 7, pp. 427-473 (1997).

[Jor99] À. Jorba. *Numerical Computation of Normal Forms, Central Manifolds and First Integrals of Hamiltonian Systems*. Experimental Mathematics, Vol. 8 (1999), No. 2.

[Jor00] À. Jorba. *A numerical study on the existence of stable motions near the triangular points of the real Earth-Moon system*. Astron. Astrophys., Vol. 364, n. 1, pp. 327-338 (2000).

[Jor01] À. Jorba. *Numerical Computaion of the Normal Behaviour of Invariant Curves of n-Dimensional Maps*. Nonlinearity **14** (2001) 943-976.

[JZ05] À. Jorba, M. Zou. *A software package for the numerical integration of ODE by means of high-order Taylor methods*. Experimental Mathematics 14, pp. 99-117 (2005).

[KLM+00] W. S. Koon, M. W. Lo, J. E. Marsden, S. D. Ross. *Heteroclinic Connections between Periodic Orbits and Resonance Transitions in Celestial Mechanics*. Chaos. 2000 Jun;10(2):427-469.

[KLM+01] W. S. Koon, M. W. Lo, J. E. Marsden, S. D. Ross. *Resonance and Capture of Jupiter Comets*. Celestial Mechanics and Dynamical Astronomy **81**: 27-38, 2001.

[Mee98] J. Meeus. *Astronomical Algorithms*. Willmann-Bell, Richmond, VA, 1998.

[OIY+08] K. Ohtsuka, T. Ito, M. Yoshikawa, D. J. Asher, H. Arakida. *Quasi-Hilda comet 147P/Kushida-Muramatsu Another long temporary satellite capture by Jupiter*. A&A 489, 1355–1362 (2008).

[Pol76] H. Pollard *Celestial Mechanics*. Carus Mathematical Monographs. Mathematical Association of America, 1976.

[Sim90] C. Simó. *On the Analytical and Numerical Approximation of Invariant Manifolds.* Les Méthodes Modernes de la Mecánique Céleste, D. Benest and C. Froeschlé (eds.), pp. 285–329, Editions Frontières, Paris, 1990.

[Sze67] V. Szebehely. *Theory of Orbits. The Restricted Problem of Three Bodies.* Academic Press, New York, 1967.

[Val97] D. A. Vallado., W. D. McClain *Fundamentals of Astrodynamics and Applications.* New York: McGraw-Hill Companies, Inc, 1997.

[Wie84] W. Wiesel. *The Restricted Earth-Sun-Moon Problem I: Dynamics and Libration Point Orbits.* Dept. Aeron. and Astron., Air Force Institute of Technology Wright-Patterson AFB. Ohio (1984).